Comprehensive Single Cell Microfluidic Chips for the Study of Cancer Cell Heterogeneity and Metastasis

by

Yu-Chih Chen

A dissertation submitted in partial fulfillment
of the requirements for the degree of
Doctor of Philosophy
(Electrical Engineering)
in The University of Michigan
2014

Doctoral Committee:

Professor Euisik Yoon, Chair
Professor L. Jay Guo
Professor Shuichi Takayama
Professor Max S. Wicha
Emeritus Professor Kensall D. Wise

TABLE OF CONTENTS

LIST OF FIGURES

LIST OF TABLES

ABSTRACT

Due to the genomic and epigenetic instability of cancer cells, tumors are highly heterogeneous and difficult to treat. Additionally, cancer metastasis, which account for 90% of cancer mortality, is a complicated multi-step process. As such ideal assays should be high-throughput and provide single-cell resolution and microenvironmet control, enlightening individual cell properties rather than the average behavior of the bulk tumor. Here, we have developed microfluidic platforms meeting these requirements to investigate three critical stages of metastasis.

First, a **single-cell migration chip** was developed to model cancer cell migration from the primary tumor. The motility of cells under the influence of chemo-attractants can be measured on-chip. After the assays, highly motile cells and non-motile cells can be retrieved for further culture and analysis. Second, to understand cell survival in the circulatory system, a **single-cell suspension culture chip** was developed, improving the throughput of single-cell anoikis assays and single-cell derived sphere formation by orders of magnitude utilizing hydrodynamic single cell positioning. Third, to investigate interactions between cancer cells and stromal cells, three **cell-cell interaction** platforms were developed. Innovations including control of interacting cell ratios, valveless isolation of co-culture using two-phase flow, continuous nutrient renewal enabled by 3D integration, and dual adherent-suspension co-culture were attained.

In addition, a **selective single-cell retrieval** technique that selectively detaches and retrieves targeted single cells has been developed for incorporation in our microfluidic platforms. The technique neither affects cell viability nor alters mRNA expression for qRT-PCR. These single cell platforms provide numerous advantages over traditional methods including: (1) ability to monitor and track individual cells, (2) control of various micro-environments on-chip for emulation of bio-processes, (3) accommodation of high-throughput screening, (4) capability to handle rare cell samples, and (5) potential to retrieve interesting single cells for further culture and analysis.

Chapter 1
INTRODUCTION

This chapter covers the importance of cancer cell heterogeneity and metastasis, the motivation of emulating bio-processes in-vitro by single cell microfluidic platforms, the goal of the research, and the outline of this thesis.

1.1 Cancer metastasis

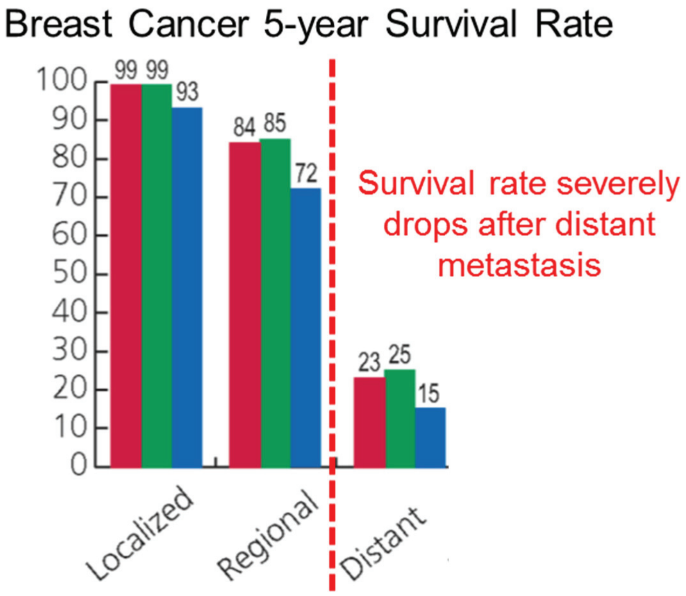

Fig. 1-1. 5-year survival rate of breast cancer with and without metastasis. [4]

Cancer, an uncontrolled growth of cells in vivo, is a leading cause of death in many developed countries. However, metastasis, rather than the cancer itself, is the real problem [1-4], accounting for nearly 90% of cancer related deaths. In the absence of metastasis, we can remove the tumor via surgery in many cases. In breast cancer, 5-year survival rates drop from 90% to 20% when distant metastases occur (Fig. 1-1) [4]. For this reason, it is critically important to investigate and understand mechanisms of metastasis in order to improve patient outcomes [5-7].

1.2 Conventional cancer metastasis assays

Conventionally, there are two approaches for studying metastasis: xenograft model and dish based assays. In xenograft model, cancer cells are injected into the abdomen of the mouse and observed to see how they spread in the body [8-9]. This method closely mimics the metastatic process in-vivo, but its high cost (around several hundred dollars per mouse) and long turnaround time (8 weeks) make it impractical to do large scale screening with this method. Though there are a number of dish based assay, the two most common approaches to study metastasis are Boyden chamber assays and wound healing assays [8-9]. In a Boyden chamber assay, cells are loaded on the top of a porous membrane, and their invasion through the membrane in traced. For wound healing assays, cells are removed from a small section in a cell monolayer, and their migration and time to migrate into the blank region is observed. These assays are low cost (price) and fast (time), but the conditions are less relevant to the real in-vivo scenarios. There is a fundamental trade-off between physiological relevance and throughput (Fig. 1-3). Xenografts are physiologically relevant but low throughput, while the dish based models are high throughput but less physiologically accurate. To address this issue, we have created single cell microfluidic platforms with both higher throughput and higher physiological relevance than dish based models for metastatic studies.

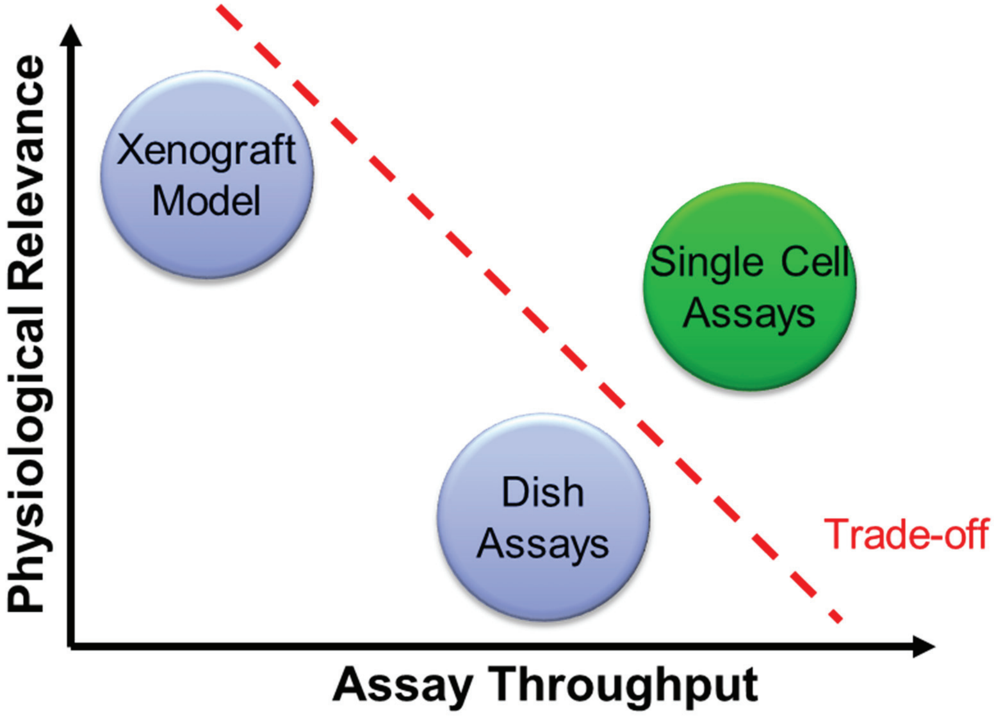

Fig. 1-2. The comparison between existing platforms and the proposed single cell microfluidic approach.

1.3 Cancer cell heterogeneity

In addition to higher throughput and better micro-environment control, single cell approaches enable the study of cancer cell heterogeneity. Recently, several studies have found significant heterogeneity among cells that were previously treated as essentially homogeneous [7]. Still, many assays and measurements are reported as averages over large numbers of cells. This assumption that all cells are identical, when they might really be a mixture of different cell subtypes, can lead to incorrect or at least imprecise and harder to replicate results [7]. Heterogeneity in cell populations poses a major obstacle to understanding complex biological processes.

Due to their genomic and epigenetic instability, cancer cells are highly heterogeneous; different sub-populations can have different potential to metastasize and generate new tumors [1]. Nevertheless, in the conventional assays, the behavior of small populations will be averaged out, so the results only represent the behavior of the majority. This is especially problematic as cancer relapse and metastasis may be caused by these small sub-populations in the tumor. To fully characterize the intra-tumor heterogeneity, there is an imminent need to develop new technologies for monitoring individual cell behavior in well-defined biological and chemical microenvironments.

1.4 Recent development in microfluidics

With the development of micro-fabrication, micro-structures fabricated in PDMS have proved invaluable for the creation of next-gen cell assays. Although microfluidic technology provides better control over microenvironment, higher throughput, and uses smaller volumes of reagents, many microfluidic platforms still load hundreds or thousands of cells for their assays. Thus, like conventional approaches, they still lack single cell resolution [10-18]. Droplet based technology, encapsulating drops of cell solution, can easily isolate single cells with very high throughput; [19-21] however, droplet based cell culture is not suitable for the study of mammalian cells. First, most mammalian cells are adherent cells; therefore, suspension in a droplet can lead to anoikis, resulting in cell apoptosis. [22] Second, it is difficult to continuously provide fresh media to each droplet, so the nutrition in the isolated droplets deplete over a short period of time. Recently, hydrodynamic cell capture schemes have been developed to enable single cell assays [23-25], but most of them lack precise micro-environment control (e.g. suspension culture, ratio controlled cell co-culture environment, isolation and flow control) to recapitulate the cancer niche. More importantly, though these single cell assays have the potential to investigate the heterogeneity within a tumor or cell line, most studies still treat the cells as a homogeneous population.

1.5 Research goal of microfluidic platforms

To facilitate the study of cancer metastasis, which is a complicated multiple-step process, we designed three types of platforms (a migration chip, a suspension culture chip, and multiple cell interaction chips) to study three main stages of metastasis (Fig. 1-3) [5-6]. The migration chip is used to study the process of cancer cell migration, from the primary tumor to the circulatory system. The single cell suspension culture platform is used to study cell survival in the circulatory system. Finally, the cell-cell interaction platforms are designed to study the process of secondary tumorigenesis, enhanced by tumor-stromal interactions. Utilizing the microfluidic technology, the presented platforms provide five key advantages (Fig. 1-4): (1) ability to monitor and track individual cells, (2) control of various micro-environments on-chip for emulation of bio-processes, (3) accommodation of high-throughput screening, (4) capability to handle rare cell samples, and (5) potential to retrieve interesting single cells for further culture and analysis.

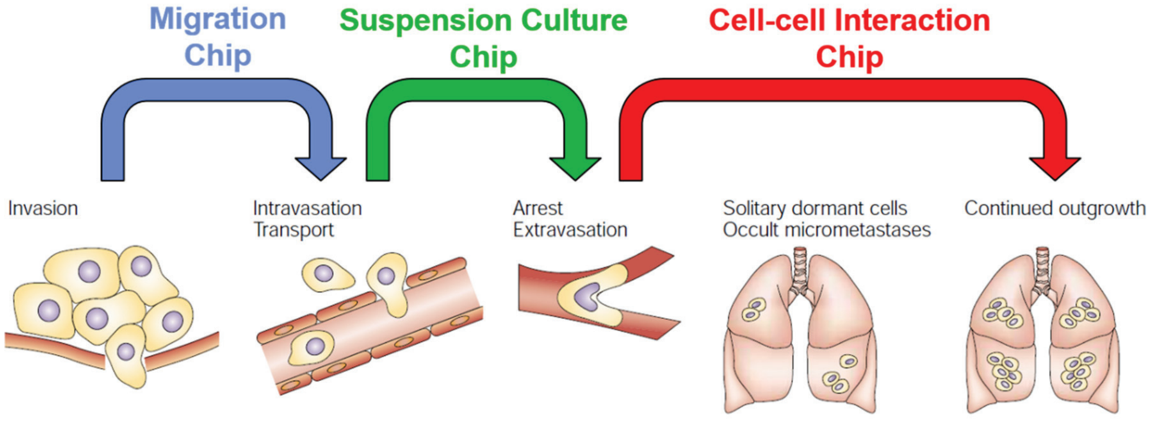

Fig. 1-3. The three stages of metastasis and the corresponding platforms for studying them. [6]

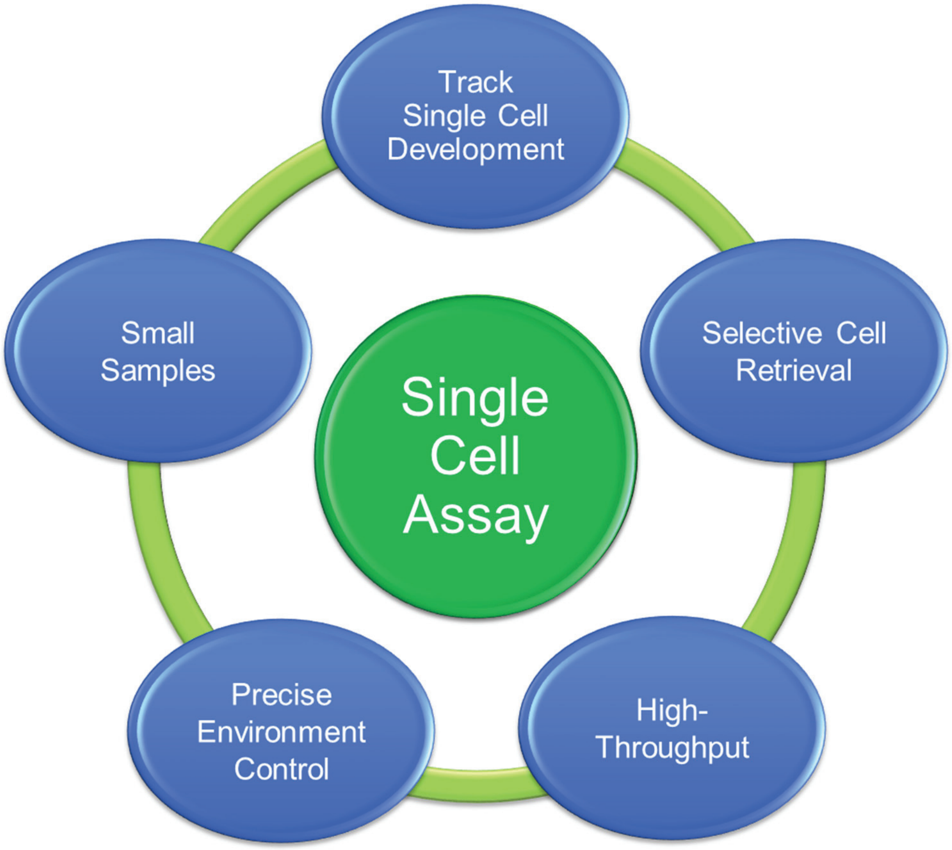

Fig. 1-4. Five key benefits of microfluidic single cell platform.

1.6 Selective cell retrieval for the studies of phenotypic cell heterogeneity

Conventionally, cell heterogeneity is studied by sorting and characterizing the cells with different surface markers using FACS and MACS instruments. Although these tools have very high throughput (million cells per hour), the markers used for sorting often may not correlate well with the cell behaviors that matter during treatment [26-29]. Using our microfluidic chips, we can observe the behavioral heterogeneity of cells, but it is difficult to retrieve the cells of interest from the microfluidics for further culture, xenograft, or analysis (e.g., mRNA gene expression, epigenome, protein). There are some selectively cell retrieval techniques using laser pressure microdissection, vacuum capillary suction, localized trypsin exposure, photo degradation of a film substrate, and ultrasound-induced cavitation [30-34], but unfortunately these approaches only work on open substrates. To make a selective cell retrieval tool that is compatible with microfluidics, we have investigated a photo-acoustic cell detachment mechanism utilizing nano-second pulsed laser to detach cells from a CNT-PDMS composite film. The detached cells can then be retrieved by precise microfluidic flow control for subsequent analysis. The mechanism was proven to have a negligible effect on cell viability and mRNA gene expression.

1.7 Thesis outline

The thesis covers two main topics: (1) microfluidic platforms for studying cancer metastasis at a single cell level (chapter 2 to chapter 6) and (2) selective cell retrieval by photo-acoustic detachment mechanism (chapter 7). The first topic includes the platforms that are used to emulate three critical stages of cancer metastasis on-chip, including the migration chip (chapter 2), the single cell suspension culture platform (chapter 3), and the cell-cell interaction platforms (chapters 4-6). The interaction platforms include cell ration control (chapter 4), two-phase isolation and 3D device integration (chapter 5), and dual adhesion and suspension culture environment (chapter 6). The second topic describes the tool developed for retrieval of interesting single cells from the microfluidic platforms. The cell retrieval technology can be and has been applied to the platforms developed in the previous chapters. The outline of each chapter is listed below:

The chapter 2 introduces the Single Cell Migration Chip, which can capture cells in each capture site and provide a chemical gradient to induce the migration of cells through a long capillary channel to model the migration process. The chip is designed to study cancer metastasis by measuring the motility and chemo-attraction of cells in an array of multiple migration channels. After the assay, the cells can be retrieved for further analysis.

Chapter 3 describes the Single Cell Suspension Culture Chip, which can capture 1,024 cells in an array at a single cell resolution and provide a suspension cell culture environment for these cells via polyHEMA coated surfaces that prevent cell adhesion. The platform can perform anoikis assays, which evaluate cell survival in suspension environment, and single cell derived sphere formation assays, which explore the tumor forming potential at a single cell level.

Chapter 4 covers the ratio controlled cell-cell interaction chip, which can precisely control the number of interacting cells and their type to accurately model cancer cell niches and provide spatio-temporal control of microenvironments for cell-cell interaction. To isolate chambers without using any valves or external pneumatic pumps, we introduced a novel actuation method by generating electrolytic bubbles to block the flow.

Chapter 5 introduces a single cell co-culture platform that implements actuation-free isolation using two-phase immiscible flows while providing continuous renewal of media through a semi-permeable membrane for long-term co-culture.

Chapter 6 covers a dual adherent-suspension co-culture device, which can provide both a suspension environment for cancer cells and an adherent environment for stromal cells in close proximity by selectively patterning polyHEMA in indented micro-wells. In addition, the platform specializes in high capture efficiency. Up to 75% of all cells in a small samples (50 cells) can be captured, granting the potential to study rare cell populations such as primary cells or circulating tumor cells.

Chapter 7 presents a novel cell detachment technique which provides good spatial resolution to selectively retrieve single cells from microfluidic chips. Pulsed laser beams were used to generate deformation on a CNT-PDMS composite film on which cells were adhered and cultured. Due to rapid (in milliseconds) deformation, cells can be detached in a non-thermal manner. This enables high cell viability and produces a negligible effect on the mRNA expression of single cell.

Chapter 8 concludes the thesis and discusses the future directions in the single cell assay chips.

Chapter 2
SINGLE CELL MIGRATION CHIP FOR HETEROGENEOUS CELL POPULATION

This chapter introduces the Single Cell Migration chip, which can capture cells in each capture site and provide a chemical gradient to induce the migration of cells through a long capillary channel to model the migration process. The chip is designed to study cancer metastasis by measuring the motility and chemo-attraction of cells in an array of multiple migration channels. After the assay, the cells can be retrieved for further analysis, and the cells.

2.1 Introduction

Cell migration is an essential process in angiogenesis, cancer metastasis, wound healing, inflammation, and embryogenesis. In particular, significant attention has been paid to the migration of cancer cells, since cancer metastases account for more than 90% of cancer-related mortality. [1-3] Cancer metastases result from a multi-step process with significant attrition of viable cells at each step in the metastatic cascade. One such step is the chemotactic intravasation of tumor cells from the tumor stromal to the capillary bed or lymphatic vessels. The response to chemoattractants and migration through these narrow microvessels and capillaries are both rate limiting steps for cells traversing through the metastatic cascade. The regulation of certain metastasis-related genes can also modulate the occurrence and number of metastasis. Although several have been discovered and may be potential targets for therapeutics, [4-6] the study of metastasis-related genes still largely depends on xenograft mouse models, which require considerable time and cost and may be difficult to adapt to personalized therapy. [7, 8] Single cell resolution and visualization are also at present impractical in xenograft-based experiments. Hence, there is an unmet need to develop *in-vitro* devices which can realistically emulate critical steps of the metastatic cascade, especially intravasation into and migration through blood and lymphatic capillaries. [9]

Popular approaches for studying cell motility *in-vitro* such as wound healing and Boyden's assays have significant limitations. [10, 11] Wound healing assays present challenges both in the non- repeatability of the execution of the scratch across the plate and in its inability to discern the more motile from the less motile cells. [12] Boyden chambers provide quantitative binary motility results in large cell populations, but imaging of the actual migration process of the individual cells is not possible. These fundamental limitations preclude the use of these assays to understand, in detail, the motility of cancer cells under conditions that more closely mimic the metastatic cascade. Taking advantage of modern microfabrication technologies, a number of recent studies have employed microfluidic channels to study cell migration. [13, 14] Different channel cross-sectional sizes and geometries have been used to study the effects of geometry on cell migration. [15-18] The hydrogel- or extra-cellular matrix was filled within the migration channel to simulate the cancer invasion process in the tissue. [19, 20] In some approaches, two or more cell types were co-cultured in microfluidic channels to approximate the cellular diversity in the tissue micro-environment. [21, 22] However, these previous microfluidic approaches which study collective migration behaviors, lack the capability to trace single cell behavior and investigate cell heterogeneity in motility.

Cellular heterogeneity is a key characteristic of cancer. [23] Due to the genomic mutation or epigenetic regulation, [24, 25] each cancer cell has distinct behaviors, including cell motility. It is hypothesized that cells that undergo an epithelial-to-mesenchymal transition (EMT) can exhibit elavated motility and contribute metastasis. [26-30] Because of the importance of motility in metastasis, effective suppression of the EMT has potential as a therapeutic strategy. [28-30] As researchers have begun recognizing the importance of cellular heterogeneity in metastasis, several papers reported the techniques to study the migration behavior at a single cell level. However, these platforms suffer from low capture efficiency, loading many cells but only investigating a small portion. This wastes many cells, which is unfavorable for applications using rare samples. More importantly, these platforms do not allow the retrieval of the cells after migration assay for further downstream analysis, preventing understanding of the fundamental causes of elevated motility.

To overcome these limitations, we designed an innovative single cell migration platform that incorporates a single cell capture scheme. This scheme positions one cell at the entrance of each migration channel, so the migration behavior of each individual cell can be easily traced. Using this cell positioning technique, the assays can be performed by monitoring 20 captured cells, making the platform favorable for use with primary samples and other rare cells. In addition, after the migration assays, both highly motile cells and non-motile cells can be retrieved for further downstream analysis. We have demonstrated that the highly motile cells selected in the migration assay maintain this behavior off-chip.

Lastly, we have demonstrated the capability to customize migration channels, which facilitates emulation of lymphatic capillaries for the study of metastasis regulating genes.

2.2 Design of the single cell capture scheme

The single cell motility microfluidic device consists of single cell capture sites and migration channels. Fig. 2-1 (A) shows a schematic diagram of the proposed chip and fabrication processes. To achieve single cell resolution, cells are loaded by gravity flow and hydrodynamically captured at each capture site (Fig. 2-1 (B)) by cellular valving. Although the hydrodynamic cell capture was previously reported, [33,34] we incorporated an capturing design right next to the entrance of a narrow migration channel. As shown in Fig. 2-1 (C), two paths are created in the design: a central path and a serpentine path. The hydrodynamic resistance of each path is inversely proportional to its flow rate. A long serpentine structure increases the hydrodynamic resistance (R_S), so the serpentine flow resistance is larger than that of the central path. Therefore, the serpentine flow (Q_S) is less than the central flow (Q_C), and cells will more likely follow the central path. Since the opening of the central path is slightly smaller (Height: 20 μm, Width: 10 μm) than the size of cancer cells (e.g., SKOV3 cells has an average diameter of 14.1 μm, SD ±3.2 μm), the captured cell easily plugs the gap and blocks the flow through the central path. Thus, the rest of the cells will travel through the serpentine path and will be subsequently captured in the downstream capture sites (Fig. 2-2). We simulated the pressure and velocity field for various channel geometries (Fig. 2-3). Based on the simulation, we optimized the length of the serpentine path to achieve a high cell capture rate. To optimize the cell capture rate in this asymmetric capturing design, the media in the right inlet (80 μL) is slightly less than that in the left inlet (100 μL). The resulting weak flow rightward into the migration channel can guide the cells closer to the capture site to increase the capture probability.

Fig. 2-3 shows the simulation of the pressure and flow velocity under varying serpentine lengths ranging from 200 μm to 800 μm. Ideally, the greater the hydrodynamic resistance of the serpentine path (R_S) (which is proportional to the serpentine length) the higher the capture rate is. However, when the serpentine length is longer than 800 μm, the hydrodynamic resistance of the serpentine path (R_S) becomes so large that the flow velocity drops significantly. In this case, cells may get easily stuck along the serpentine path, resulting in clogging, which in turn significantly degrades the capture rate. As a result, there is a large standard deviation of capture rates observed in chips with long serpentine lengths. From these results, the optimal serpentine length was determined, and we have achieved high capture rates of over 94% (capturing exactly one cell per each migration channel) with a serpentine length of 600 μm (Fig. 2-1 (D)). The stiffness of the cells of interest is also critical for optimal cell capture. More elastic cells yield higher capture rates since they deform more easily and plug the central path, sealing the capture site better than stiff cells. Based on the particular cell types used in the experiments, the geometry of serpentine lengths and path openings were modified to improve capture efficiency, as described in the supplementary methods. Extensive studies have been done on various cell types including SKOV3, A2780DK, C2C12, MDA-MB-231, and PC3 cells, and we have achieved a capture rate higher than 85% in all the tested cell types (Table 2-1). This experimental data demonstrate that the proposed single cell capture mechanism is reliable and robust for a broad spectrum of cell types, and thus amenable to the study of cancer metastases.

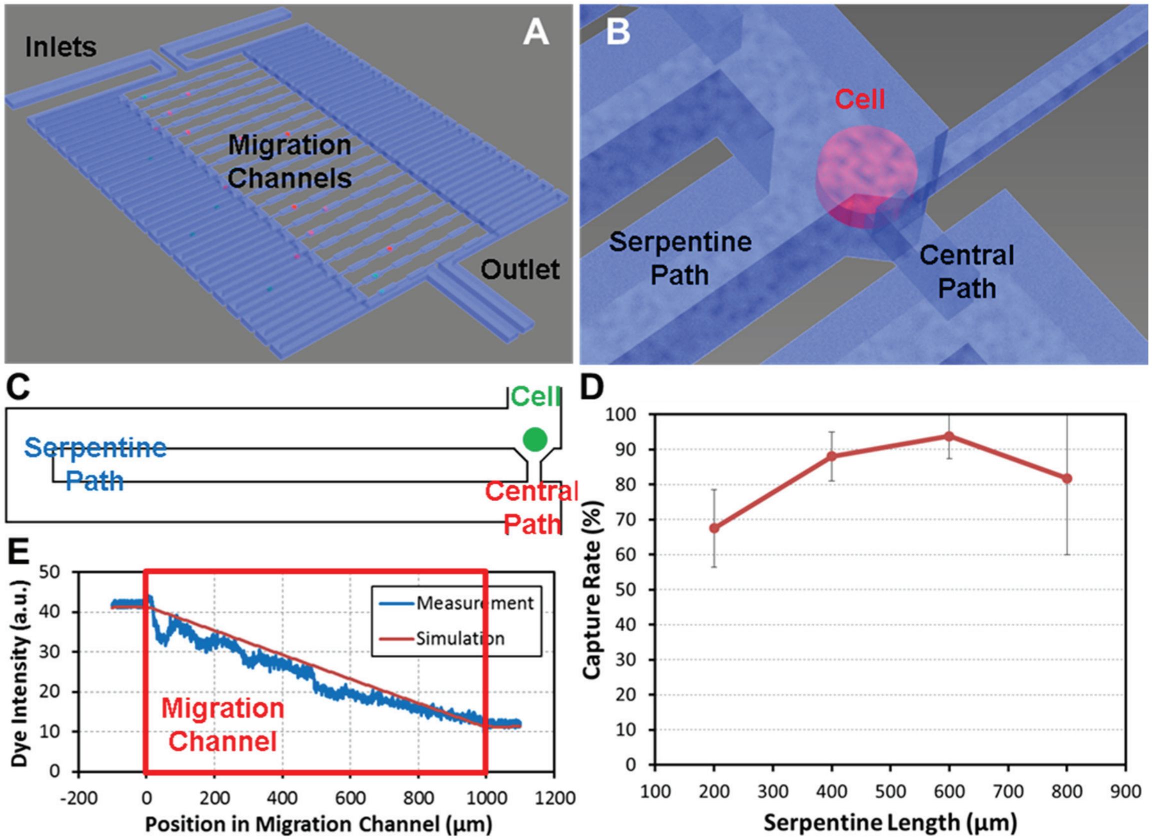

Fig. 2-1. Presented microfluidic chip for single cell migration. (A) 3D schematic drawing of the chip. During cell loading, the culture media containing cells flows from left inlet to the outlet, and cells are captured in an array of cell culture sites along the left side. After cell loading, the left inlet media is replaced by pure culture media, and the chemo-attractant spiked media is injected into the right inlet. (B) Enlarged 3D schematic drawing of one cell capture site. (C) Schematic of the cell capture principle. Two paths are designed for single cell capture. The central path has lower hydrodynamic resistance than the serpentine path, so the incoming cells will be diverted to and captured at the central path. Since the opening of the central path is smaller than the cell size, the captured cell blocks the central path acting as a valve. The next incoming cells will flow through the serpentine path and get captured in the subsequent downstream capture sites. (D) The capture rate of the migration chip with different serpentine lengths. The longer the paths are, the higher the hydrodynamic resistance (RS) becomes, which can enhance cell capture by the central path. However, when the serpentine length is longer than 800μm, the hydrodynamic resistance of the serpentine path (RS) becomes too high, and the slow flow may lead to cell clogging, which can significantly degrade the capture rate. The optimal length determined from these experiments is 600 μm. (E) Concentration gradient of chemicals in the migration channel. The red line indicates the simulation result by COMSOL 3.5. The blue line is the measurement of the fluorescent dye (Fluorescein 5(6)-isothiocyanate, F3651, Sigma-Aldrich) intensity in the migration channel, which correlates well with the simulation.

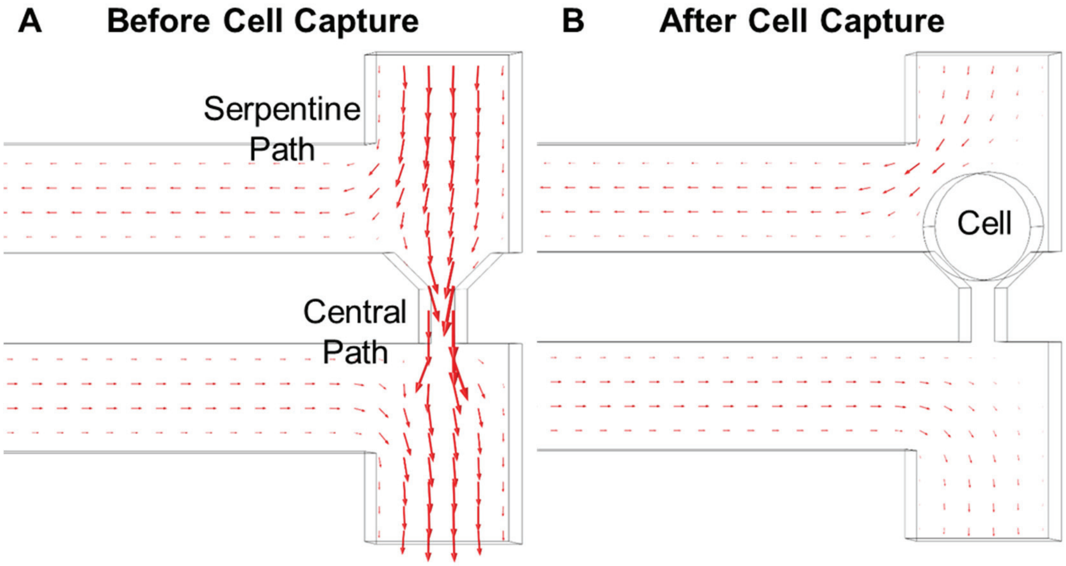

Fig. 2-2. Simulations of flow velocity before and after capturing one cell by COMSOL 4.3: (A) Before cell capture, simulation of flow velocity shows that the higher flow rate through the central path, so the cells will more likely follow the central path. (B) After capturing one cell, the captured cell plugs the gap and blocks the flow through the central path. Thus, the rest of the cells will travel through the serpentine path and will be subsequently captured in the downstream capture sites.

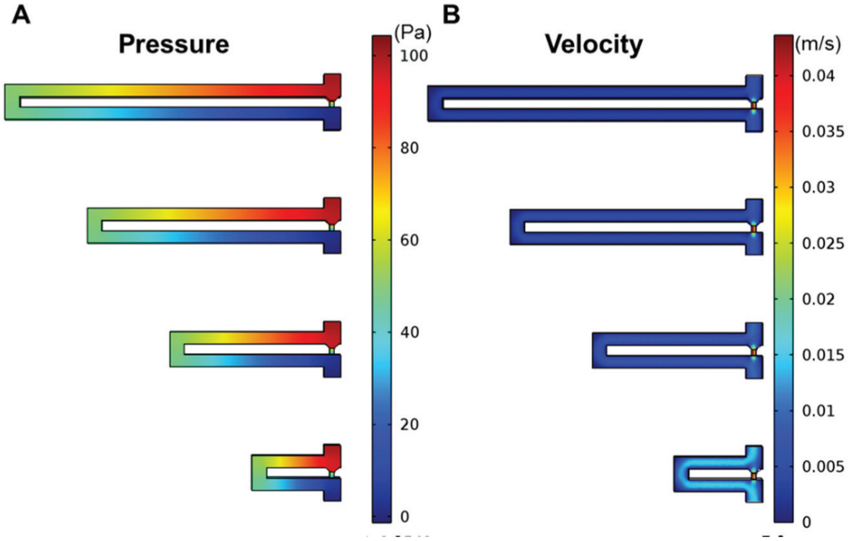

Fig. 2-3. Simulations of flow velocity and pressure on different serpentine lengths ranging from 200 μm to 800 μm by COMSOL 4.3: (A) Simulations of pressure distribution illustrates that the quick transition in the capture site leads to a high capture probability of single cells at the site. (B) Simulations of flow velocity indicates that when the serpentine structure is short, the flow rate through serpentine path becomes higher, which means that the cell is less likely to be driven to the capture gap.

Table 2-1. Capture rates of five cell lines among four different cell types. The capture rates of all five cell lines are higher than 85%. Since the skov3, C2C12 and MDA-231 cells are more elastic than A2780DK and PC3 cells, it is easier for them to squeeze into the capture site and block the path. Thus, the capture rate of these elastic populations is higher.

	Cell Type	Capture Rate
Skov3	Ovarian cancer cell	93.8±6.4 %
A2780DK	Ovarian cancer cell	88.6±10.2 %
C2C12	Mouse muscle myoblast	92.2±4.5 %
MDA-231	Breast cancer cell	91.5±7.2 %
PC3	Prostate cancer cell	85.1±9.7 %

2.3 Chemical gradient generation

The migration of cancer cells can be driven by chemotaxis, whereby differences in the concentration of growth factors and chemokines can drive tumor cells to intravasate into the circulatory system. [35] To emulate this condition, the migration channels (Width: 10 μm, Height: 40 μm, Length: 1 mm) are designed to study the movement of cells, and an artificial concentration gradient profile is generated by diffusion. [36] To generate the chemical concentration profile to induce cell migration, culture media with chemo-attractants is pipetted into the right inlet, and the serum free culture media (pure DMEM or RPMI) is pipetted into the left inlet. Due to the nature of diffusion, the concentration of the chemo-attractant in the migration channels increases linearly along the channel from left to right (Fig. 2-4). The generated chemical profile projected in the simulation is confirmed experimentally using a fluorescent dye (Fluorescein 5(6)-isothiocyanate, F3651, Sigma-

Aldrich). The fluorescent intensity is measured and plotted in Fig. 2-1 (E). The measured fluorescent concentration profile matches well with simulation (COMSOL 3.5), verifying that concentration profiles can be successfully generated. Additional simulations were performed to investigate whether a migrating cell in the channel can affect the gradient profile. A pseudo-cell (10 μm width by 10 μm height and 40 μm length) was added to the model to simulate a potentially blocked channel. However, since the channel cross-section (10 μm by 40 μm) is much larger than that of a cell, the gradient is changed by less than 2% as shown in Fig. 2-5.

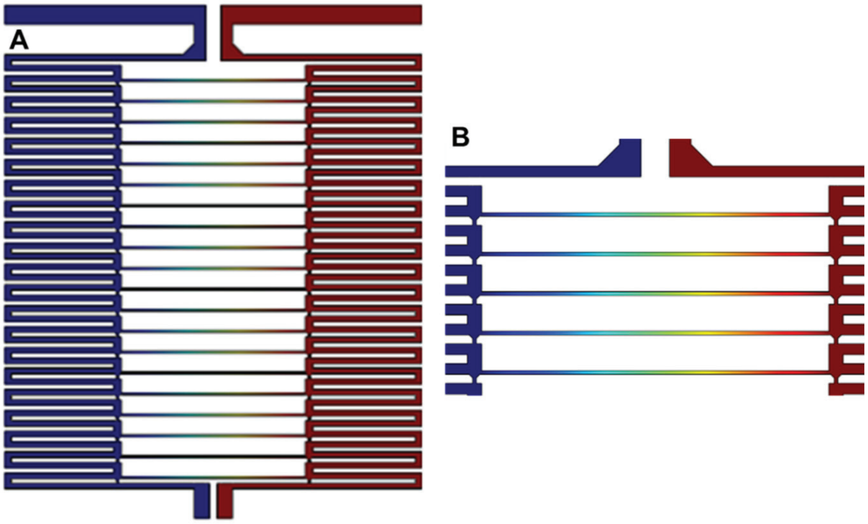

Fig. 2-4. Simulations of chemical concentration gradient generated in the device by COMSOL 3.5. (A) The simulation of the whole chip demonstrates that the chemical concentration is uniform from the upstream to the downstream since the diffusion is relatively slow. (B) Enlarged view of the first few channels. The simulated concentration profile shows the linear chemical gradient is formed in the migration channel. Concentrations are shown in color scale with red being 1 M chemokine and blue being 0 M chemokine.

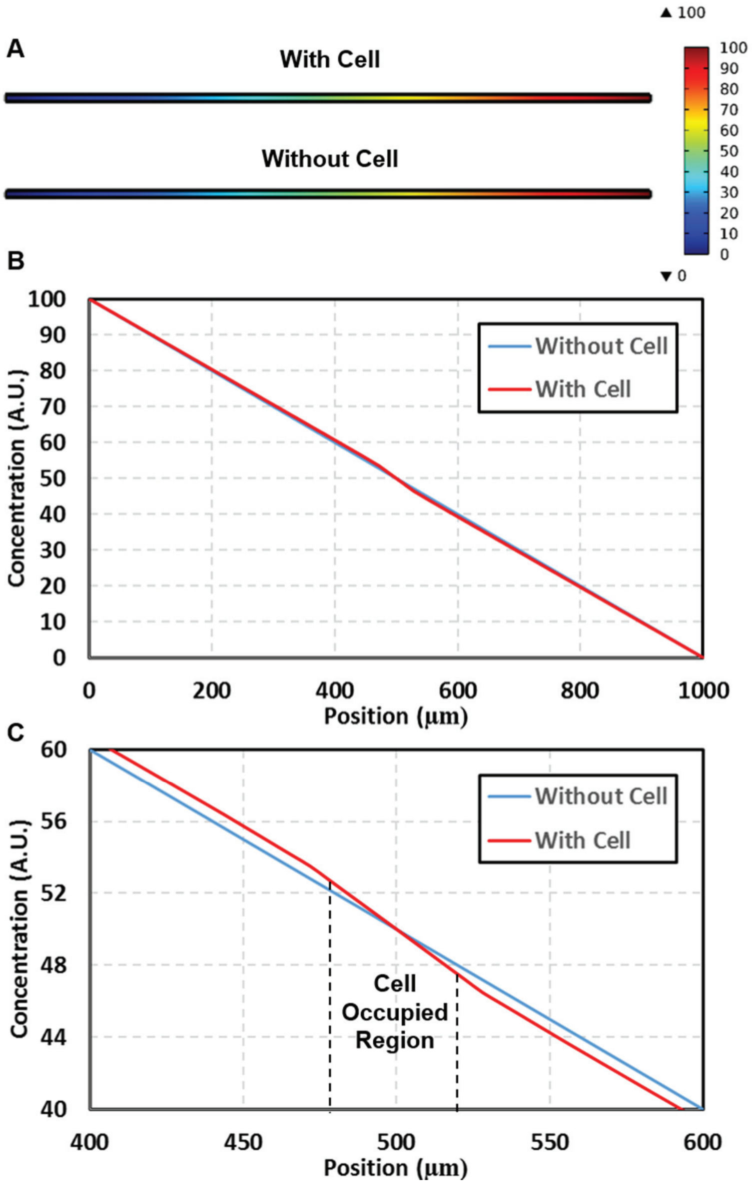

Fig. 2-5. Simulations of chemical concentration profile with and without cell migrating in the migration channel. (A) The simulation of the chemical concentration profile with and without cell migrating in the migration channel. The cell was emulated by adding a pseudo-cell (10 μm width by 10 μm height and 40 μm length) on the bottom of the channel to block diffusion. The cell was placed at the center (500 μm from the left) (B) The concentration profile in the channel. (C) Enlarged concentration profile in the channel from 400 μm to 600 μm position. Since the channel cross-section (10 μm by 40 μm) is much larger than cell, the cell can alter the concentration by less than 2%.

2.4 Single cell migration assay

Cancer metastases are caused by a multi-step process which begins with the escape of tumor cells from the primary tumor and the subsequent intravasation of cancer cells into capillary vessels as induced by chemo-attractants. [35] Competition with these chemo-attractants or inhibition of the receptors for these regulating signals can be potential strategies for cancer treatment. [40, 41] The platform presented herein provides the capability to investigate putative chemo-attractants and the efficacy of drug treatments in inhibiting motility. In order to validate the utility of the fabricated migration chip, we demonstrated chemotaxis of SKOV3 cells induced by Hepatocyte Growth Factor (HGF), which is a well-known chemo-attractant for many cell types. [42]

Fig. 2-6 (A, B) illustrates the single cell migration tests in the platform. During cell loading, all the captured SKOV3 cells were positioned at the capture sites along the left side as shown in Fig. 2-6 (A). The captured cells attached to the substrate within three hours, and the cell chemotaxis was monitored over 24 hours at single cell resolution, as shown in the Fig. 2-6 (B). After cell loading, the media in the right inlet was replaced with media supplemented with 50 ng/mL HGF, which can induce the SKOV3 cell migration. [43] Pure media was pipetted into the left inlet, creating a linear concentration gradient of HGF. After 24 hours, we observed that more cells migrated to the right side when exposed to the HGF concentration gradient, while the control (applying culture media to both inlets) did not show any directional migration (Fig. 2-6 (A)). The statistical analysis is plotted in Fig. 2-6 (C). This preliminary data demonstrates that the presented single cell platform is suitable for the studies of single-cell chemotaxis.

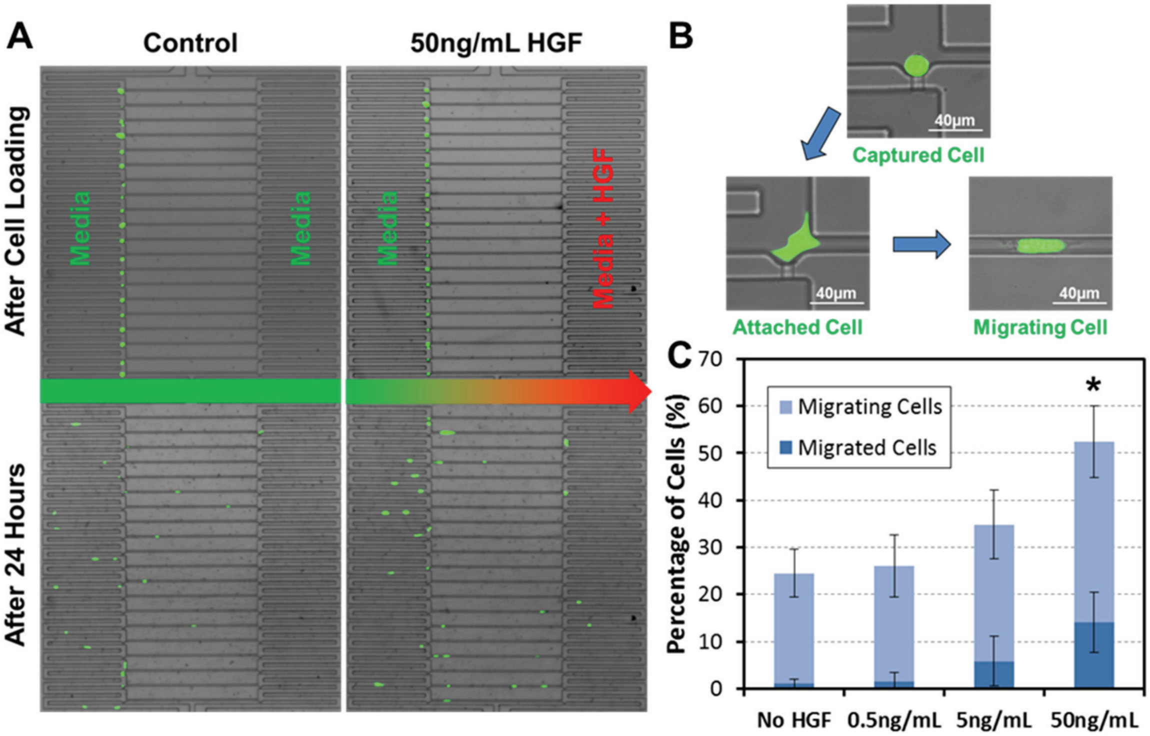

*Fig. 2-6. Single cell migration assay with HGF as a chemoattractant. (A) The images of the single cell migration assay. The upper two images illustrate the cell distribution after cell loading. (Cells were loaded from the left channel.) All captured cells are aligned along the left side of the migration channels. The lower two images illustrate the cell distribution after 24 hours with the same media in both sides (lower left, control) and with HGF of 50ng/mL added to the right inlet (lower right, stimulated). Compared to the control, the HGF induced cells to migrate more to the right. (B) Process of cell migration. First, a cell is captured by the hydrodynamic force from the cell solution. After 4-6 hours the cell attaches to the substrate and then it begins to move into the migration channel. (C) Result of the chemoattractant assay. The graph illustrates the relative ratio of migrated cells (all the way to the opposite side) and migrating cells (within the channel) vs. HGF concentration. The result confirms that the HGF is a strong chemo-attractant to the skov3 cells. Data points represent means ± standard deviations (N= 4 devices), * refers to P < 10-4.*

2.5 Selective cell harvesting for downstream cellular heterogeneity analysis

Cellular heterogeneity is a key characteristic of cancer, meaning each cell in a primary tumor or even a cancer cell line has its own distinct behaviors. The difference can come from genomic mutation or epigenetic regulation such as epithelial-to-mesenchymal transition (EMT). In our single cell migration platform, we can easily monitor the movement of each single cell, specializing in the studies of cell heterogeneity. After performing migration assays, we can selectively harvest both highly motile cells and non-motile cells for downstream analysis. This capability grants the opportunity to analyze the causes of heterogeneity in motility.

Although MDA-MB-231 is a motile breast cancer cell line, some cells still have higher motility than others. Both highly motile and non-motile MDA-MB-231 cells were retrieved as illustrated in Fig. 2-7 (A). Fig. 2-7 (B) shows a highly motile MDA-MB-231 cell, which had migrated to the serpentine channel in the right side within 24 hours. To selectively harvest highly motile and non-motile cells, we flowed trypsin from the outlet to the inlet, detaching and directing motile cells to the right inlet, while the non-motile cells that remain in the left side, will be directed to left inlet. After 3 minutes of trypsinization in the incubator, the cells became rounded, indicating successful trypsinization (Fig. 2-7 (C)). After 5 minutes of trypsinization, the target cells were detached, retrieved from the inlet, and transported to the 60 mm petri dish for recovery (Fig. 2-7 (D, E)). After 12 hours recovery, E-Cadherin and DAPI staining was performed on the retrieved cells. The highly motile cell had weaker E-Cadherin expression than that of non-motile cells, indicating EMT-like behavior (Fig. 2-7 (F, G)). [28-30] 4 days after the retrieval, the single cells grew into distinct colonies containing 30-40 cells (Fig. 2-7 (H, I)). Comparing the colonies formed by highly motile cells and non-motile cells, we found that the harvested highly motile cells maintain EMT-like morphology even after forming a colony. In that colony, cells were mostly elongated and spread wider than those in a colony formed by non-motile cells. Significant difference in the colony radius was observed between the two types of colonies (Fig. 2-7 (J)), while no significant difference in the proliferation rate was seen

(Fig. 2-7 (K)). This validates the larger colony radius was caused by the EMT-like morphology rather than higher proliferation rates.

To examine whether the difference in motility was maintained after cell retrieval and culture, single cell migration assays were performed on the retrieved sub populations. Although we only have a small (<1,000) number of cell harvested from early (Day 7) colonies of sorted cells, our single cell migration chipcan efficiently use such a small sample, as only 20 cells are needed for analysis. The descendant cells of highly motile cells were still significantly more motile than those of non-motile cells when assayed under the influence of a 10% FBS chemotactic gradient (Fig. 2-7 (L)), while no significant difference was observed between the descendant cells of the non-motile cells and the unsorted bulk cells. These preliminary results demonstrate that the distinct characteristics of sorted cells are maintained after the harvesting process, allowing further downstream studies on the differences between highly motile and non-motile cells.

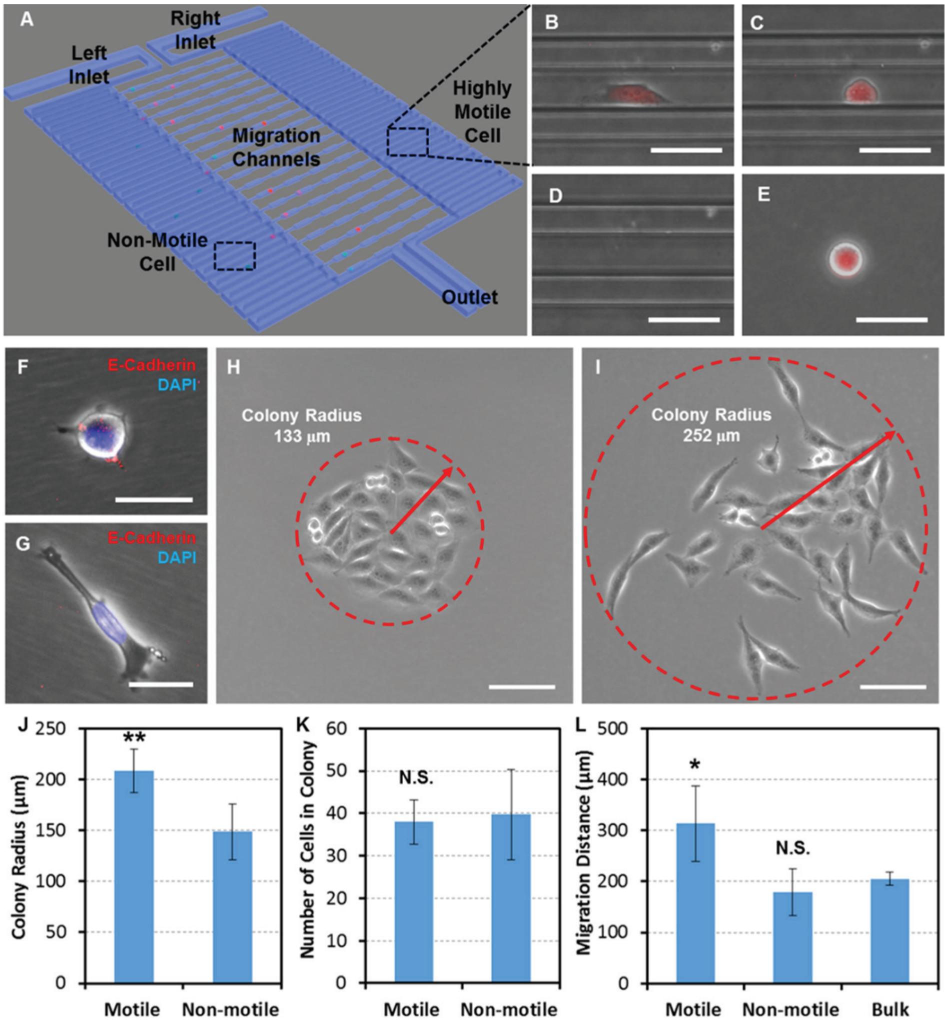

*Fig. 2-7. Selective retrieval and downstream analysis of highly motile cells. (A) The schematics of cell retrieval. (B) Two highly motile cells, which have migrated through the migration channels within 24 hours. (scale bar: 50 μm) (C) After 3 minutes trypsinization, the cells became rounded morphology. (scale bar: 50 μm) (D) After 5 minutes trypsinization, the cells were successfully detached and flowed to the right inlet. (scale bar: 50 μm) (E) The detached cell transferred to the 60mm petri-dish. (scale bar: 50 μm) (G) E-Cadherin and DAPI staining of non-motile cell after retrieval (scale bar: 20 μm) (H) E-Cadherin and DAPI staining of highly motile cell after retrieval (scale bar: 20 μm) (H) The colony formed by single non-motile cell after 4 days. The cells in the colony tightly connected together. (scale bar: 100 μm) (I) The colony formed by single highly motile cell after 4 days. The cells maintaining elongated (mesenchymal-like) morphology, and the cells spread widely. (scale bar: 100 μm) (J) The comparison of the colony radius between highly motile and non-motile cells. The colonies formed by motile cells have significantly larger radius. (N = 8 colonies), ** refers to $P < 0.01$. (K) The comparison of the number of cells per colony between highly motile and non-motile cells. No significant difference was observed. (N = 8 colonies) (L) The migration distance of single cell migration assays. Descendants of highly motile cells still more motile than the descendants of non-motile cells and unsorted bulk MDA-MB-231 cells (N = 5 devices), * refers to $P < 0.05$.*

2.6 Customized migration channel for emulating lymphatic capillaries

With the presented platform, we are also capable of customizing the migration channel in order to emulate cell migration through various tissues. The lymphatic capillary invasion process is a critical step in the metastasis of cancer through to the lymph nodes, so we designed narrow channels with choke points to emulate lymphatic capillaries [43]. As a further demonstration of the proposed device's capabilities, we studied a mitogen activator of protein kinase (MAPK) family members, p38γ, and its role in breast cancer cell migration. The MAPK members, including p38γ, are known to be involved in cell motility signaling pathways. Additionally, p38γ mRNA is overexpressed in several types of cancer and helps increase Ras-induced cancer invasion. Knockdown of p38γ genes degrades the efficiency of lymph invasion *in-vivo*, partly due to drastically changing the type of motion the cell can undergo [45]. It is believed that p38γ knockdown leads to ubiquitination and degradation of Ras homology gene family member C (RhoC) [45, 46]. Due to a lack of RhoC, the knockdown cells (GKD) are unable to form long pseudopodia and thus engage in unproductive cytoskeleton cycling that does not effectively lead to cellular displacement. The resulting unorganized cytoskeleton reduces the efficiency of cell movement. To characterize the invasion capability of MDA-MB-231 (breast cancer) cells in a 3D model of lymphatic capillaries, we designed a single cell migration chip that contains multiple migration resistance choke points and successfully demonstrated the capability of tracing single cells in this lymphatic capillary invasion assay (Fig. 2-8 (A)). The size variation of the migration channels and choke points are illustrated in Fig. 2-8 (B)

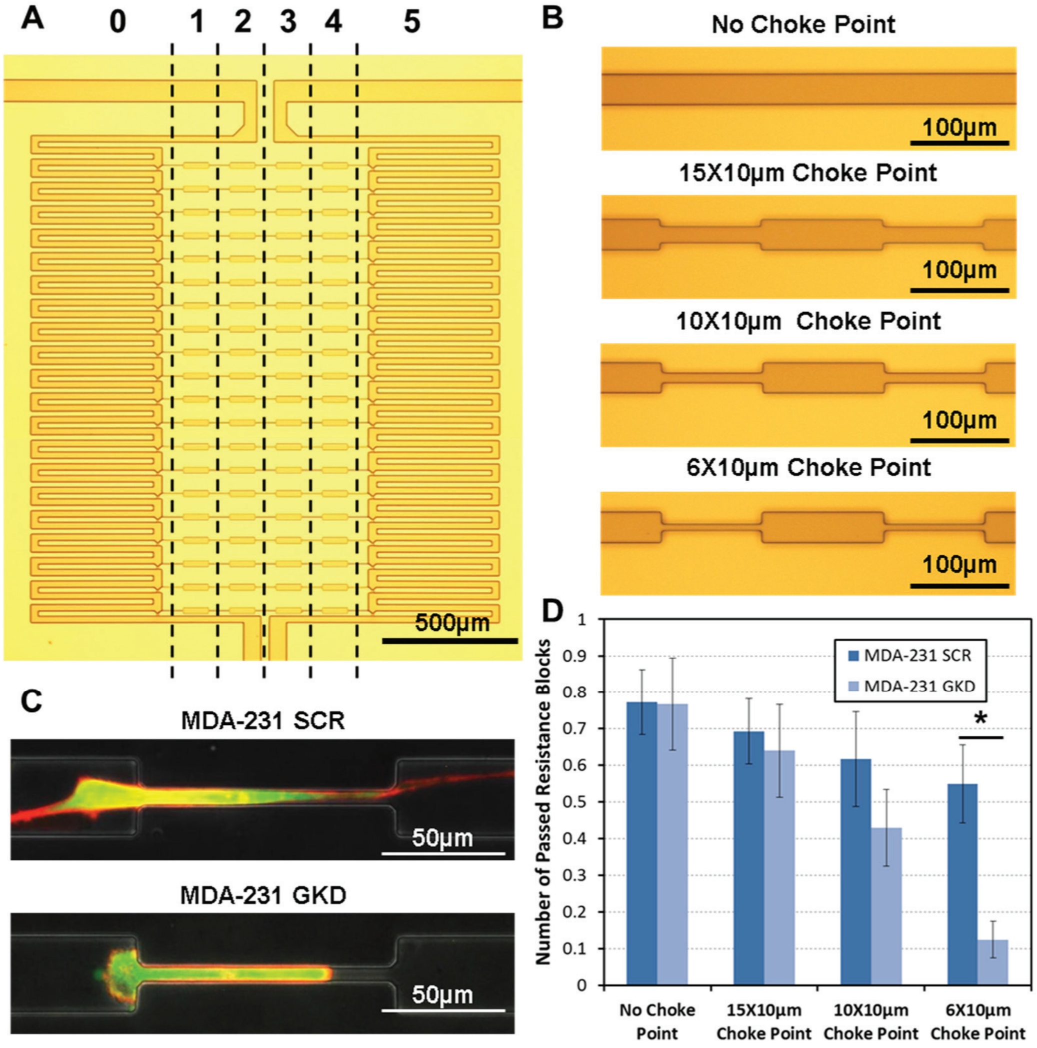

*Fig. 2-8. Customized migration channels for emulating lymphatic capillaries. (A) Microphotograph of the fabricated device. The cells are loaded in the left side, and the chemo-attractant induces the migration through migration channel to the right. (B) Size variation of migration channels. The length of choke point is 100 μm, and the width of choke point varies from 6 μm to 30 μm. It is difficult for cells to migrate through the narrow choke point, which is similar to the geometry of lymphatic capillaries. Thus, the ability to migrate through the narrow choke point can be used to predict the invasion potential. (C) Qualitative observation of migration behavior of MDA-MB-231 cells (F-actin is labeled by RFP) in the 6 μm x 10 μm choke point. The scrambled (SCR) cells can form a stable and long stress fiber to migrate through the choke point, while the p38γ knockdown (GKD) cells can only deform into the choke point. (D) Single cell migration assay on different channel geometries. We measured the average number of choke points passed by SCR and GKD cells for various choke point dimensions with 20% FBS as an chemoattractant. The motilities of both cells are similar in the straight channel, but the SCR MDA-231 cells are far more motile in the narrow channel. This result predicts the higher invasion potential of SCR MDA-231 cells in-vivo. Data points represent means ± standard deviations [N= 8 devices), * refers to P < 10-5.*

First, we observed cell migration behavior in the narrow choke point migration channels with a choke point of 6 μm x 10 μm. Fig. 2-8 (C) shows the representative morphologies of scrambled vector (SCR) cells and p38γ knockdown (GKD) cells. F-actin fibers are labeled by RFP red fluorescence. Since SCR cells were able to form long pseudopodia past the choke point in a mesenchymal-like manner, the cells were successful in migrating through the narrow channel by contraction of the stress fibers in the typical "rubber band-like" fashion. Due to the lack of RhoC and other global effects of p38γ knockdown, the GKD cells could only squeeze into the narrow channel with the actin evenly distributed around the periphery of the cell but could not form pseudopodia. The SCR cells are much more mesenchymal in nature whereas the GKD cells exhibit an epithelial pattern. Next, we measured the cell migration distance (as a function of "passed choke points" or relative distance in the channels) for multiple choke point geometries, as shown in Fig. 2-8 (D). Since hepatocyte growth factor (HGF) may also regulate RhoC and confound the results, in this experiment, we used 20% serum (FBS) media as the chemoattractant [46]. We observed that SCR and GKD cells have a similar motility when the migration channel is wide (30 μm x 10 μm) and without choke points, but the motility of GKD cells significantly diminishes when the channel is obstructed by narrow choke points (6 μm x 10 μm). To verify the lower migration efficiency of p38γ knockdown cells, the velocity of MDA-MB-231 cells in the narrowest choke point channel (6 μm x 10 μm) is measured and shown in Fig. 2-9. Although the variation is large, the velocity of SCR cells is almost double that of GKD cells. This result reaffirms the hypothesis that the motility of GKD cells decreases due to a lack of RhoC, which causes unproductive actin cytoskeletal cycling. This experiment demonstrates the potential of the proposed single cell platform for studying models of cell migration through geometrically constrained tissues and the ability to discern cellular motility differences as a result of gene knockdown.

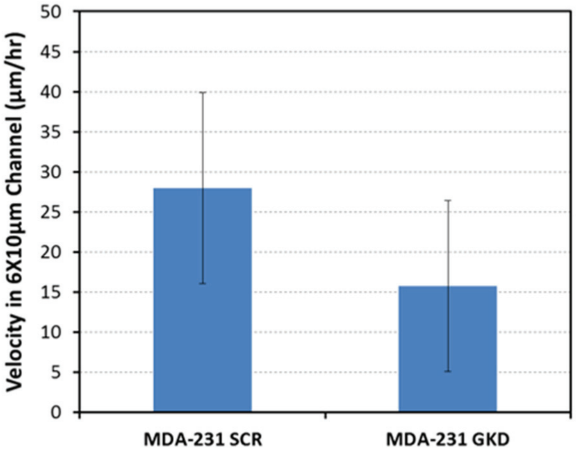

Fig. 2-9. The migration velocity of MDA-MB-231 cells in the 6 µm x 10 µm choke points. The scrambled (SCR) cells can migrate more efficiently than the p38γ knockdown (GKD) cells through the choke point.

2.7 Chapter Summary

There are many microfluidic devices for cell migration have been reported in recent years. Although these works exploit the advantages of microfluidics (small volume and precise micro-environment control), most assays still measure the average behavior over large numbers of cells with an underline assumption that all cells are identical. This leads to incorrect, or, at least, imprecise results. Cell heterogeneity is an important part of what makes cancer treatment difficult and complicated. The microfluidic tool presented has the potential to distinguish and characterize individual cell behaviors. Here, we demonstrated single-cell migration, investigating individual properties of each cell rather than the average behavior. After the assays, cells of different motility can be selectively retrieved for further downstream analysis.

The presented tool can reliably position exactly one cell right next to the channel, granting the advantages of using small number of cells and allowing easily tracing of single cell migration behavior. We incorporated the hydrodynamic scheme with migration channel, so single cells can be positioned right next to the narrow migration channel the assays. Through optimization we can achieve 90% capture rates in 5 different mammalian cell lines. As only 20 cells need to be monitored for analysis, the assays can be performed by small number of cells. In addition, the chemo-gradient profile can be reliably generated in the narrow migration channels, and a migrating cell in the channel has limited effect on the concentration profile. Using presented platform, we have successfully demonstrated three single-cell migration assays: tracing SKOV3 cells chemotaxis induced by HGF, studying MDA-MB-231 cancer cell heterogeneity in motility, and studying metastasis-related genes (p38γ) by evaluating their effect on migration in the artificial lymphatic capillaries.

In addition to single cell migration assays, the platform also provides a method for motility based cell behavioral sorting. Highly motile and non-motile cells can be selectively retrieved after migration assay, and the retrieved cells were proved to be viable for staining and culture. The preliminary results demonstrate that the distinct characteristics of sorted cells are maintained after the harvesting process, allowing for further downstream studies in the difference between highly motile and non-motile cells. We demonstrated that the heterogeneity in a cell line, and the presented platform provides the capability to study this heterogeneity and the potential to correlate the motility behavior with the molecular signature of single cells.

Chapter 3
SINGLE CELL SUSPENSION CULTURE USING POLYHEMA COATING FOR ANOIKIS ASSAY AND SPHERE FORMATION

This chapter describes the Single Cell Suspension Culture chip," which can capture 1,024 cells in a chip at a single cell resolution and provide a suspension cell culture environment for these cells via polyHEMA coated surfaces that prevent cell adhesion. The platform can perform anoikis assays, which evaluate cell survival in suspension environment, and sphere formation assays, which indicate the tumor forming potential at a single cell level within a population.

3.1 Introduction

Since metastatic cancer accounts for more than 90% of cancer-related mortality, targeting cancer metastases can greatly improve patient prognosis [1,2]. Although inhibiting metastatic capacity is critical for successful therapy, pre-clinical studies are limited in throughput due to extended time periods and high cost of xenograft models [3]. Hence, there is an unmet need to develop in-vitro devices that can emulate aspects of metastasis, study critical signaling pathways in metastasis, and test therapeutic interventions. Conventional in-vitro assays of metastasis focus on cancer cell migration and invasion [4,5], though that only represents the early stages of cancer metastasis1. After migration from primary tumors to the circulatory system, cancer cells need to survive in suspension and then re-grow into a micro-metastasis once suitable secondary sites are reached.

For normal and pre-malignant cells, adhesion to the extracellular matrix (ECM) is essential to maintain cellular homeostasis, and disruption of cell attachment leads to anoikis, a form of programmed cell death[6]. In order to successfully metastasize, tumor cells must detach from the ECM and maintain their viability in the circulatory system. Most circulating tumor cells (CTCs) will die as a result of losing adhesive junctions, so anoikis serves as a natural barrier for metastasis [3,7]. Since most CTCs are single cells, studying the survival and growth of metastatic cancer cells should be modeled using single cell assays [8]. Performing single-cell assays in cell-culture dishes is limited by low-throughput and poor reliability. Due to these issues, thousands of cells are used in conventional anoikis assays, which assess the cell viability in suspension culture dishes after a few days [9]. However, cell aggregation, which inevitably happens, can enhance the viability of cells in aggregates, resulting in a skew of survival rates. Although anti-aggregation additives (e.g. Heparin) can be used to mitigate aggregation, the anoikis behavior can be significantly affected [10]. Another issue in bulk anoikis assays is reliable media exchange. Cells can be easily lost when replacing the waste media by pipetting; as a result, the duration of the assay can be limited.

Due to genomic instability of cancer cells [11,12], certain cells may have a higher metastatic potential. For example, tumor-initiating cells (TICs), which are a small portion of the whole tumor [13-15], are hypothesized to serve as metastatic seeds and be responsible for tumor re-growth following chemotherapy and radiation [16]. However, their behavior can be averaged out by bulk tumor cells in conventional assays [17-19]. To understand the behavior of each cell in a heterogeneous group, we should be able to provide single cell resolution at high throughput, enlightening individual properties of each cell rather than the average behavior of the bulk tumor.

There are a number of previous works reporting microfluidic platforms for performing sphere assays on-chip, including hanging droplet methods [20-22] and micro-rotation flow [23]. These platforms accomplished suspension culture resulting in mostly cell aggregation rather than single cells. The droplet-based system can isolate single cells in suspension; however, it is difficult to continuously provide fresh media to each droplet, so the nutrients in the isolated droplet are depleted over time [24]. Recently, we demonstrated successful suspension cell culture in our single cell platform by integrating topographically-patterned polydimethlysiloxane (PDMS) layers to provide a super-hydrophobic surface for facilitating suspension cell culture without aid of any chemical coatings [25]. Despite its advantages over many conventional suspension culture coatings, the patterned surface requires the deep reactive ion etching of silicon in fabrication and makes optical imaging complicated.

In this work, we report a single cell suspension culture chip, which can provide high-throughput of 1,024 assays in a trial, single cell resolution (locating exactly one cell into each chamber) and continuous media perfusion to avoid the difficulty in exchanging media. To the best of our knowledge, this is the first trial of integrating polyHEMA in a single cell platform for single cell anoikis assays.

3.2 Single cell capture scheme

For the presented single cell anoikis assay chip, we adopted our previous single cell hydrodynamic capture scheme [26]. Fig. 3-1 (A) shows the fabricated device with 1,024 microchambers, which facilitates high throughput single cell assays. Cells are loaded from the inlet to the array of microchambers. The flow is generated spontaneously by the liquid height difference between the inlet and the outlet, so no external pump is required. In each microchamber, there are two fluidic paths: the central path and serpentine path (Fig. 3-1 (B)). The central path has lower flow resistance, so, the first cell entering the chamber tends to flow through the central path (Fig. 3-2). As the opening of the central path is smaller than the cell size (10 µm by 15 µm) and sterically captures the cell, the captured cell will block the central path and act as a valve, increasing the central path resistance. The following cells will thus preferentially flow through the serpentine path and be captured in the downstream microchambers (Fig. 3-2 (F)).

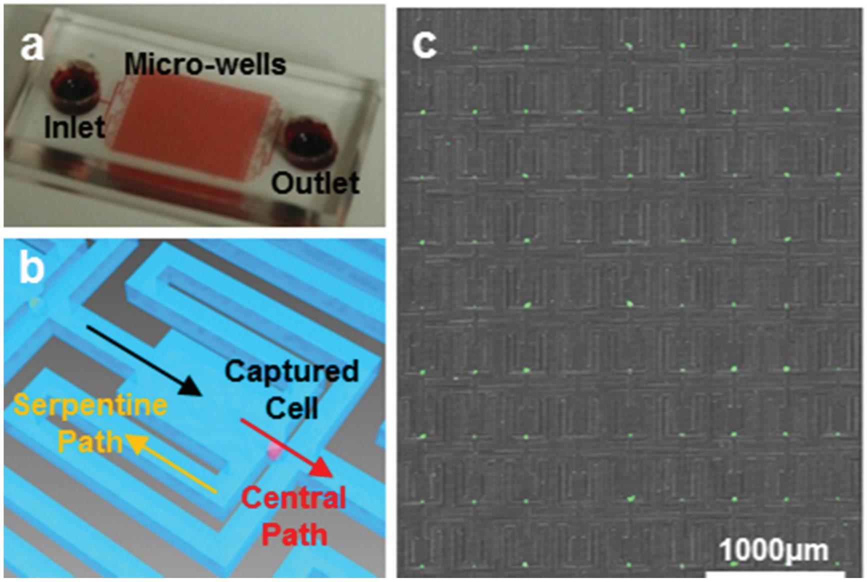

Fig. 3-1. Microfluidic chip for single cell suspension culture. (A) Photograph of the fabricated 1,024-microchamber device, in which the media containing cells flows from the inlet to the outlet. (B) Enlarged schematic of a cell capture chamber with a central path and serpentine path. (C) Fluorescent micrograph of captured SUM159 cells in the fabricated chip, showing a 9 by 9 segment. Cells were stained with CellTracker Green. Scale-1000µm.

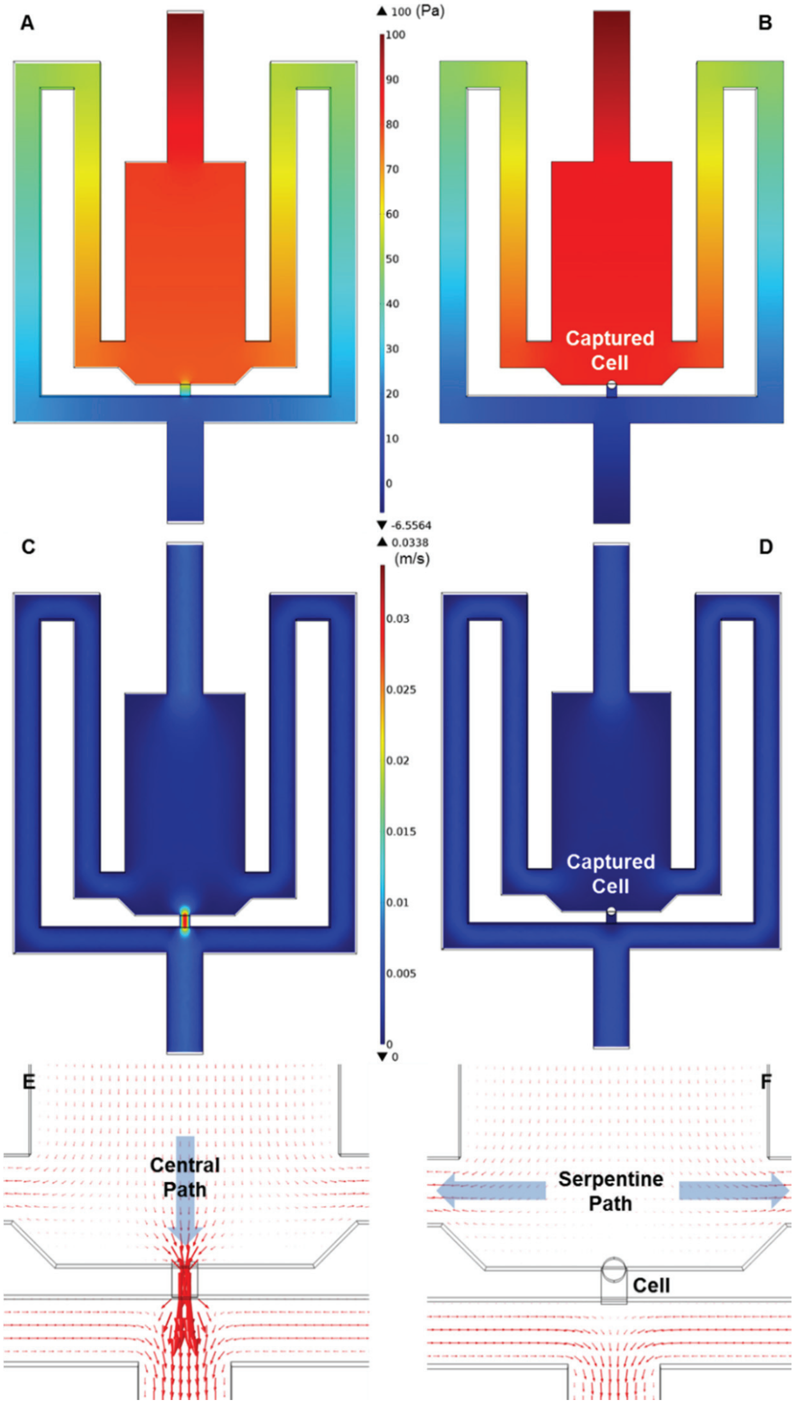

Fig. 3-2. Simulations of flow velocity and pressure on the cell capture scheme by COMSOL 4.3: (A, B) Simulations of pressure distribution before and after cell capture. (C, D) Simulations of flow velocity before and after cell capture. (E) The simulated flow pattern before cell capture. The red arrows indicating flow direction and velocity suggest that the cells are likely to be guided to the capture site and get captured. (F) After cell capture, the capture cell blocks the flow through capture gap, so the next cell will be guided to the serpentine path.

Extensive experiments have been performed by five cell types; high cell capture rates of > 70% have been achieved in all of these cell lines. Fig. 3-1 (C) shows a 9 by 9 subset of the array of culture chambers, in which 70 SUM159 cells were captured for an 86.4% capture rate. The captured single cells can be easily distinguished by optical imaging, making this platform ideal for quantifying heterogeneous cell populations. Using this chip, we can capture, culture, and monitor nearly 700-800 single cells in a single experiment, so the presented system outperforms previous miniaturized anoikis platforms in throughput and capture rate by an order of magnitude [27, 28].

3.2 Characterization of PolyHEMA coated substrate

To achieve suspension culture in our single cell platform, we used poly(2-hydroxyethyl methacrylate) (polyHEMA) as a non-adherent coating material [29]. After absorbing water, polyHEMA forms many hanging long-chains that block cell adhesion on the substrate. Although polyHEMA has been used for suspension culture for more than 30 years, it has not yet been integrated with microfluidic technology. Conventional coating techniques are very simple: polyHEMA is first dissolved in ethanol, and then the solution is added to a cell-culture dish. After natural evaporation of ethanol, polyHEMA will form a thin film on the dish [30]. However, due its surface roughness and non-uniformity, this process has two major challenges when integrated with microfluidics. First, large surface roughness, resulting from uncontrolled evaporation of ethanol, leads to poor bonding with the PDMS layer and inducing severe leakage (Fig. 3-3 (A)). Second, due to the non-uniformity of film thickness, we need to apply a thicker polyHEMA coating (~ 30 mm) to prevent pinholes or openings in the coating. As polyHEMA can absorb 50% water (w/w) and expand [31], the expanded polyHEMA hydrogel can block the fluidic channel thereby preventing ideal device operation.

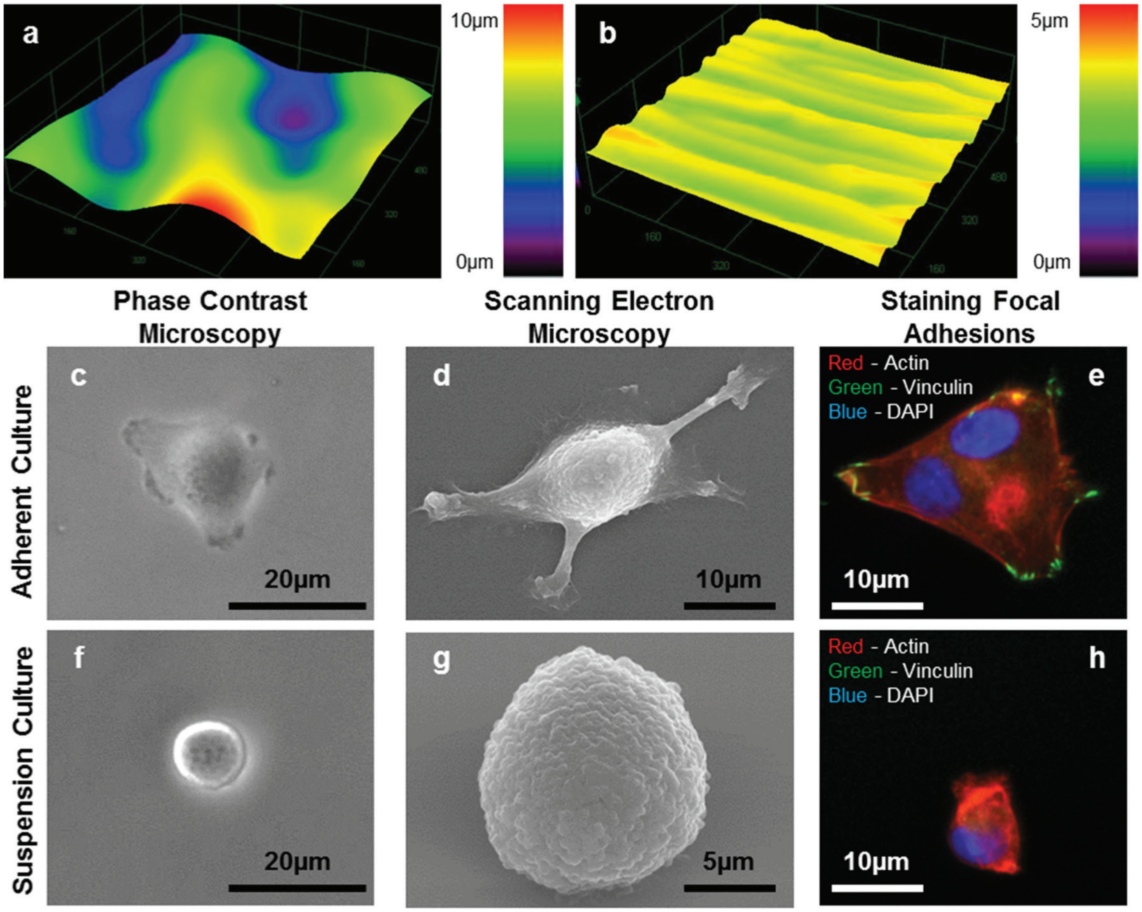

Fig. 3-3. Surface properties of polyHEMA films. 3D surface profile of polyHEMA coated substrate by (A) conventional evaporation process or (B) by spin coating and reflow process. MDA-MB-231 cells were cultured for 24 hours on (C-E) non-coated glass substrate or (F-H) polyHEMA coated substrate. Phase contrast micrographs (C, F) and scanning electron micrographs (D, G) of single MDA-MB-231 cells. (E, H) MDA-MB-231 cells were stained for actin (red), vinculin (green), and nucleus (DAPI blue).

The presented process is composed of two steps: spin coating and reflow. The spinning process removes any excess polyHEMA from the surface, and the thickness of polyHEMA layer can be precisely controlled by the spin speed. Although the rapid spinning speed may result in quicker evaporation of ethanol, leaving cavities on the surface and some trenches along the radial direction, these issues can be alleviated by reflowing the polyHEMA film at an elevated temperature after spin coating (Fig 3-3 (B)). As the glass transition temperature of polyHEMA is around 100°C, the polyHEMA film can reflow to fill the cavities and trenches at a temperature above 100°C and below 200°C, the burning temperature of polyHEMA (Fig 3-4). The surface roughness root mean square (RMS) of the conventional coating process is more than 3 μm, while that of the spin-coated films is less than 0.2 μm (Table 3-1). Compared to the conventional evaporation process, which generates high peaks and deep valleys, the thin and uniform polyHEMA films coated by the spin and reflow method can reliably bond with the PDMS layers for suspension cell culture.

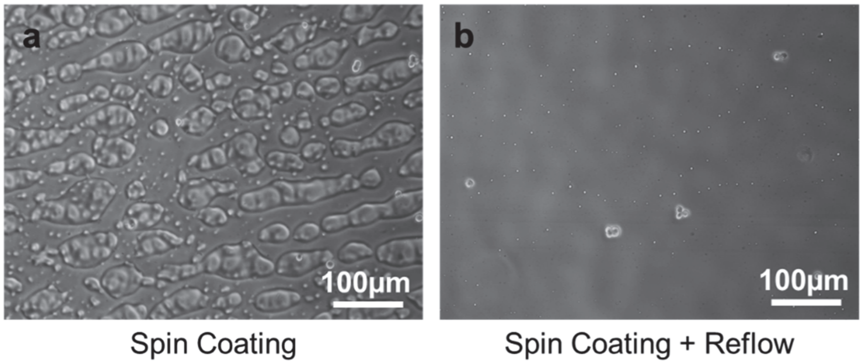

Fig. 3-4. PolyHEMA spin-coated surface with and without reflow process: (A) the polyHEMA spin-coated surface without reflow. As the ethanol evaporates fast during the spin-coating, the radial trenches are formed on the substrate. Also, some evaporation bubbles were trapped in the polyHEMA film, making the surface coarse. (B) After reflow at 200 °C overnight, the trench profile was flattened, and the trapped bubbles were released, making the coated surface smoother.

Table 3-1. The comparison between conventional and presented polyHEMA coating technology. *Data are shown as the mean ± SD (N = 5), *** $P < 10^{-3}$.*

	Conventional	**Spin & Reflow**
Thickness***	30.5±2.71 µm	2.04±0.26 µm
Roughness RMS***	3.15±0.50 µm	0.19±0.04 µm
Peak Height***	6.55±0.62 µm	0.56±0.07 µm
Valley Depth***	9.24±1.65 µm	0.65±0.14 µm

3.3 Suspension culture on polyHEMA coated substrate

After characterizing coating quality, suspension cell culture was performed on the coated substrate and compared to conventional culture. MDA-MB-231 breast cancer cells cultured for 24 hours on glass substrate without polyHEMA coating exhibit spreading morphology and focal adhesions indicating good cell adhesion (Fig 3-3 (C, D)). In contrast, MDA-MB-231 cells cultured on the polyHEMA-coated surface indicate no focal adhesions formed on the substrate and cells maintained a rounded morphology (Fig. 3-3 (F, G)). Focal adhesions serve as the link between internal cytoskeletal networks and ECM. Therefore, the absence of focal adhesions indicate whether a cell is truly cultured in a suspension environment[32]. MDA-MB-231 cells were plated on standard tissue culture plastic with and without polyHEMA coatings, and their focal adhesions were stained. Cells cultured on a normal tissue culture plastic expressed distinct vinculin focal adhesion clusters (Fig. 3-3 (E)), while cells cultured on polyHEMA did not form focal adhesions (Fig. 3-3 (H)). No adherent cells or cells with distinct extracellular vinculin clusters were observed in the polyHEMA-coated dishes, confirming a robust non-adherent environment by the polyHEMA coating.

3.4 Single cell anoikis assay

While conventional dish-based anoikis assays load many cells and suffer from uncontrolled cell aggregation, our approach provides precisely one cell in a chamber (Fig. 3-5 (A)). We quantified the ability of single C2C12 normal myoblast and SUM159 breast cancer cells to survive in adherent or suspension conditions in the microfluidic chip. For the normal myoblast cells, adhesion to the substrate is critical for maintaining viability; as a result, only 4% of the captured cells survived after six-day culture in suspension (Fig. 3-5 (B)). However, 50% of SUM159 cells, which is a highly aggressive cancer cell line, can survive in suspension. Significant difference in vaibility was observed on day 2, day 4 and day 6.

Within tumor cells, TICs are an emerging target for cancer therapy due to their resistance to conventional drug therapies and potential to initiate relapse of cancer [13, 17, 33]. Aldehyde dehydrogenase (ALDH) activity is a well-known marker of these cells, which are identified using the ALDEFLUOR assay [33, 34]. High ALDH expression in tumors correlates with poor patient prognosis [35]. ALDH+ SKOV3 cells are highly enriched for tumor-initiation and resistance to chemotherapy [34]. To test if ALDH+ cells are more resistant to anoikis, we loaded SKOV3 cells into polyHEMA-coated microfluidic chips, and used the ALDEFLUOR assay to identify the ALDH+ cells right after cell loading. Following six days of suspension culture, cell viability was assessed by LIVE/DEAD staining. 31.2% of the ALDH+ population survived, while the survival rate of ALDH- SKOV3 cells was only 9.3% (Fig. 3-5 (C)). This result confirms that ALDH+ cancer cells exhibit stronger resistance to anoikis.

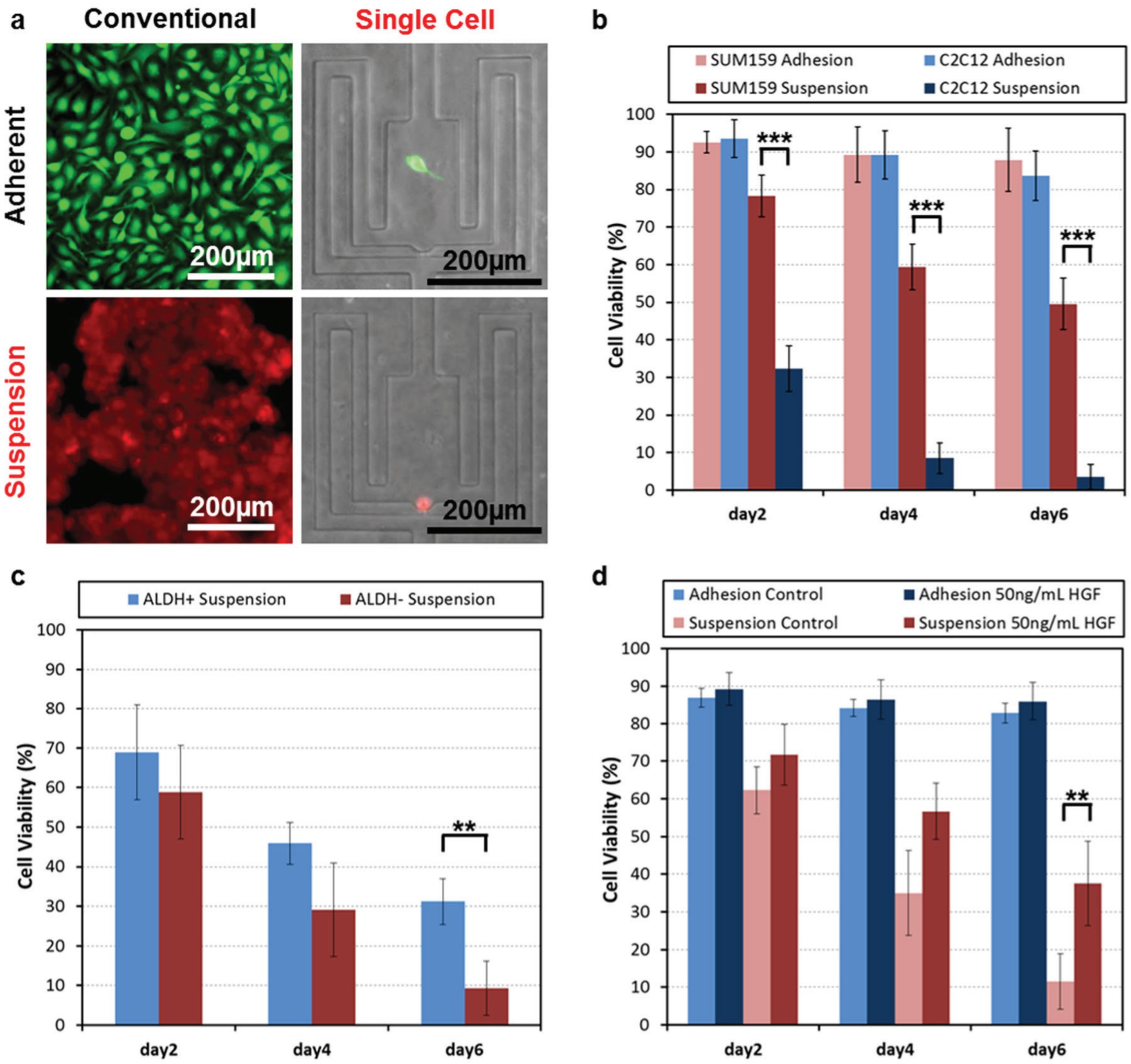

*Fig. 3-5. Single cell anoikis assay. (A) SKOV3 cells were plated in conventional dishes (left) or fabricated microfluidic chips (right) that were uncoated (top) or polyHEMA coated (bottom). Cells were loaded at 1000 cells/cm^2 (left) or at single cell level (right). Cell viability (green=live, red=dead) was measured 48 hours later. (B) SUM159 and C2C12 cells were loaded into uncoated (adherent) or polyHEMA (suspension) microfluidic chips and cell viability measured 2, 4 or 6 days later. Data are shown as the mean ± SD (N = 4), *** $P < 10^{-3}$. (C) SKOV3 cells were loaded into polyHEMA coated microfluidic chips and stained with the ALDEFLUOR assay to identify ALDH+ and ALDH- cells. Cell viability was assessed using the LIVE/DEAD kit at the indicated time points. Data are shown as the mean ± SD (N = 6), ** $P < 10^{-2}$. (D) SKOV3 cells were loaded into uncoated and polyHEMA coated microfluidic chips in the absence or presence of 50 ng/mL HGF. Cell viability was assessed using the LIVE/DEAD kit at the indicate time points. Data are shown as the mean ± SD (N = 9), ** $P < 10^{-2}$.*

Anoikis can be regulated through a variety of intrinsic and microenvironment factors that play a key role in determining the outcome of metastasis [2]. Hepatocyte growth factor (HGF) has been shown to trigger greater resistance to anoikis in cancer cells [36, 37], and SKOV3 cells were tested since most cells die in suspension by day 6. In media without HGF, only 11% of SKOV3 cells survived for 6 days, while the viability increased to 37% when treated with 50 ng/mL HGF (Fig. 3-5 (D)). This experiment confirmed that HGF can enhance the resistance of single cells to anoikis and demonstrated the feasibility of our platform in screening for regulators of anoikis.

3.5 Sphere formation from single cells

Although some metastatic cancer cells can survive in the circulatory system by avoiding anoikis and seed secondary organs, the majority of cancer cells remain dormant and do not proliferate [2]. Two possible reasons that can explain this phenomenon include: 1) the survival and proliferation of metastatic cancer cells depends on signals from the microenvironment [2], or 2) that only TICs are able grow into a secondary tumor [18, 19]. Sphere formation has been suggested as a surrogate assay for stem/progenitor cell activity [38, 39]. We assessed the ability of the suspension microfluidic chips to support sphere formation by culturing cancer cells in serum-free media supplemented with EGF, FGF, B27 and other reagents. For SUM159 cells, 55% of single SUM159 cells can grow to a sphere with a size larger than 50μm diameter in 10 days (Fig 3-6 (A-F)). In contrast to SUM159 cells, MDA-MB-231 cells have a low proliferation rate in suspension, forming small and loosely connected aggregates (Fig. 3-6 (G)). Compared to SUM159 and MDA-MB-231, MCF-7 breast cancer (Fig. 3-6 (H)) and C6 glioma cells have moderate-sphere-forming potential (Fig. 3-6 (I)). Around 3% of the captured MCF-7 and C6 can form spheres. In addition to the sphere formation rate (Fig. 3-6 (I)), the size of each sphere can be continuously monitored over 10 days (Fig. 3-6 (J)). These experiments demonstrate the capacity to perform high-throughput sphere formation assays where hundreds of spheres can form in a single assay.

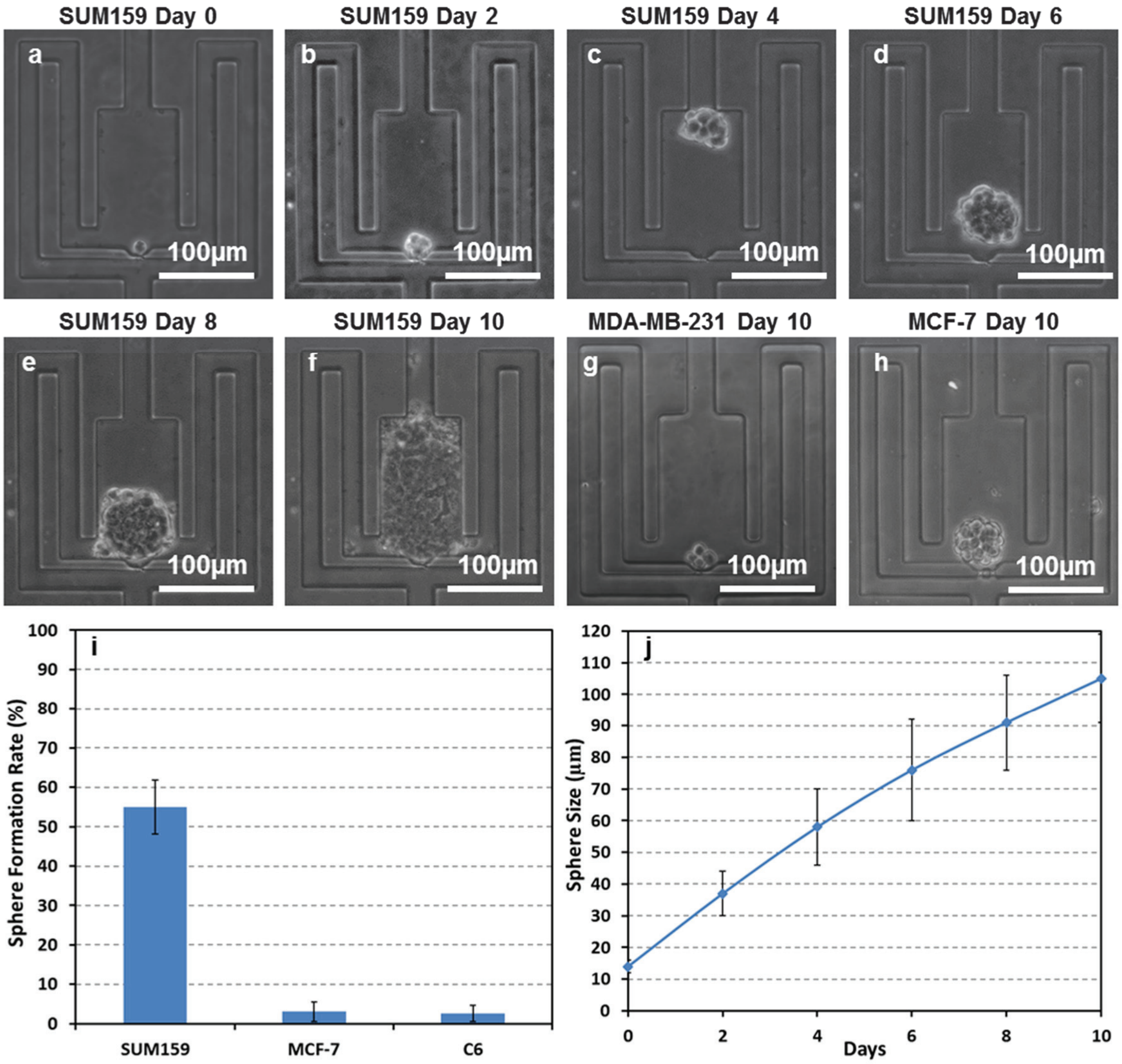

Fig. 3-6. Formation and morphology of cancer spheres derived from a single cell: (a-f) The development of a SUM159 sphere from a single cell in the polyHEMA-coated suspension culture micro-chamber: (A) day 0, (B) day 2, (C) day 4, (D) day 6, (E) day 8, and (F) day 10. (G) The development of sphere formation from single MDA-MB-231 cell after ten days. (H) The development of sphere formation from single MCF-7 cell after ten days. (I) The sphere formation rates of SUM159, MCF-7 and C6 cells for spheres with a diameter larger than 50 μm. (J) The sphere size change of SUM159 over time by the diameter of spheres from day 0 to day 10.

3.6 Sphere formation rate of stem-like Notch+ and non-stem-like Notch- cells

As the presented tool can monitor sphere formation of individual cells over time, we investigated the cellular heterogeneity in T47D breast cancer cells. The Notch pathway is a signaling pathway that regulates cell self-renewal and differentiation, and high Notch expression is related to stem-like properties and higher tumor initiating potential [40, 41]. To monitor Notch pathway activation, we transduced T47D cells with a lentiviral (pGreenFire1) Notch reporter containing multiple Notch response elements upstream of a minimal CMV promoter regulating destabilized GFP. Due to asymmetric division, some Notch+ cells generate Notch- daughter cells, so the cell culture becomes a mixture of Notch+ and Notch- populations. To measure sphere formation from Notch+ and Notch- T47D cells, we loaded unsorted cells into suspension microfluidic chips and cultured in serum-free media. After culture for 14 days, both Notch+ and Notch- T47D cells formed spheres (Fig. 3-7 (A, B), but the sphere formation rate of Notch+ cells was significantly higher (Fig. 3-7 (C)). This result confirms that Notch+ cells have a higher stem/progenitor cell potential. In addition, the average diameter of Notch+ spheres was significantly larger than that of Notch- spheres (Fig. 3-7 (D)), indicating a higher proliferation rate of the Notch+ cells. The sphere formation data from T47D cells is consistent with the previous rate reported from the conventional sphere assays [41]. This experiment validates our capability to study the sphere-forming potential of different subpopulations within a heterogeneous cell population.

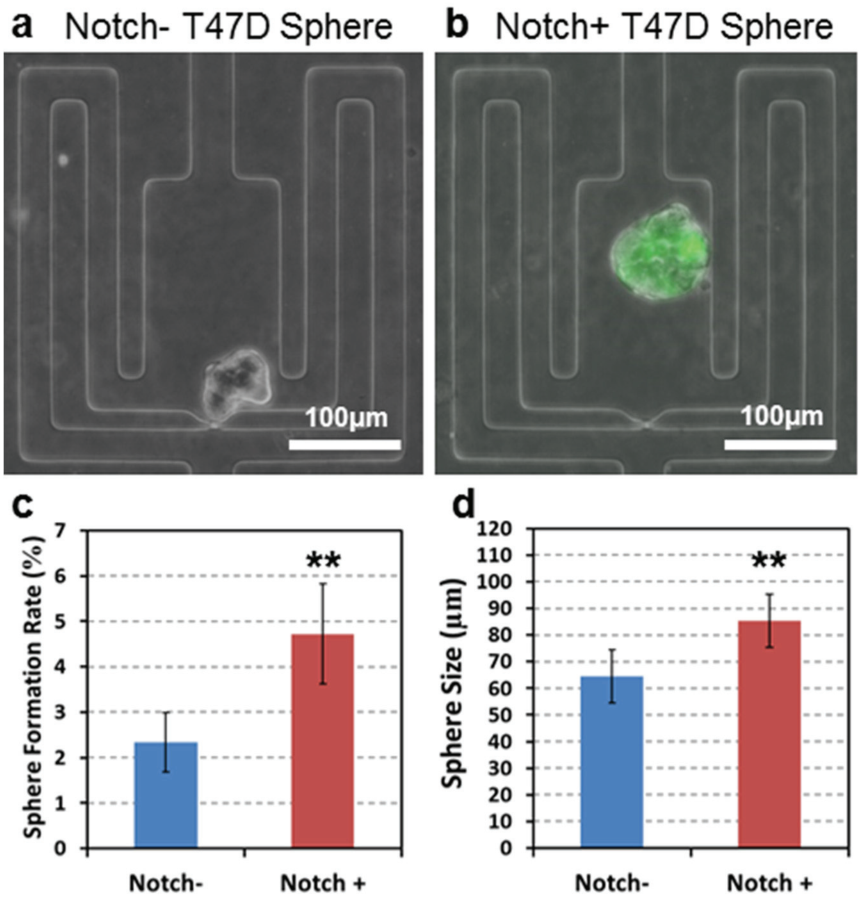

*Fig. 3-7. Differential cancer sphere formation from Notch+ and Notch- T47D cells. Representative cancer sphere derived from a single (A) T47D Notch- (GFP-) or (B) T47D Notch+ (GFP+) cell in the polyHEMA coated suspension culture micro-chamber. (C) Sphere formation rate of Notch+ and Notch- cells after 14-day culture. Data are shown as the mean ± SD (N = 4), ** $P < 10^{-2}$. (D) Average sphere size of Notch+ and Notch- cells after 14-day culture. Data are shown as the mean ± SD (N = 4), ** $P < 10^{-2}$.*

3.7 Chapter Summary

We present a microfluidic system for high-throughput single-cell suspension culture using a hydrodynamic capture scheme and optimized polyHEMA coating technique. In the cell capture experiments, the flow in the microfluidic chamber is consistent with computer simulation, and thus single cells were captured reproducibly in the array of 1,024 chambers by simple gravity flow without any external component. Among 5 different mammalian cell types, high and reliable capture rates from 71% - 84% were attained; the weak sensitivity to the cell type makes the platform a generic single-cell assay tool. Using the platform, the cells are individually separated into each chamber; this will not only prevent uncontrolled cell aggregation but also enable tracking of individual cell behaviors within heterogeneous populations.

Although polyHEMA has been used for suspension cell culture, the conventional coating technique provides poor uniformity due to its uncontrolled evaporation process. The spin-coating, which can achieve a controlled evaporation process and remove excessive polyHEMA solution, is widely used in microfabrication, so we introduced it in the polyHEMA coating technique. Even though pinholes and trapped bubbles are generated during spin-coating, these defects can be removed by double spin-coating and high temperature reflow. With the optimized coating protocol, the surface roughness can be reduced to 0.2 μm, which is only 6% of the conventional coating process, so the uniform coated substrate can be successfully integrated in microfluidics.

The features of single-cell, high-throughput, and reliability distinguish the presented approach from previous dish-based and microfluidic methods for suspension culture. This is particularly important in the study of cancer metastasis. Due to cancer cell heterogeneity, each cell has its own unique property, and thus behaves differently in metastasis. Still, most assays measure the average cancer invasion behavior over large number of cells with an underlining assumption that all cells are identical, which can lead to incorrect, imprecise results. The presented platform facilitates monitoring the behaviors of 1,024 heterogeneous single cells simultaneously, so the distribution of individual cell behaviors can be analyzed in one assay. As such, we demonstrated different anoikic behaviors between stem-like and non-stem-like SKOV3 ovarian cancer cells.

Finally, for single-cell-derived sphere formation assays, which typically take two weeks or longer, the reliable media exchange is an important issue, because cells in suspension can be easily lost when replacing the waste media by pipetting. In contrast, the presented platform provides a continuous perfusion of media from gravity flow for long-term culture. Thus, the presented technology greatly improves the reliability and throughput of the assays. With orders of magnitude higher throughput, we successfully performed the single-cell-derived sphere assays of SUM159, MDA-MB-231, C6, and MCF-7 cells. In addition, we examined the difference between stem and progenitor cell potential of Notch+ and Notch- breast cancer cells.

Chapter 4
CELL PAIRING RATIO CONTROLLED MICRO-ENVIRONMENT WITH VALVE-LESS ELECTROLYTIC ISOLATION

This chapter covers the ratio controlled cell-cell interaction chip, which can precisely control the number of interacting cell types to accurately model cancer cell niches and provide spatio-temporal control of microenvironments for cell-cell interaction. To isolate chambers without using any valves or external pneumatic pumps, we introduced a novel actuation method by generating electrolytic bubbles to block the flow.

4.1 Introduction

The cancer cell niche is a complex microenvironment, consisting of cancer cells, endothelial cells (EC), macrophages and mesenchymal stem cells (MSC); and tumor-stromal interaction is one of critical factors effecting the development of tumors [1-3]. It is believed that tumor cells can exploit nearby normal cells to enhance tumor growth, metastasis and drug resistance. Without establishing or accessing a proper micro-environment, the cancer cells may die or stay in senescence forever [4-5]. Recent papers revealed the interaction feedback loops between breast cancer and mesenchymal stem cells [6]. For example, SUM159 (breast cancer) cells form a positive feedback interaction with mesenchymal stem cells via IL-6 and CXCL7 cytokines. As a result, the existence of mesenchymal stem cells in the cancer niche can accelerate tumor development. It has been also reported that immune cells play a critical role in cancer metastasis by triggering inflammatory response in the tumor micro-environment [7-8]. Tumor associated macrophages (TAM) can enhance angiogenesis, and thus metastasis, by secreting a wide range of growth factors and cytokines. Endothelial cells also contribute to the invasion and metastasis of cancer by promoting cancer stem cell phenotypes and enhancing cancer metastasis [9-10]. Compared to the late stage tumor cells, these tumor associated cells are less drug resistant; thus killing these tumor associated normal cells can be used to deter the cancer development [11]. Inhibiting the interaction between tumor cells and tumor associated normal cells can be an alternative therapy. As a result understanding cancer-niche interactions is of great importance for developing cancer therapeutics.

Conventionally, cell interactions can be studied by co-culturing two cell types in the same petri dish [12]. However, dish-based co-culture methods are limited in several key aspects. Metastatic cancer cells are typically transported as a single CTC, and tumorigenesis from a single cell is quite different from co-culturing many cells [13]. As cancer metastases account for more than 90% of cancer-related mortality, modelling the tumorigenesis process in an appropriate microenvironment from a single cell is essential for metastasis study [3,14-15]. As the cell behaviour can be affected by neighbouring cells, the conventional dish culture cannot ideally model the tumorigenesis process [16]. Another limitation of conventional co-culture assays is its poor spatial control. In conventional interaction experiments, two cell populations are simply mixed in a dish, so the spatial distribution of two cell types can vary from one place to another. Some cells may be surrounded by a large number of different types of cells, while others may form aggregation of the same type of cells. Hence, the precise ratio controlled co-culture cannot be achieved by the conventional dish co-culture. Also, dish-based methods lack the ability of using small samples (< 1000 cells), while CTCs and primary samples are more often available in a small sample. Finally, dish-based studies cannot track individual behaviors of heterogeneous cancer populations. They can only characterize the average behavior of entire cell population. This is an issue as some sub-populations in tumor have a different interaction pathway. For example, it is believed that only the aldehyde dehydrogenase positive (ALDH+) cells have strong interaction with MSC [6].

There are a number of previous works reporting on microfluidic platforms for cell-to-cell interaction studies [17-28]. Most of them still require loading hundreds or thousands of cells in a device; thus, they suffer from the same issues as in the conventional dish-based co-culture [17-23]. Droplet based technology can provide a high-throughput combinatorial pairing of cells, but it lacks the capability of long-term cell culture, limiting its applications in practical co-culture assays [24] Recently, three microfluidic devices reported the cell pairing and cell-to-cell interaction at single-cell resolution [25-28]. However, they can only achieve the pairing of two different cells at 1:1 ratio due to geometric restrictions in the device structures. Actually, the cell ratios in tissue can matter in differentiation and it is important to screen assays for many different cell ratios to emulate in-vivo niches [29]. In this work, we present a reliable microsystem capable of performing cell interaction assays with a specific ratio between the two different cell types. By applying a hydrodynamic cell capture scheme in two different fluidic streams, we can precisely control the number of captured cells in each type. The captured cells interact through a bridge channel by diffusion of secreted cytokines. Although juxtacrine (contact-dependent) signalling also plays a role in cell-cell interaction, we focus on the secretion based interaction, which has been proved to be important in the interaction between cancer cells and MSCs [6].

A major innovation of the proposed microfluidic platform is the electrolytic valving, which generates bubbles to isolate paired cells in a chamber. In previous cell isolation works, pneumatically actuated valves formed from thin PDMS membrane deformation were used [22, 26]. Although pneumatic actuation has been widely used for control in many microfluidic systems, such microfluidic devices need to be continually connected to the pump during the entire isolation process; otherwise, the pressure, and thus the cell isolation, will be released. This weakness limits the applications and usability of pneumatic valving, especially in mammalian cell culture, which may require specialized culture conditions and long term incubation. The electrolytic valving, on the other hand, can maintain the bubbles generated through electrolysis for isolation without continued external connection. In addition, the pneumatic valving is sensitive to channel geometry [30, 31]. Channel height and width need to be carefully designed and made rounded to guarantee completely sealing. As the electrolytic bubble can fill almost any shape to isolate the chambers, there are fewer design constraints in the use of electrolytic valving. Moreover, the electrolytic actuation circuit can be implemented compactly using ICs, while the programmable pneumatic control cannot be easily miniaturized. Thus, electrolytic actuation has a higher potential for miniaturization and extension to high-throughput as a standalone micro-system, especially for the applications that need long-term and continual isolation control. In this work, we developed an electrolytic bubble generation and removal scheme, which can be used to control cell-to-cell interaction times to within a precision of one minute.

For the proof of feasibility, we demonstrated the interaction between PC3 (prostate cancer) cells and C2C12 (myoblast) cells by secreted growth factors [32, 33]. We confirmed that the growth of C2C12 could be boosted by the secretion factors from PC3 cells, and the proliferation rate of C2C12 be affected by the number of PC3 cells inside the same co-culture chamber.

4.2 Microfluidic Device Operation

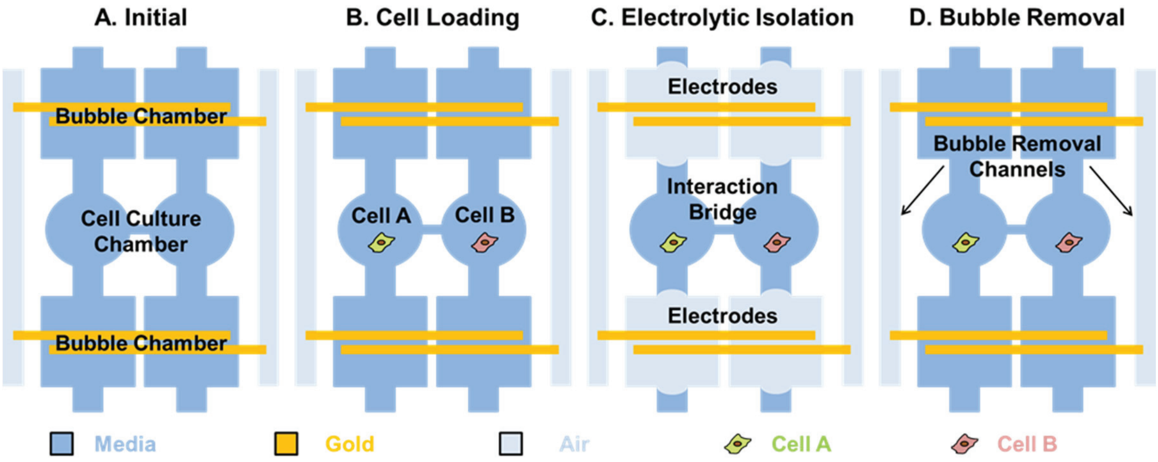

Fig. 4-1. Proposed microfluidic chip for paired cell to cell interaction. (A) The cell culture chamber is surrounded by two bubble chambers both in the upstream and downstream. (B) Two different cells are loaded in the cell culture chambers respectively. (C) After cells attached on the substrate, the voltage is applied to the gold electrodes, and thus the bubble generated by electrolysis seals the cell culture chamber. As the cytokines secreted by cells can diffuse through the interaction bridge, the cells in two cell culture chamber can interaction with each other. (D) Since the PDMS is gas permeable, the bubble can be removed by applying negative pressure to the bubble removal channel. Thus, the time of cell isolation can be precisely controlled.

The presented platform composes of cell culture chambers, interaction bridges for cell-cell interaction, and bubble chambers with gold electrodes on the substrate (Fig. 4-1(A)). Two key features of the proposed system are the ability to control the number of cells and cell-to-cell interaction time. To address the first task, the cells were loaded from two separate inlets. The number of loaded cells in a chamber can be determined by the number of capture sites in each chamber. To regulate the cell-cell interaction time, we used an electrolystically generated bubble for valve-less isolation of chambers. Each cell culture chamber is sandwiched by two bubble chambers in the upstream and downstream, respectively. When a sufficient potential for electrolysis is applied to the electrodes, a bubble can be generated, sealing the fluidic path. Then, the isolated cells in the chambers can interact through the interaction bridge by diffusion of secreted factors.

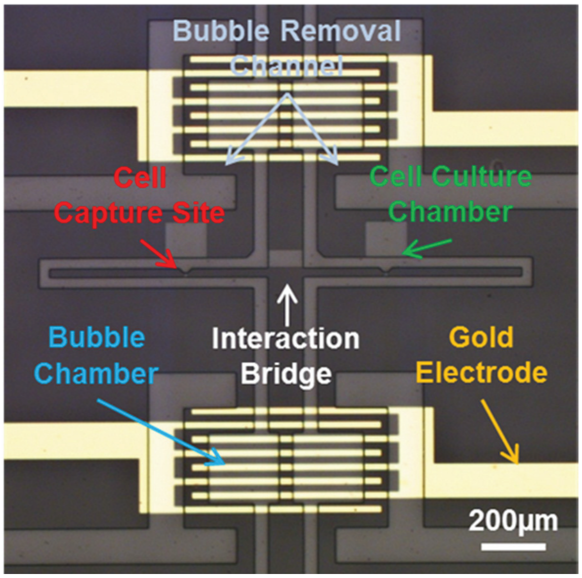

Fig. 4-2. Enlarged microphotograph of a fabricated device. The light color region is the microfluidic layer which culture chambers, bubble chambers, gold electrodes and the bubble removal channels. The cell culture chamber is surrounded by two bubble chambers. The golden part shows the comb shape gold electrodes for electrolysis.

Fig. 4-1 illustrates the operation of the presented microfluidic platform for paired cell-to-cell interaction. In the cell loading phase (Fig. 4-1 (B)), cell A is loaded from the left inlet and captured in the left chamber, and cell B is loaded and captured in the right chamber. Since the pressure is balanced between the two fluidic streams, cell loading can be carried out without interference between the two laminar fluids. The number of captured cells (for both type A and type B cells) can be determined by the number of cell capture sites in each chamber. After 4-6 hours, the captured cells will adhere to the substrate and remain viable and then proliferate within the microfluidic chambers.

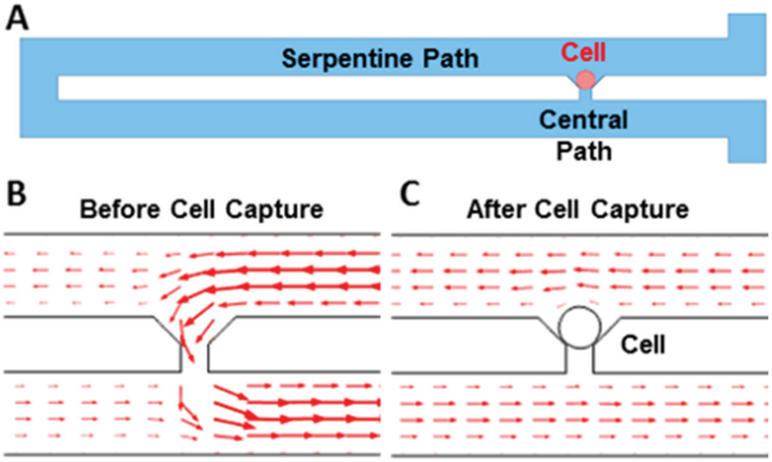

Fig. 4-3. Mechanism of Cell capture scheme: (A) The schematics of the cell valving capture (B) The simulated flow pattern before cell capture. The red arrows indicating flow direction and velocity suggest that the cells are likely to be guided to the capture site and get captured, and (C) After cell capture, the capture cell blocks the flow through capture gap, so the next cell will be guided to the serpentine path.

In the electrolytic isolation phase (Fig. 4-1 (C)), voltage is applied to the gold electrodes, and bubbles are generated by electrolysis to seal the cell culture chambers. The cytokines secreted by the cells can be accumulated and diffused through the interaction bridge, so the cells captured in two separate sides can communicate with each other by protein signals. The interaction bridge is narrow (10 μm in width and height) and long (100 μm), so that it will prevent cells from migrating into the other side. The bubbles generated in the bubble chamber are stable over more than three hours. If a longer cell-to-cell interaction time is required, the electrolysis electrodes can be activated again to generate additional bubbles to maintain the isolation. The interaction can be stopped at any time by removing the bubble (Fig. 4-1 (D)). When negative pressure is applied to the bubble removal channel, the bubble can diffuse out through the PDMS (50 µm thick) from the bubble chamber since PDMS is gas permeable. After the bubble is completely removed, media perfusion is resumed and the secreted proteins are washed away. Thus, the interaction stops.

4.3 Cell Capture Mechanism

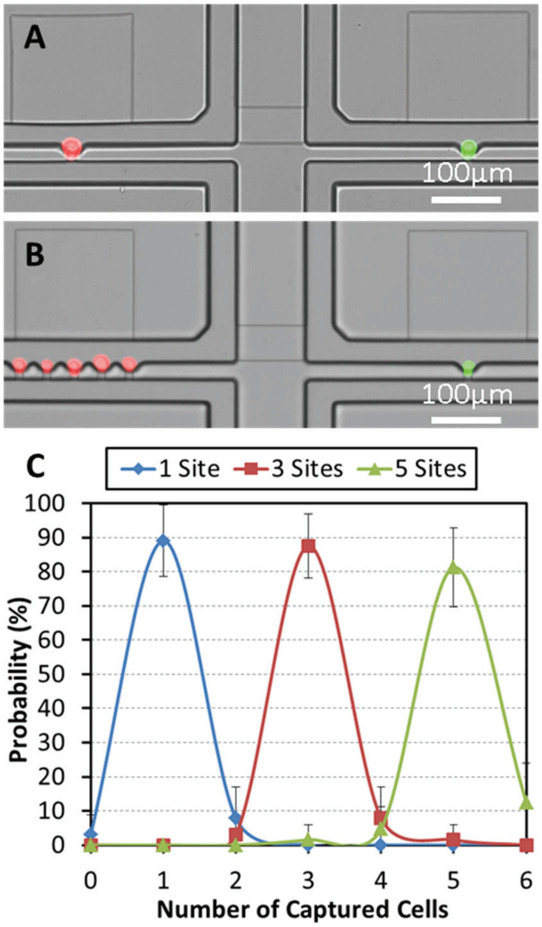

Fig. 4-4. Ratio controlled cell pairing: (A) One of each PC3 (red fluorescent labelled) and C2C12 (green fluorescent labelled) cells, (B) Five PC3 cells and one C2C12 cell, and (C) Capture rate for various different numbers in capture sites: one, three, and five, respectively.

In order to capture the specific number of cells in each culture chamber reliably and reproducibly, cellular valving mechanism has been adopted to deploy the cells hydrodynamically at each capture site (Fig. 4-3 (A)) [34-37]. To capture cells at each designated capture site, two paths are created in the design: a central path and a serpentine path. The hydraulic resistance of each path is inversely proportional to its flow rate. As a result, the long serpentine structure has a higher hydrodynamic resistance than the central path. Thus, the cells, following the major flow stream, are likely to be guided to the central path (Fig. 4-3 (B)). Since the opening of the central path is slightly smaller (Height: 10 μm, Width: 10 μm) than the size of PC3 (human prostate cancer) cells and C2C12 (mouse fibroblast) cells, the cells are sterically captured and plugs the gap, blocking the flow through the central path. Thus, the next cells will be guided through the serpentine path and captured in the downstream capture sites (Fig. 4-3 (C)). After optimizing the serpentine length, a capture rate of ~90% has been achieved for C2C12, PC3, and Skov3 (ovarian cancer) cells (Table 4-1)

Table 4-1. Optimized geometric parameters of capture sites for C2C12, PC3 and Skov3 cells and the corresponding capture rates.

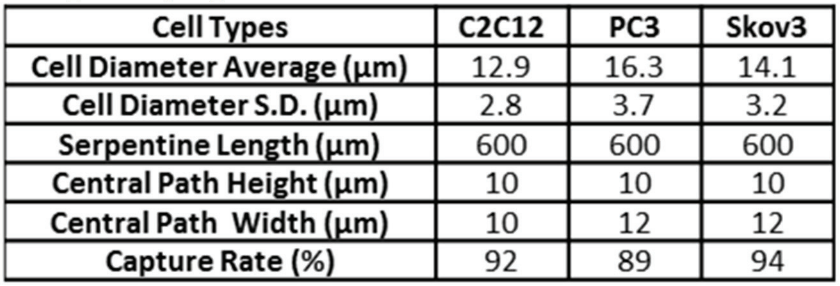

Cell Types	C2C12	PC3	Skov3
Cell Diameter Average (μm)	12.9	16.3	14.1
Cell Diameter S.D. (μm)	2.8	3.7	3.2
Serpentine Length (μm)	600	600	600
Central Path Height (μm)	10	10	10
Central Path Width (μm)	10	12	12
Capture Rate (%)	92	89	94

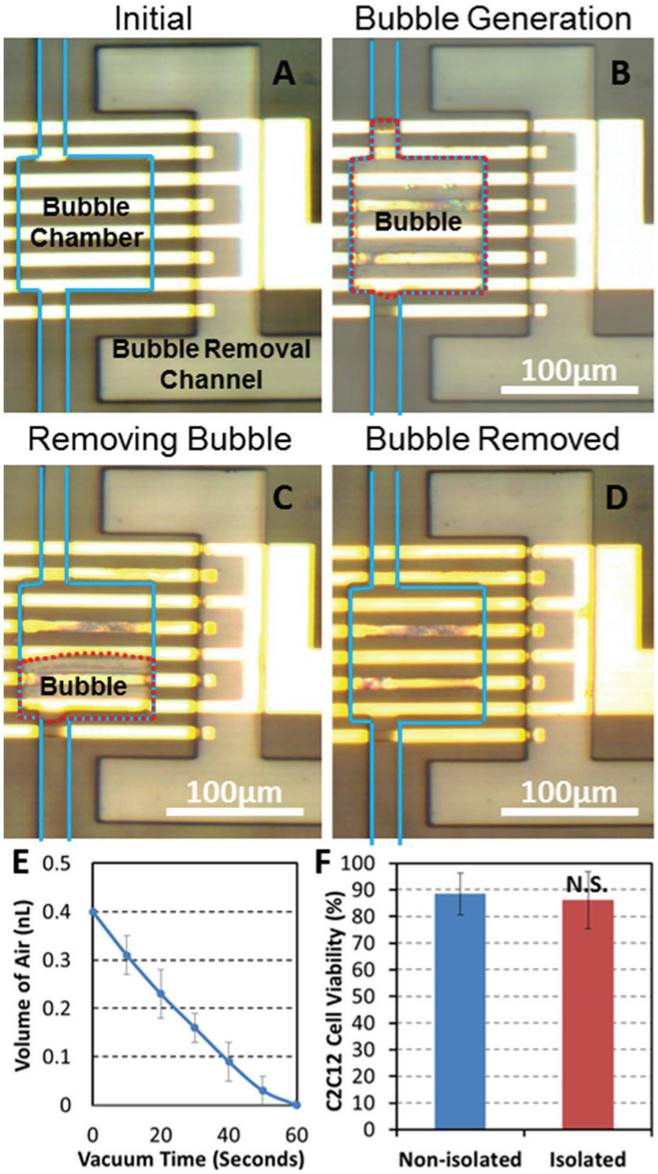

Fig. 4-5. Process of electrolytic bubble generation and removal. (A) Before electrolysis the bubble chamber was filled with cell culture media and the bubble removal channel was filled with air at atmospheric pressure. The blue line delineates microfluidic channels. (B) After 60 seconds of electrolysis, a bubble completely filled the bubble chamber and blocks the flow. The red dotted line is the outline of a bubble. (C) To remove the bubble, we applied negative pressure to the bubble removal channel. After 30 seconds, a bubble shrank in half. (D) After 60 seconds, the bubble was completely removed. (E) The volume of residual air in a bubble chamber as a function of time after applying negative pressure to the bubble removal channel. (F) The day 3 cell viability with and without the operation of electrolytic valve. No significant difference was observed, suggesting electrolysis has negligible effect on cell viability. (N = 4 devices)

By utilizing a high capture rate of single cells over 90% in each capture site, we can extend our design to capture multiple cells simply by adjusting the number of capture sites in each chamber. We can also deploy an arbitrary number (up to five) of two cell types in separate flow streams and study the effect of cell ratio in cell-to-cell interaction during co-culture. Fig. 4-4 (A, B) shows the ratio-controlled cell capture: pairing one PC3 cell and one C2C12 cell (Fig. 4-4. (A)), and pairing five PC3 cells and one C2C12 (Fig. 4-4 (B)). We can vary the combination of pairing from 1:1 to up to 5:1 (or even higher). When the number of capture sites is equal to or smaller than five, more than 80% of the chambers are filled with the captured cells as shown in Fig. 4-4 (C).

4.4 Electrolytic Isolation

In continual media perfusion culture, secreted proteins will be washed away. Therefore, it is important for cell-to-cell interaction studies to control and sustain the isolation of cell culture chamber to accumulate the secreted proteins and cytokines inside the chamber. In this work, we achieve this by generating electrolytic air bubbles in the bubble chambers located between the adjacent cell culture chambers. Fig. 4-5 (A) shows a bubble chamber with gold electrodes and bubble removal channels. As the PDMS is gas permeable, small bubbles can easily diffuse out through the PDMS membrane within several minutes. To maintain stable channel isolation, we incorporate a large bubble chamber of 100 μm by 100 μm and 40 μm in height (shown with a blue outline in Fig. 4-5) to facilitate the creation of a larger isolation bubble, which can sustain for more than 3 hours. If longer isolation is required, electrolysis can be performed again after 3 hours to sustain the bubble. Comb finger-shaped electrodes (20 μm in width for each comb finger and 20 μm in spacing between fingers) can generate bubbles evenly inside the whole bubble chamber. Thus, the generated bubble can quickly and completely seal the whole chamber in a minute.

The electric field as well as heat generated during electrolysis can be harmful to cells. We have implemented several techniques to minimize these effects. First, we tried to minimize electrolytic voltage. Since the minimum potential required for water electrolysis is around 1.23 Volts, the applied voltage should be higher than this to overcome extra potential drops in the metal wires and media. However, the higher the voltage we use, the more heat we generate. We chose 3 V as an optimal voltage for on-chip electrolysis that can balance electrolytic efficiency and cell viability, based upon design parameters and preliminary experiments. With 3V as a peak operating voltage, we optimize the waveform. Compared to applying a DC voltage, a pulsed waveform can help dissipate the accumulated heat, and a large single bubble can be easily formed from multiple bubble generations from the comb finger-shaped electrodes. For these reasons, we chose to use a pulse wave (3 Volts, 0.1 Hz, 1 μs pulse) for electrolytic bubble generation. The average power is less than 1 nW, and the resulting temperature increase in the cell culture chamber should be less than 0.01℃ (from simulation). After electrolysis for 60 seconds, a bubble can occupy the whole bubble chamber, and the culture chamber can be completely sealed and isolated (Fig. 4-5 (B)). In addition, we located the bubble chamber 500 μm away from the cell culture chambers to minimize the effect of any excessive heat generation and E-fields.

As the electric field and heat generated by electrolysis can be harmful to the cells, we implemented several techniques to minimize the effect on cells. The E-field and heat can be minimized by using the proper voltage. Since the standard potential of the water electrolysis is around 1.23 Volts, the applied voltage should be higher than the threshold to overcome resistance of the metal wire and the media. However, the higher the voltage we use, the more heat we generate. Considering the resistance of gold electrodes and the media, 3 Volts was determined as a suitable voltage for on-chip electrolysis that balanced the electrolytic and viability parameters. Once peak operating voltage is determined, the waveform is the next key parameter that must be optimized. Compared to continuous application of a DC voltage, a pulsed waveform can help dissipate the accumulated heat, and the rest between pulses allow time for the multiple bubbles generated by different electrodes to merge to form a larger single bubble. For these reasons, we decided to use a pulse wave (3 Volts, 0.1 Hz, 1 μs pulse) for the electrolytic bubble generation. The average power is less than 1 nW, and the resulting temperature change in the cell culture chamber is simulated to be lower than 0.01℃. After electrolysis for around 60 seconds, a bubble occupied the whole bubble chamber, and the culture chamber was sealed completely (Figure 4-5 (B)). Also, to minimize the effect of E-field and excess heat, the bubble chamber is 500 μm away from the cells.

4.5 Bubble Removal

To precisely control the cell isolation time, the electrolytic bubble can be immediately removed at the end of interaction cycles. We achieve this by applying a negative pressure to the bubble removal channel. As the PDMS is gas permeable, the bubble can diffuse through the PDMS membrane [38-39]. We minimized the distance (50 μm) between the bubble chamber and the air removal channel to achieve rapid removal of bubbles in less than a minute. Fig. 4-5 (C, D) demonstrates the process of bubble removal. The red dotted line is the outline of the bubble, which occupied the whole bubble chamber after electrolysis. After applying negative pressure to the bubble removal channel for 30 seconds, the bubble roughly shrank by half (Fig. 4-5 (C)); and after another 30 seconds, the bubble completely disappeared (Fig. 4-5 (D)). Using a negative pressure of around 7 psi, the bubble removal rate was measured as 0.4 nL per minute (Fig. 4-5 (E)). The bubble removal rate matches well with the predication from other reports [38-39]. We confirmed full functionality of the total 14 bubble chambers after ten cycles of bubble generation and removal, demonstrating the reliability and robustness of electrolytic sealing.

4.6 Cell Interaction of PC3 and C2C12 cells

In the fabricated platform, cell-cell interaction is induced from diffusion of secreting proteins through a narrow channel (10 μm by 40 μm, 100 μm long). In order to verify whether this interaction bridge channel can provide adequate diffusion of secreted signaling proteins and cytokines for cell-to-cell communication, we simulated the diffusion of molecules similar to the secreted proteins (Fig. 4-6). The simulation results show that the two chambers reach almost steady state after 3 hours of isolation. The difference in protein concentrations between the two chambers connected by the interaction bridge channel is only 11% (Fig. 4-6 (E)), supporting that our platform can provide efficient diffusion flow for cell interaction in the given geometry of our design. In addition, the non-isolated chamber was simulated (Fig. 4-7). As the secreted proteins are washed away by continual flow, the protein concentration of the receiving side is only 3.3% of that in the isolated chamber (Fig. 4-7 (E)).

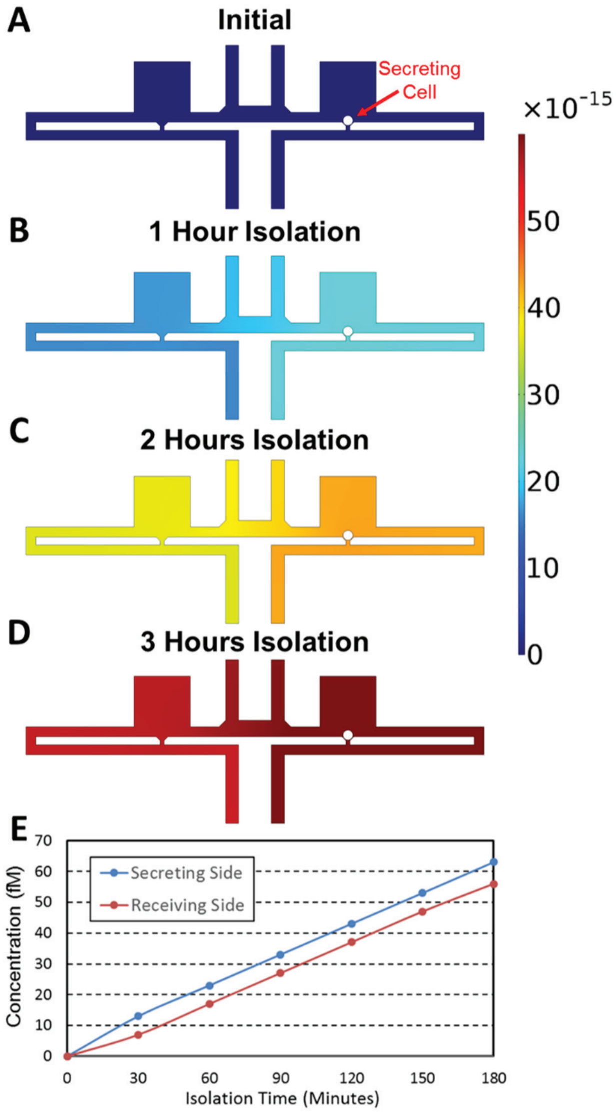

Fig. 4-6. Simulations of diffusion for signaling proteins through a narrow bridge channel by COMSOL 4.3. We assume that single cell secretes 1^{-20} mole of proteins per second and its diffusion coefficient is 1^{-10} m^2/s. We assume that the secreting cell is captured in the right chamber. We simulate the diffusion of signaling proteins from the right (secreting) chamber to the left (receiving) chamber for 3-hour isolation time. (A) Initial condition. Both chambers (left and right) have zero concentrations. (B) Concentration distribution after 1 hour isolation. (C) Concentration distribution after 2 hours isolation. (D) Concentration distribution after 3 hours isolation. (E) Concentration change of signaling proteins over time. Concentration of the receiving chamber (left) closely follows that of the secreting chamber (right). After 3 hour isolation, the concentration difference between two chamber is only 11%, confirming that the diffusion through a bridge channel is sufficient for adequate the cell-cell interaction.

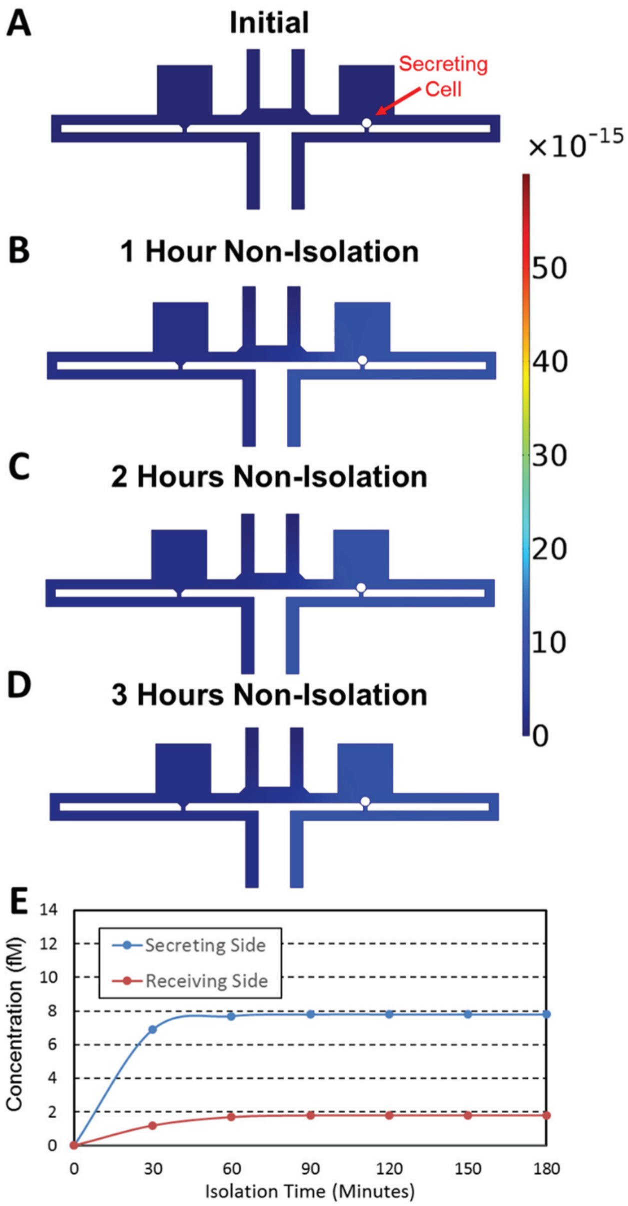

Fig. 4-7. Simulations of diffusion for signaling proteins when washed through perfusion flow by COMSOL 4.3. We assume that single cell secretes 1^{-20} mole of proteins per second and its diffusion coefficient is 1^{-10} m^2/s. As the chambers are not isolated, the secreted proteins are washed by perfusion flow of the media flowing from upstream to downstream. 50 Pa was assumed as a pressure difference between the upstream and downstream. Initially, the concentration is assumed zero and the secreting cell is captured in the right chamber. (A) Initial concentration distribution. (B) Concentration distribution after 1 hour. (C) Concentration distribution after 2 hours. (D) Concentration distribution after 3 hours. (E) Concentration change of signaling proteins over time. As the secreted proteins are washed away by perfusion flow, the protein concentration in the receiving chamber (left) is only 3.3% of that of the isolated case after 3 hours, confirming that cell-cell interaction is negligible.

4.7 Cytokine Diffusion through Bridge Channels

A novel microfluidic cell-to-cell interaction chip has been developed to control specific cell-pairing ratios for cell interaction assays. Electrolysis has been adapted to generate bubbles to block the media flow and isolate the culture chambers, so the captured cells can interact with each other by chemical secretions. Combining the fast electrolytic bubble generation and removal, the proposed platform can isolate paired cells for an arbitrary amount of time. The proposed electrolytic isolation scheme does not impose restrictions on the geometry of the capture design, so we can achieve a cell capture rate (for 1 to 5 cells) of more than 80% in all the fabricated chambers. The cell viability tests confirmed that the electrolysis and bubble removal operation will not affect the cell viability and proliferation rate. As a proof of the concept, we have demonstrated a cell interaction assay between C2C12 and PC3 cells utilizing different cell-pairing ratios on chip. This work not only demonstrates the capability of performing ratio controlled cell-to-cell interaction assays, but also shows the compatibility of electrolysis in microenvironment control for cell culture.

4.8 Cell-to-Cell Interaction Assays from Co-Culture of PC3 and C2C12 cells

Before carrying out biological assays in the fabricated devices, we evaluated the effect of electrolysis on cell viability. Since the air generated from electrolysis has more than 1,000 times the volume of the liquid (media), only a small fraction of the media (< 0.005%) in the chamber is consumed. Thus, the change in the media concentration is negligible. Also, the culture media is a buffered media; therefore, the pH of the solution is resistant to possible fluctuations that may be introduced by electrolysis.40 Three-day cell viability experiments of C2C12 cells were carried out to confirm that there was indeed no effect on cell conditions. After electrolytic sealing for three hours once a day for three days, 86 % of the captured single cells were still viable in the culture chamber. The cell viability was comparable to 89% viability observed in the control without electrolysis (Fig. 4-5 (F)). Fig. 4-8 (A) shows that the proliferation of C2C12 cells with electrolytic bubble sealing is similar to that of the control cells without electrolysis.

As a proof of concept, we demonstrated the interaction between PC3 cancer cells and C2C12 myoblast cells. PC3 are known to secrete a number of growth factors to enhance the growth of tumors [32]. In the previous work, it has been demonstrated that co-culture of PC3 cells and C2C12 cells can enhance the proliferation of C2C12 cells, but whether the ratio of two cell types can affect the interaction is not clear [26,33]. Using the fabricated prototype platforms, we loaded both PC3 cells and C2C12 cells in the same device with different ratios on Day 0. For simplicity, we compared only the two different ratios: "1:1" and "5:1" in this experiment. After cell loading, the bubbles were generated to seal the culture chamber for three hours once a day for three days.

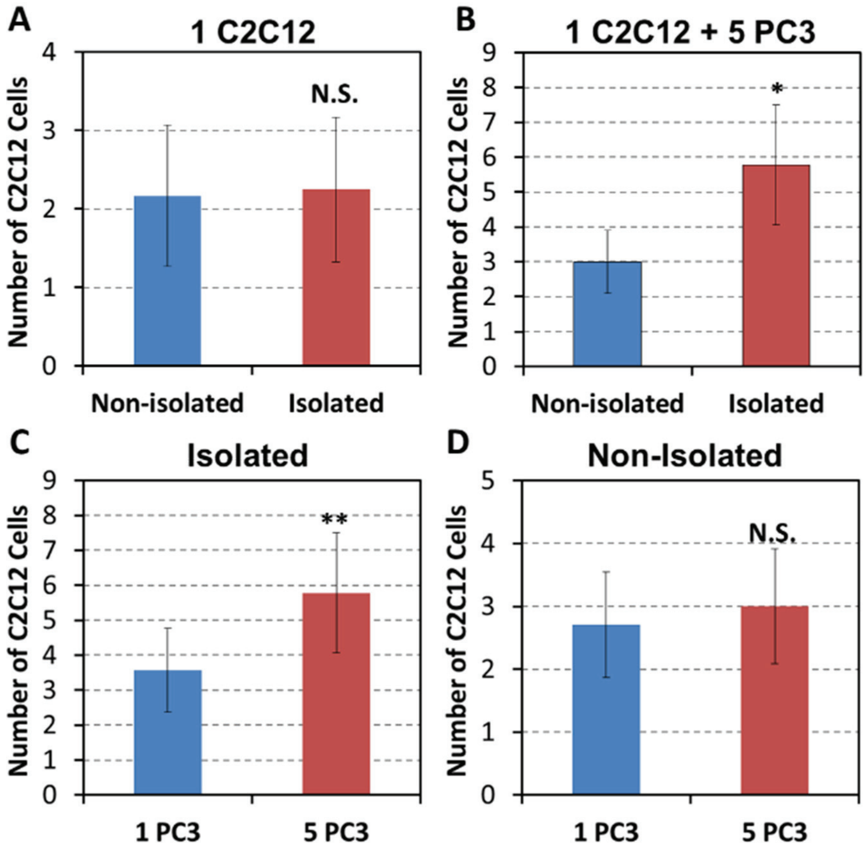

*Fig. 4-8. Cell proliferation of C2C12 cells with and without PC3 cells: (A) Proliferation rates of C2C12 cells with and without bubble isolation. The result confirms that the electrolytic isolation has negligible effect on proliferation. (B) C2C12 and PC3 cell-interaction assays with and without bubble isolation after 3 days. Co-culturing of one C2C12 cell and five PC3 cells significantly enhanced the proliferation of C2C12 cells when electrolytically isolating the culture chambers. Data points represent means ± standard deviations (N = 4 devices), * refers to $P < 0.05$. (C) With 3 hours of chamber isolation per day for three days, comparing the proliferation of C2C12 cells co-cultured with 1 PC3 and 5 PC3 cells, respectively, the latter showed a significantly higher proliferation rate, confirming that cell ratios are critical for cell interaction studies. Data points represent means ± standard deviations (N = 4 devices), ** refers to $P < 0.05$. (D) Without chamber isolation, no significant difference was observed in proliferation rates. Data points represent means ± standard deviations (N = 4 devices).*

We verified the effect of chamber isolation on cell-to-cell interaction assays. We loaded one C2C12 cell and five PC3 cells in the devices. We cultured cells for three days. In one device, we did not apply any electrolytic isolation (control). In the other device, we generated bubbles to isolate the culture chambers for cell-to-cell interaction for three hours per day. The culture chamber sealed by electrolysis (Fig. 4-9 (A)) has significantly more C2C12 cells than the unsealed one (Fig. 4-9 (B)). This result implies that the growth factor secreted by the PC3 cells can enhance the proliferation of C2C12 cells. Fig. 4-8 (B) compares the number of C2C12 cells after three day culture between the control (non-isolated, non-interaction) and the cell-interaction assay.

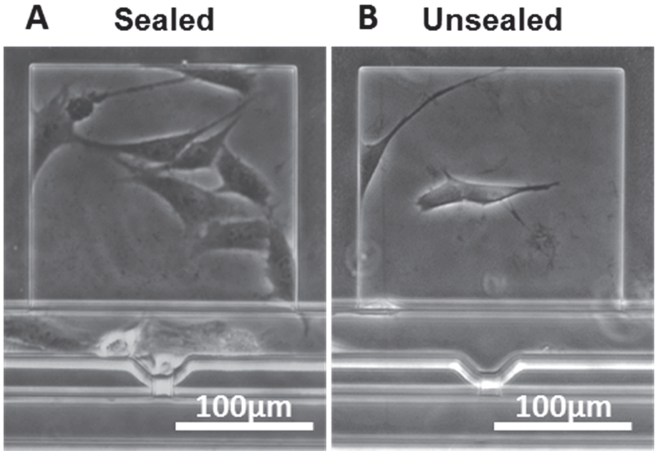

Fig. 4-9. Cell-cell interaction between C2C12 and PC3 cells: (A) C2C12 cell chambers after 3 day co-culture with five PC3 cells with electrolytic bubble isolation and (B) without electrolytic bubble isolation.

The effect of different cell pairing ratios was investigated and compared. As five PC3 cells secrete more growth factors than single PC3 cell, it is expected that proliferation enhancement would be more significant where C2C12 cells are paired with five PC3 cells. Fig. 4-8 (C) supports this hypothesis. In order to confirm that these effects indeed come from cell interaction as a result of building up of secreted factors in the isolated chambers, we conducted the same assay without electrolytic isolation as a control. Fig. 4-8 (D) shows that the pairing ratio does not give any effect on proliferation behavior without isolation of culture chambers. These experiments confirmed that both chamber isolation and cell ratio control are critical parameters that make significant effects on cell-to-cell interaction assays.

These preliminary results successfully demonstrated the capability of our microfluidic prototype devices as a potential platform for high-throughput cell-to-cell interaction assays.

4.9 Chapter Summary

A novel microfluidic cell-to-cell interaction chip has been developed for precise control of cell-pairing ratios and cell-to-cell interaction time. Using hydrodynamic capture schemes in a dual streams in laminar flow, we achieved a high cell capture rate over 80% in pairing cell ratios from 1:1 to 1:5. We implemented a cell isolation scheme based on electrolytic bubble generation and removal without using any on-chip microvalves or external pneumatic pumps. As the bubbles can be generated and removed within a minute, the presented platform can precisely control the cell interaction time for the paired cells inside a chamber. We confirmed that cell viability and proliferation rates are not affected by electrolysis and bubble removal operations. As a proof of the concept, we have performed the cell interaction assays by co-culturing C2C12 and PC3 cells in different cell-pairing ratios using the fabricated chip. Experimental results showed that proliferation rate was enhanced where C2C12 cells were co-cultured with higher pairing ratios of PC3 cells. This demonstrated the capability of our microfluidic prototype devices as a potential platform for high-throughput cell-to-cell interaction assays, and the compatibility of electrolysis for spatial temporal microenvironment control during cell culture.

Chapter 5

PAIRED SINGLE CELL CO-CULTURE MICROENVIRONMENT ISOLATED BY TWO-PHASE FLOW WITH CONTINUOUS NUTRIENT RENEWAL

This chapter introduces a single cell co-culture platform that implements actuation-free isolation using two-phase immiscible flows while providing continuous renewal of media through a semi-permeable membrane for long-term co-culture.

5.1 Introduction

The cancer cell niche is a complex microenvironment where cancer cells, endothelial cells (EC), macrophages, and mesenchymal stem cells (MSC) coexist [1], and tumor-stromal cell interactions can determine the development of the tumor [2]. It is believed that tumor cells exploit nearby normal cells to enhance growth, metastasis, and drug resistance. Conventionally, cell interactions can be studied by co-culturing two different cell types in the same petri dish. However, this dish based co-culture model lacks several key aspects to comprehensively understand cancer development. First, metastatic cancer cells typically metastasize as single circulating tumor cells (CTC); therefore, single-cell-derived tumorigenesis may be different from what is observed when co-culturing many cells [3, 4]. Second, conventional dish culture cannot provide an accurate model of tumorigenesis processes, as cell behavior will be affected by uncontrolled interaction with multiple neighboring cells [5]. In conventional interaction assays, two cell populations are simply mixed in a dish, so the spatial distribution of two cell types is not uniform, resulting in significant variation between locations. Some cells may be surrounded by many of the other type of cells in one region, while others may aggregate with the same type of cells in another region. As such, it is difficult to achieve precise ratio controlled co-culture in the conventional culture platforms. Third, dish-based culture lacks the ability to use small samples (<1,000 cells). This is important because it is difficult to acquire large samples of CTCs or primary samples. Finally, for highly heterogeneous populations such as cancer, dish-based co-culture can only monitor the average behavior, rather than tracking individual cell behavior. This can be an issue because some sub-populations in tumors have different metastasis potential. Although microfluidic technology provides better control over co-culture microenvironment, many platforms still load hundreds or thousands of cells in the device, so they lack single cell resolution as conventional co-culture in petri dishes [6-14].

Although the single cell co-culture on-chip allows for isolating single cells in the chamber, there are still two critical issues to be resolved: 1) Due to the small amount of secreted proteins from single cell, continuous perfusion can easily wash away the secretion and thus impair cell-cell interaction; and 2) As the platform aims to study the heterogeneity of single cells, the chamber-chamber cross-talk, which can cause undesired interaction, should be eliminated. In the previous works reported on the single cell-cell interaction [15, 16], the co-culture microenvironment of each cell group was not completely isolated. Thus, the cross-talk among different co-culture environments can inevitably distort the cell behaviors. Droplet based technology can naturally provide isolated co-culture microenvironment at single cell level; [17-19] however, droplet based cell culture is limited in the study of mammalian cells. First, most mammalian cells are adherent cells; therefore, suspension in a droplet can lead to anoikis, resulting in cell apoptosis [20]. Second, it is difficult to continuously provide fresh media to each droplet, so the nutrition in the isolated droplet depletes over time. Previously, our group reported two different platforms, which are capable of controlling the isolation time of paired cells by pneumatic valve or electrolytic bubble generation and removal [21, 22]. In these platforms, the isolation time was optimized based on the accumulation of signaling proteins and nutrition depletion.

Nevertheless, it is difficult to determine the optimal cell interaction time, especially for cancer cells, a highly heterogeneous population. Cells with low metabolism rates, which are likely to be quiescent and drug resistant, may need longer interaction times, while high metabolism rate cells, which contribute to rapid growth, may need a short interaction time. In order to fully characterize the sub-populations in the tumor, we should not miss any sub-population behaviors. In addition, the difference in proliferation rates after culturing several days (some chambers with more cells and others with less cells) will make the situation even more complicated.

In this work, we used a semi-permeable membrane for cell-cell interaction studies. The semi-permeable membrane under each micro-chamber can provide stable nutrient supply for cells, while retaining the secreted signaling proteins for interaction, without using any external control mechanisms for micro-chamber isolation. We incorporate immiscible oil isolation to achieve stable channel isolation in a simple and robust way. As a result, the device can operate without any external components such as micropumps or electrical control signals. For proof of feasibility, we demonstrated the interaction between UM-SCC-1 (head and neck squamous cell carcinoma) cells and endothelial cells (EC). Secreted cytokines from ECs can boost the growth of UM-SCC-1 cells as compared to control experiments where UM-SCC-1 cells were cultured alone.

5.2 Microfluidic Device Operation and Device Fabrication

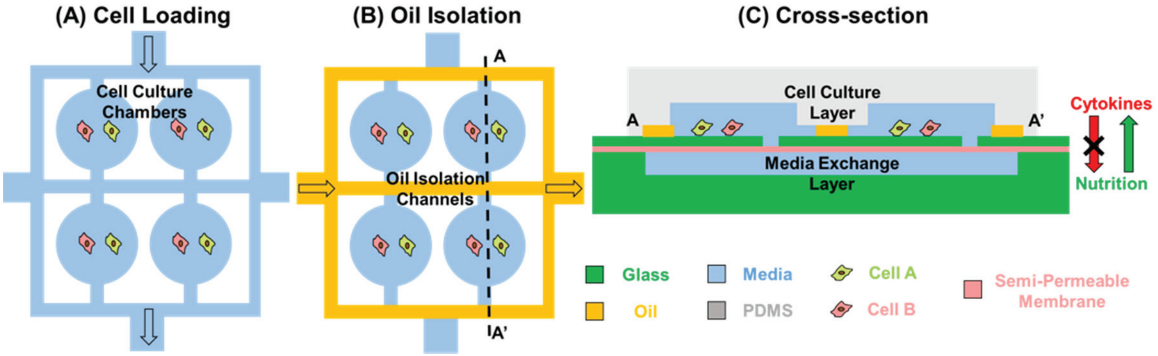

Fig. 5-1. Schematics of the proposed cell-niche-on-chip. (A) Cells are loaded and captured in each chamber by paring with different types of cell. (B) Oil is introduced from left to right in the upper layer to isolate the culture chambers by immiscible oil. (C) Illustration of cross-sectional view of the device shows that secreted cytokines are accumulated inside the chamber for cell-cell interaction, while the nutrition can be steadily supplied through a semi-permeable membrane.

The presented platform provides three functions: pairing of single cells for co-culture, oil isolation to avoid the cross-talk between chambers, and nutrient renewal through the semi-permeable membrane. To pair single cells, the hydrodynamic cell capture scheme is implemented. Using two capture sites per chamber, two cells can be captured in the same chamber as shown in Fig. 5-1 (A). After cell capture, the chambers are isolated by an immiscible oil phase. The oil flows left to right, so the cell chambers sandwiched by two parallel oil channels are isolated (Fig. 5-1 (B)). The nutrition can be supplied to the cells in the isolated chamber through the semi-permeable membrane (2k Daltons Cut-off molecular weight), while the secreted cytokines are accumulated inside the chamber because their molecule sizes (typically tens of kDa) are too large to escape (Fig. 5-1 (C)). In this manner, secreted cytokines are retained inside the chamber for cell-cell interaction, while the nutrition can be steadily supplied through a semi-permeable membrane.

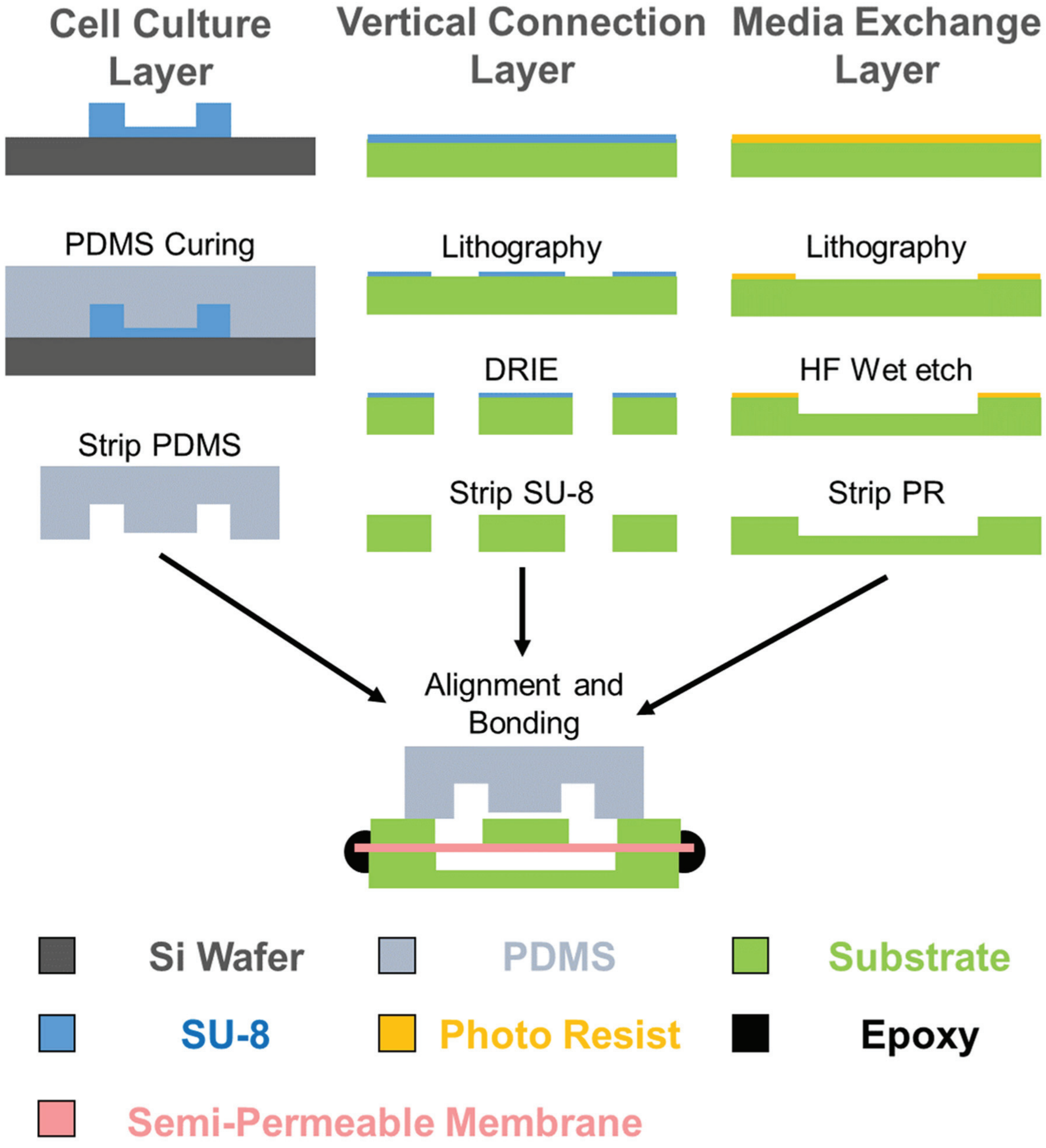

Fig. 5-2. Fabrication process of the cell-cell interaction chip.

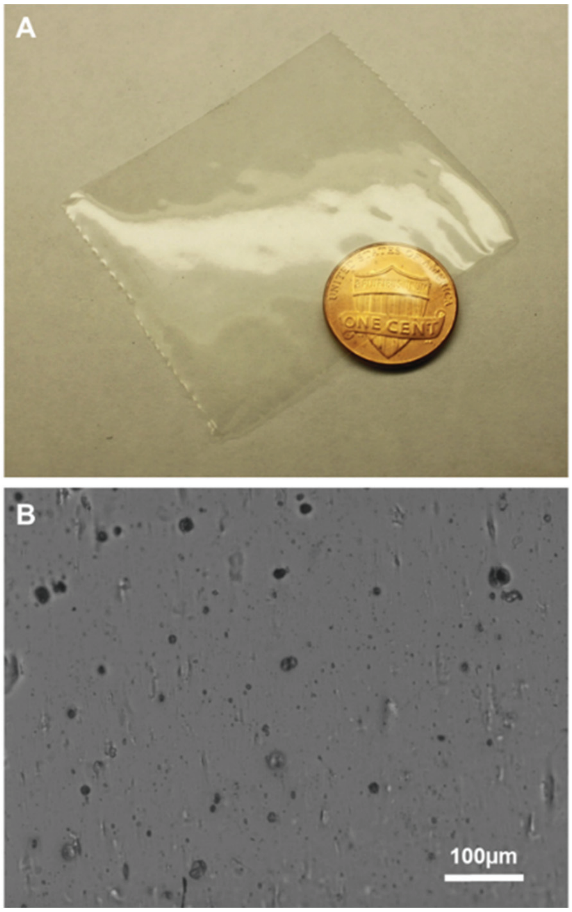

Fig. 5-3. The semi-permeable membrane used for nutrition exchange: (A) photo and (B) microphotograph.

Three layers (cell culture layer, substrate with vertical connections, and the media exchange layer) were fabricated separately, and then all three layers were aligned and bonded (Fig. 5-2). For the cell culture layer, three masks were used to fabricate a SU8 (Microchem) master mold: the first mask for a shallow (10 μm) interaction bridge, the second mask for microfluidic channels and cell culture chambers (40 μm), and the third mask for oil isolation channels (100 μm). The PDMS (PDMS, Sylgard 184, Dow Corning) layer was fabricated using the standard soft lithography processes. We used a 100 μm-thick fused silica wafer (Fused silica wafer, University wafer, MA) for substrate. In order to form vertical connections, a 50μm SU-8 layer was spin-coated and patterned and used as the mask for DRIE. The fused silica was etched through by DRIE (Pegasus glass etcher), and the residual SU-8 was removed by PG Remover (Microchem). The media exchange channel was formed by HF etching of a glass substrate. The media exchange layer has many pillars (100 µm by 100 µm) to support the semi-permeable membrane (Dialysis Membrane 2K MWCO, Fisher Scientific) on top, and the images of semi-permeable membranes are shown in Fig. 5-3. The PDMS channel layer and the vertical connection layer were treated with oxygen plasma and then aligned and bonded together. Finally, the bonded PDMS-fused silica, semi-permeable membrane, and media exchange layer were all assembled and sealed utilizing UV cured Epoxy (OG147, Epoxy technology).

5.3 Cell Capture Mechanism

In order to capture specific number of cells in each culture chamber, a cellular valving mechanism is used [23-25]. In this hydrodynamic capture scheme, two types of flow paths are created in the design: one is a central path and the other is a serpentine path, as shown in Fig. 5-4 (A). The hydraulic resistance of each path is inversely proportional to its flow rate. The long winding structure of the serpentine path is designed to increase the hydrodynamic resistance, so that the flow rate in this path is lower than that of the central path. Thus, the cells are likely to be guided to the central path and captured. Since the opening of the central path is slightly smaller (Height: 10 µm, Width: 10 µm) than the size of typical mammalian cells, the cells are sterically captured and plug the gap. Once the cell is captured, it blocks the flow in the central path and the remaining cells will flow through the serpentine path and be captured in the next chamber. With proper geometric design, a capture rate of ~90% can be achieved [25].

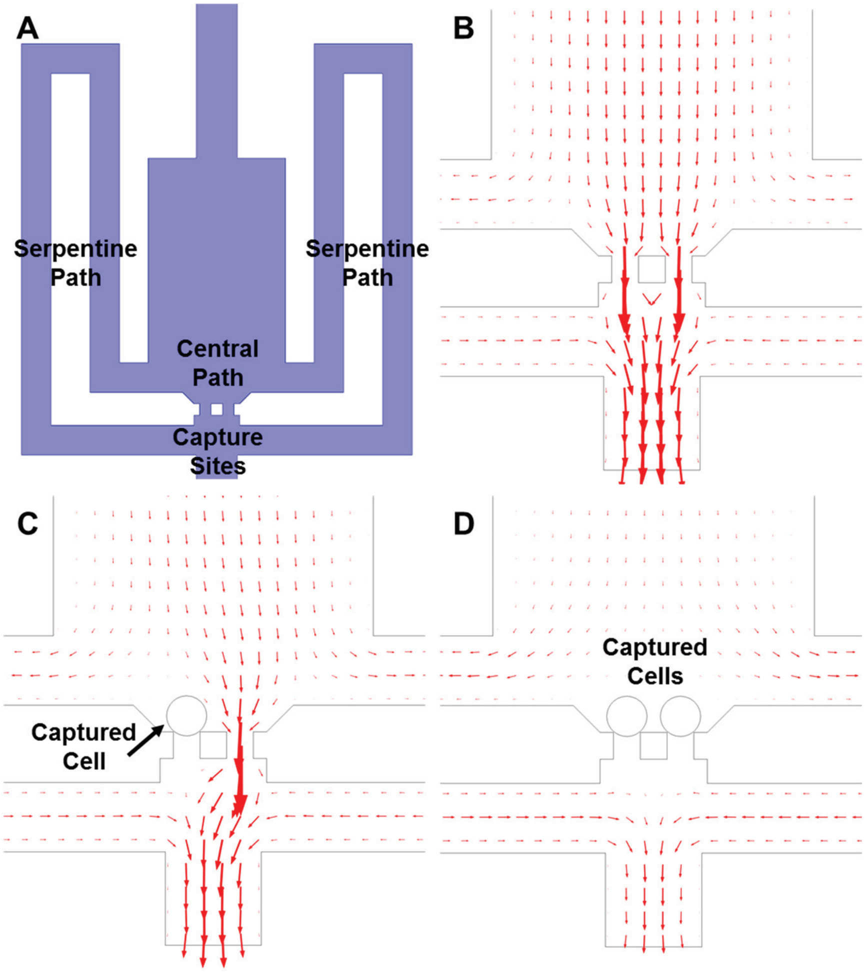

Fig. 5-4. Simulations of flow velocity and pressure during cell capture in a chamber by COMSOL 4.3: (A) schematics of cell capture scheme showing two capture sites, a central path, and two serpentine paths, (B) The simulated flow pattern before cell capture. The red arrows indicating flow direction and velocity suggest that the cells are likely to be guided to the capture sites and get captured by either of capture sites. (C) After one capture site is taken, the next cell is guided and captured in the other capture site. (D) Once both capture sites are taken, the flow resistance through the central path becomes higher than that of serpentine paths, so the next coming cells will flow through the serpentine paths to the downstream.

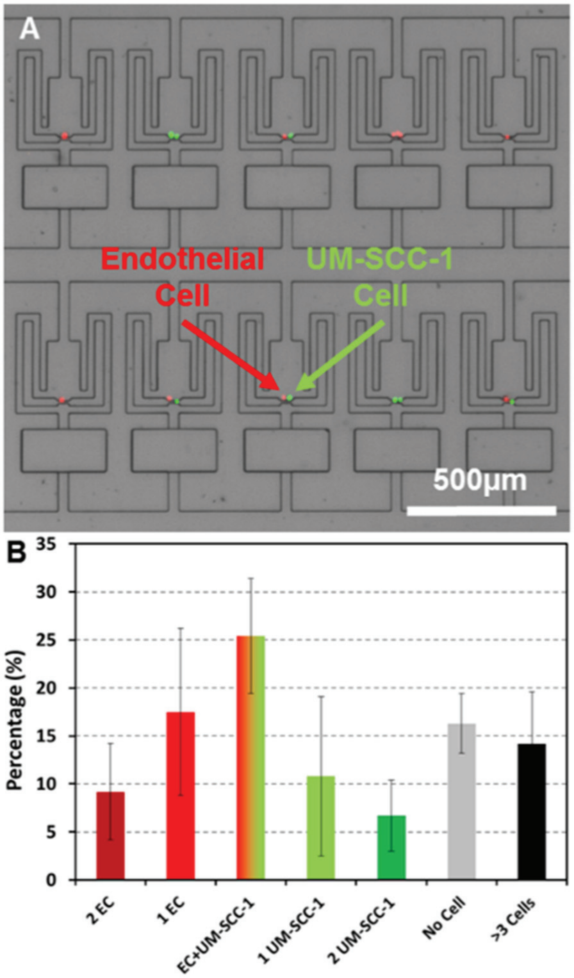

Fig. 5-5. Multiple cells captured in a chamber: (A) Capturing of different combinations of UM-SCC-1 and endothelial cells (EC), and (B) the capture rate of different cell combinations in an array of chambers with two capture sites when loading the mixed cells of UM-SCC-1 and EC at a 1:1 ratio.

To pair cells for the interaction, we designed two capture sites in each chamber. As 90% of individual capture sites capture exactly one cell, the number of captured cells in each chamber is determined by the number of capture sites in the design. As demonstrated by Fig. 5-4 (B), as the flow resistance of the central path is smaller, the first coming cell is likely to be captured by either capture site. The second coming cell will be captured by the other empty capture site (Fig. 5-4 (C)). Once both capture sites capture cells, the flow resistance through the central path becomes higher than that of serpentine paths, so the next coming cells will flow through the serpentine paths to the downstream (Fig. 5-4 (D)). Using this mechanism, we can achieve a high cell-pairing rate in each chamber, and the same mechanism can work for higher number of cells per chamber. As the size of most mammalian cells is similar, there is no selectivity for cell type. Thus, the ratio of captured cells will be similar to the composition of cells in cell solution. For co-culture of two cell types, we loaded a 1:1 ratio of the mixed cells to maximize the probability of 1:1 cell-pairing in the chamber. Fig. 5-5 (A) shows ten chambers capturing various combinations of cells after cell loading, and four chambers captured a pair of one UM-SCC-1 cell and one endothelial cell. Using two capture sites in each chamber, 25% of chambers capture exact a pair of two cell types, and other combinations can be generated simultaneously (Fig. 5-5 (B)). The cell behavior of different combinations can be compared side by side in the same device, so the device-to-device variation can be obviated.

5.4 Two-phase oil isolation

The immiscibility between oil and water can be an ideal way to isolated microchambers (oil-water two-phase isolation). Previous works demonstrated isolation of water droplets in oil by optimizing channel geometry and hydrophobicity. Pico-liter water droplets can be generated in oil, [26-28] and each single droplet can be used as a nano-lab for cell analysis [29]. Mammalian cells were cultured in droplets, but cell anoikis and media depletion in the droplet limit these technologies only to short term culture (less than one day) [17-19]. On the contrary, the conventional media perfusion platforms can allow cell culture longer than two weeks without affecting cell viability [25]. These isolating microenvironments, however, need bulky external components such as pneumatic pumps or function generators for control. In this work, we combine the advantages of these two approaches by integrating immiscible isolation for adherent cell culture and incorporating a semi-permeable membrane under each chamber to allow for continuous media perfusion [24, 26].

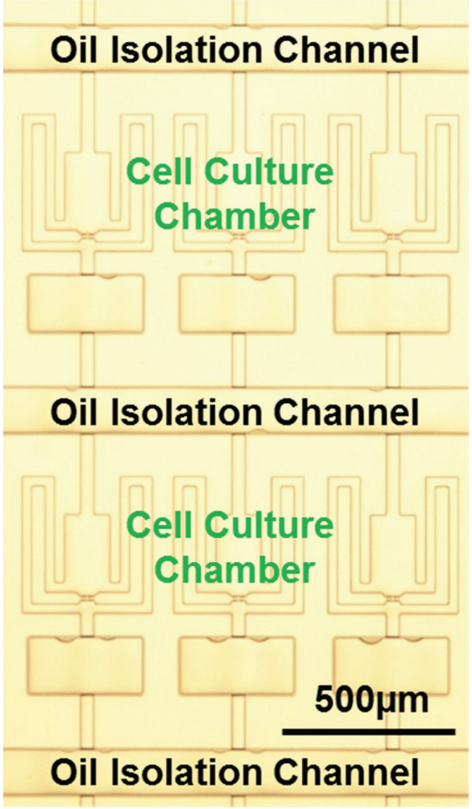

Fig. 5-6. Fabricated cell-cell interaction device. The cell culture chambers are separated and isolated by oil channels for cell-cell interaction.

In order to provide high cell viability for the long-term culture in our application, we optimized channel geometry to control the oil flow as shown in the Fig. 5-6. We designed a higher and wider channel (100 µm by 100 µm) for oil isolation paths and a narrower design (30 µm by 40 µm) for cell loading channels. In this channel configuration, the oil flow, driven by the negative pressure applied, can easily fill the wider channel and thus completely isolate the cell culture chambers, though oil has poorer affinity to the protein-coated hydrophilic channels. It is difficult for oil to invade the cell culture chamber because the collagen coated PDMS is hydrophilic. As a result, the channel geometry can guarantee good oil isolation while protecting cells inside the culture chamber. Fig. 5-7 shows the immiscible oil isolation process in the channel. A pair of cells were loaded in the chamber as shown in the Fig. 5-7 (A). When negative pressure was applied from the left, the oil filled the horizontal channels to isolate all the culture chambers. As we balanced the pressure difference between all horizontal channels, isolation process did not affect the cells captured in the chamber (Fig. 5-7 (B)).

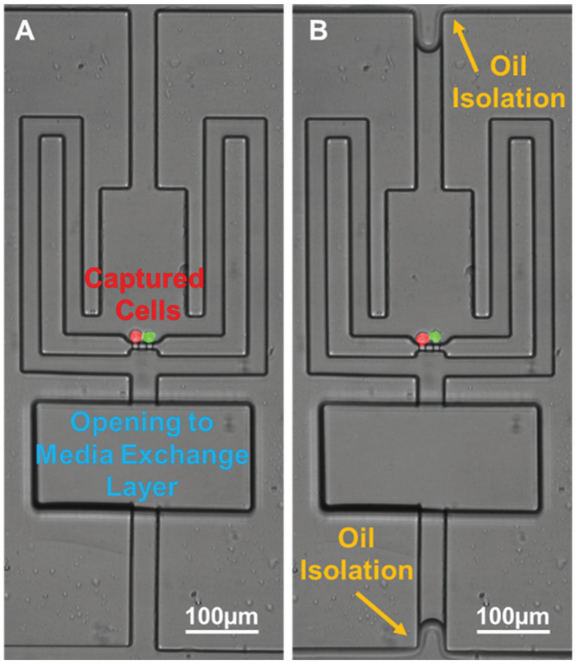

Fig. 5-7. Two-phase oil isolation: (A) before and (B) after oil introduction. The culture chamber forms an isolated microenvironment, and the oil isolation process does not affect the cells cultured in the chamber.

5.5 Fabrication of vertical connections by DRIE process

The presented platform has three critical functions: cell capture, oil isolation, and media exchange. To provide the same condition for all chambers on a chip, the symmetry of the channel routing is critical to maintain the pressure balance. However, symmetrical routing for both cell channels, oil channels, and media exchange channels on the same layer is unfeasible. To resolve this problem, we routed the media exchange channels in another layer, and then connect both layers by vertical connections. As the substrate thickness is 100 μm, it is impossible to make small vias (< 200 μm) by isotrpoic hydrogen fluoride (HF) wet etching. To make compact 3D integrated device, deep reactive-ion etching (DRIE) technology (Pagsus Glass etcher) was used instead. We used a fused silica wafer, which is pure silicon dioxide for two reasons: 1) The impurities in glass may interfere with the DRIE process, so it is difficult to achieve a high aspect-ratio deep etching on a glass wafer, and 2) as the fused silica is pure silicon dioxide, it has the same ideal optical and biocompatibility characteristics as glass [30].

We fabricated different opening sizes, ranging from 25 μm to 300 μm, and all sizes could be etched through by the DRIE process as shown in Fig. 5-8. The measured etch rate was shown in Fig. 5-8 (C). The smaller the opening is, the slower the etch rate becomes. However, even for the vias of 25 μm in square, the etch rate was still comparable (~87%) to the larger vias. The process is quite reliable within the range between 25 μm to 300 μm. The size of via connection (25 μm x 25 μm) that we formed by using a silica wafer is by an order of magnitude smaller than the connections formed through a PDMS membrane (typically ~100 μm), allowing for more compact design. [31, 32] The fused silica substrate gives better mechanical robustness than PDMS thin membrane because it has a higher Young’s modulus. Utilizing the presented 3D vertical integration technique, we can eliminate the design constraints of conventional planar fabrication processes and increase the density of integrated chambers in a given area.

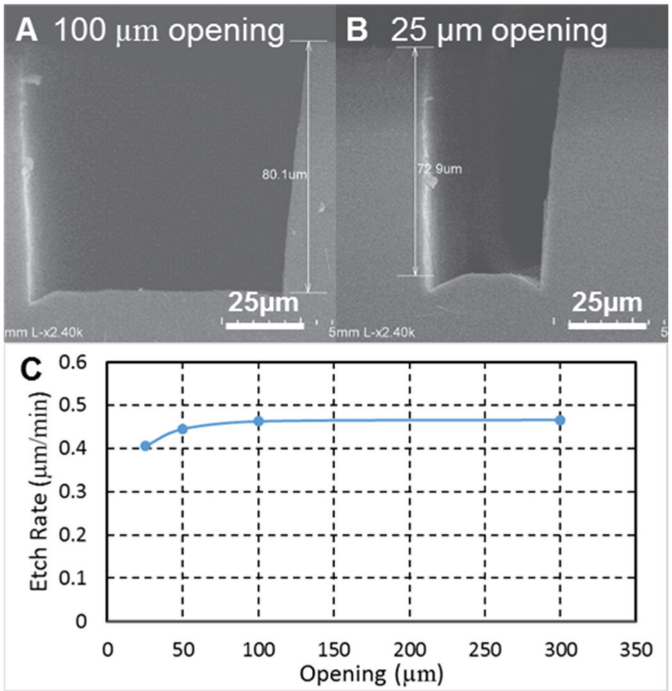

Fig. 5-8. Fabrication of vertical connections by DRIE: (A) the scanning electron microscope (SEM) of a 100 µm opening connection, (B) the SEM of a 25 µm opening connection, and (C) The etch rate of fused silica with different sizes of opening.

5.6 Continuous media renewal and protein accumulation

The small pore size of a semi-permeable membrane allows retaining signaling proteins which typically have a large molecular-weight for cell-cell interaction, while passing the nutrient in the media which typically have a small molecular weight. The semi-permeable membrane is sandwiched between the media exchange layer and the cell-culture chamber. Molecular weights of secreted proteins are typically larger than 10,000 Daltons; therefore, they will accumulate inside the culture chamber, inducing cell-cell interaction. Only the small molecules (e.g., glucose and amino acids) can pass the membrane, allowing continuous nutrient renewal from the media. Fig. 5-9 shows selective permeability based on molecular weight. The fluorescent dye in Phosphate-buffered saline (PBS, Gibco 10010) was loaded into the cell chamber, and the chamber was isolated by oil. Then, fresh PBS was supplied to the media exchange layer, so we can characterize the diffusion of fluorescent dyes through the semi-permeable membrane as a function of molecular weight by measuring the fluorescent intensity change. We used two different fluorescent dyes in the experiment: a small molecule dye (Fluorescein 5(6)-isothiocyanate, F3651, Sigma-Aldrich, Molecular weight of 389 Daltons) and a large molecule dye (Fluorescein isothiocyanate dextran, FD40S, Sigma-Aldrich, Molecular weight of 40,000 Daltons). Fig. 5-9 (A-D) demonstrates that the small molecule dye can diffuse through the semi-permeable membrane to the media exchange layer and then be washed away. The fluorescent intensity reduced to 27% from the initial intensity after 60 minutes. On the contrary, Fig. 5-9 (E-H) shows that the large molecule dye can be retained inside the chamber. After 60 minutes, the fluorescent intensity only reduced by 8%. Fig. 5-9 (I) plots the change of relative fluorescent intensity for two different dyes, respectively. It clearly shows the selective permeability for different molecule sizes, demonstrating the feasibility to continuous media renewal in the presented co-culture platform.

5.7 Proliferation enhancement by cell-cell interaction

As a proof of concept, we demonstrated cell interaction between UM-SCC-1 (head and neck squamous cell carcinoma) cells and endothelial cells (EC). Endothelial cells are known to secrete a number of growth factors that enhance the growth of tumors [33]. We compared co-culture of one UM-SCC-1 and one EC with single cell culture of one UM-SCC-1. After cell loading, the chambers were isolated utilizing the immiscible oil for three days. In the chamber loaded with the EC, the secreted cytokines from the EC were accumulated over time and boosted the growth of the UM-SCC-1. Fig. 5-10 shows the proliferation results after three days. The isolated single tumor cell barely proliferated (Fig. 5-10 (A)), while the UM-SCC-1 cell co-cultured with one EC proliferated to three cells

(Fig. 5-10 (B)). The proliferation rate of the co-cultured UM-SCC-1 cells was twice that of the isolated UM-SCC-1 cells (Fig. 5-10 (C)). Both isolated and co-cultured UM-SCC-1 cells showed good cell viability, implying stable nutrition supply through the semi-permeable membrane (Fig. 5-10 (D)) during the course of the experiments. By exchanging nutrition through the membrane, the presented platform can maintain the cell viability of 75% up to 7 days for longer experiments. These preliminary results successfully demonstrated the capability of our device retaining the secreted factors for interaction while providing stable media perfusion through semi-permeable membrane to maintain good cell viability.

5.8 Chapter Summary

We have successfully implemented a cell-cell interaction platform that can be used to co-culture a pair of cells in one chamber. The platform attains a high cell pairing rate of 25% and reliable chamber isolation by immiscible two-phase flows using oil. Although chambers are isolated, the nutrition can be supplied through a semi-permeable membrane, while the secreted signaling proteins can be retained inside the chamber for cell-cell interaction. The membrane selectivity based on molecular weights was verified utilizing fluorescent dyes. We achieved a compact integration of co-culture chamber arrays by stacking double layers through vertical via connections in the silica substrate. In the current chip, 56 chambers were implemented for proof of concept and we believe it can be easily extended to 1,000 chambers for high-throughput assays. The preliminary experiments have confirmed the increase in proliferation of cancer cells when co-cultured with endothelial cells, demonstrating the feasibility of the proposed microfluidic platform for studying tumor-stromal interaction by controlling microenvironments in cell niches.

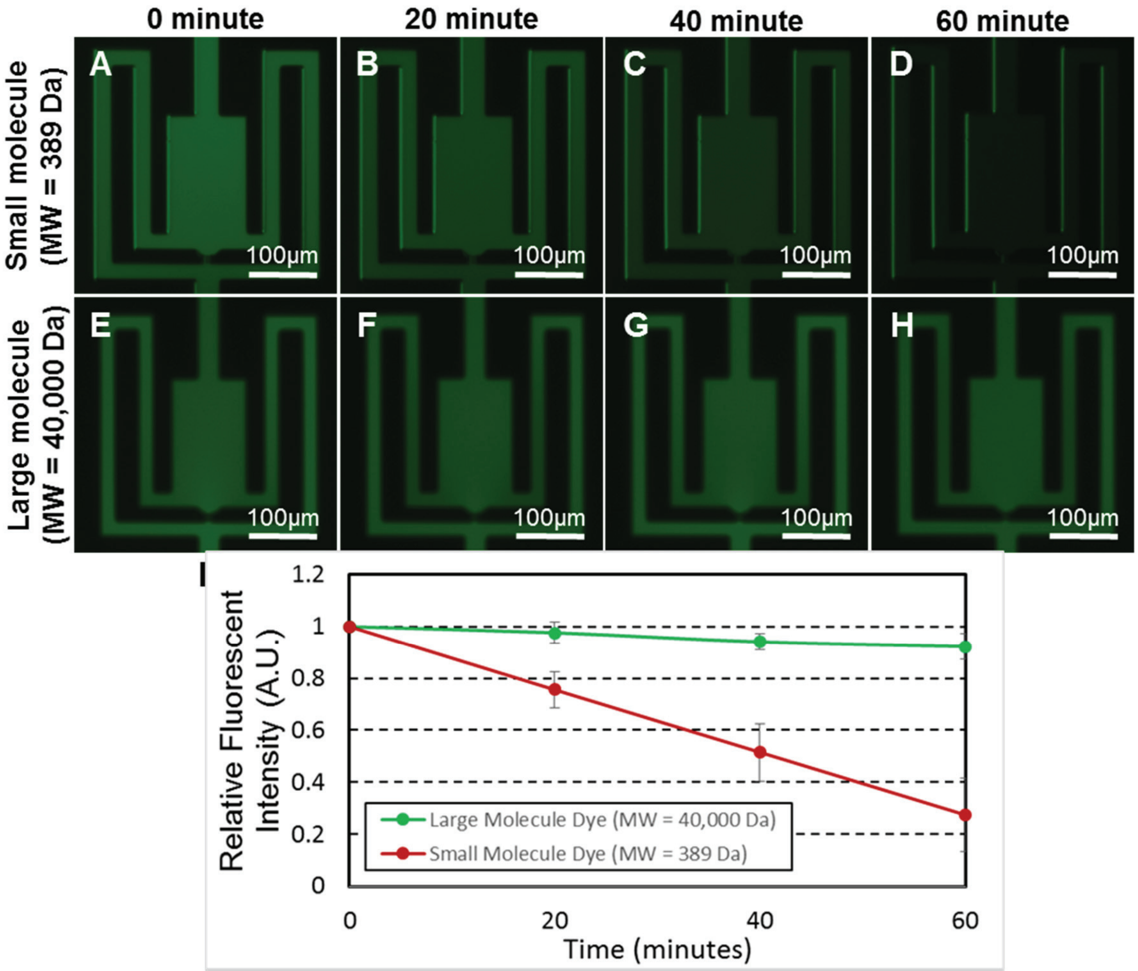

Fig. 5-9. The selectivity of retaining fluorescent dyes based on molecular weights. (A-D) Small molecule dye (MW = 389 Da) was gradually diffused out through a semi-permeable membrane: (A) initial fluorescent intensity, (B) fluorescent intensity after 20 minutes, (C) after 40 minutes, and (D) after 60 minutes. (E-H) Large molecule dye (MW = 40,000 Da) was retained in the chamber: (E) initial fluorescent intensity, (F) fluorescent intensity after 20 minutes, (G) after 40 minutes, and (H) after 60 minutes. (I) The plot of relative fluorescent intensity of fluorescent dyes in the chamber over time. The results clearly demonstrate that the small molecules (e.g., glucose, amino acids) can be exchanged, while the large molecules (e.g., signaling proteins) can be retained in the chamber for interaction (N = 5 chambers).

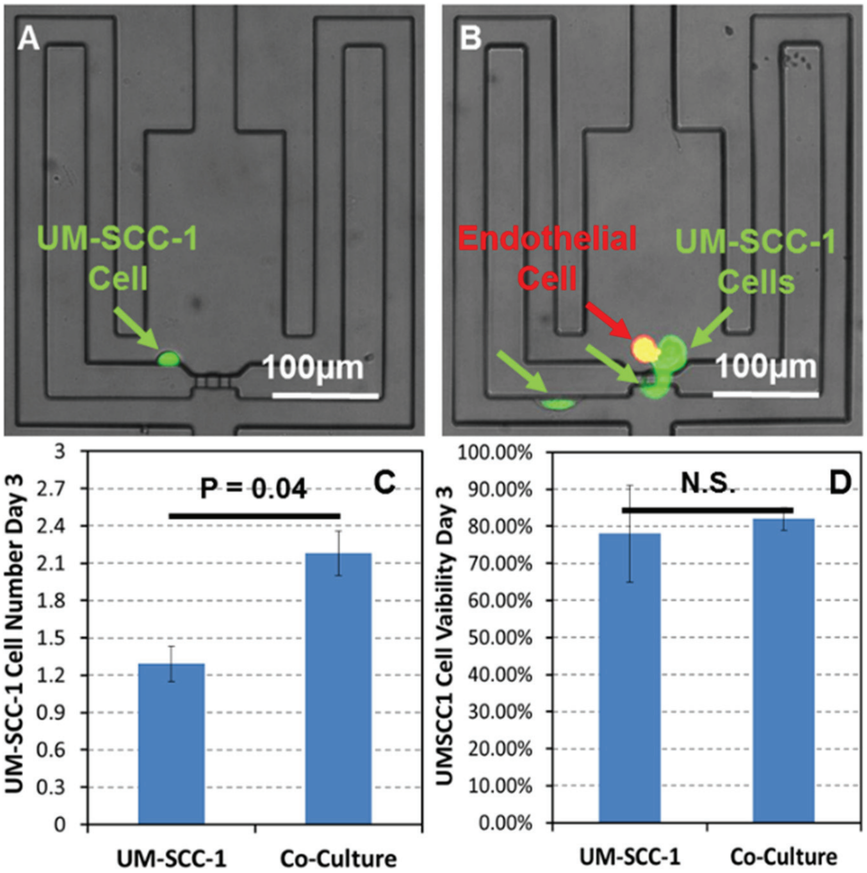

Fig. 5-10. Cell Interaction between UM-SCC-1 and EC for three days. (A) A single UM-SCC-1 cell after 3-day culture in the chamber. No proliferation was observed. (B) A pair of one UM-SCC-1 and one EC co-cultured for 3 days. After three days, one UM-SCC-1 cell became three cells. (C) The comparison between the proliferation rate of single UM-SCC-1 cell and the co-cultured EC - UM-SCC-1 cells. The result shows that the EC can enhance the proliferation of UM-SCC-1 cell. Data points represent means ± standard deviations (N = 4 devices), P = 0.04. (D) Viability of UM-SCC-1 in the chamber after 3-day culture shows that the cells were healthy in both cases. Data points represent means ± standard deviations (N = 4 devices), and no significant difference was observed.

Chapter 6

HIGH CAPTURE EFFICIENCY SINGLE CELL DUAL ADHERENT-SUSPENSION CO-CULTURE MICRO-ENVIROMENT

This chapter covers a dual adherent-suspension co-culture device, which can provide both a suspension environment for cancer cells and an adherent environment for stromal cells in close proximity by selectively patterning polyHEMA in indented micro-wells. In addition, the platform specializes in high capture efficiency. Up to 75% of all cells used for small samples (50 cells) can be captured, granting the potential to study rare cell populations such as primary cells.

6.1 Introduction

Cellular heterogeneity is a hallmark of multicellular life and plays a critical role in many disease states [1-2], including cancer. A contributor of cancer heterogeneity in many tumors is cancer stem-like cells (CSCs). There is currently a wealth of data supporting the presence of CSCs, particularly in breast cancers [3-10]. In the CSC model, only a small subset of cells actually retains the ability to differentiate and initiate new tumors, as opposed to a traditional stochastic model of cancer where any cancer cell at low frequency may reform/recapitulate the entirety of a tumor [6, 9]. CSCs have been implicated in metastasis, radiation and chemotherapy resistance, and relapse after therapy, making them important clinical targets [5, 8, 11-12].

It is believed that fibroblasts are a major micro-environmental regulator in cancer and are critical in tumorigenesis and metastasis [13-15]. Recently, it was demonstrated that the co-transplant of cancer cells and fibroblast can boost the formation of cancer and that cancer associated fibroblast can skew the differentiation or de-differentiation of cancer stem cells [14-15]. As we expect different regulation of CSC stemness with fibroblast co-culture, it is critical that we have a co-culture platform where we can maintain clonal spheres while providing signaling from adherent stromal cells.

Although cancer-stromal interactions are critical in tumorigenesis, conventional dish based co-cultures lack the capability to study cell heterogeneity by tracking single cell behavior [13-15]. To understand a heterogeneous population such as cancer, ideal co-culture platforms should be able to provide single cell resolution for characterizing individual cell behavior rather than the averaged behavior [16]. There are a number of previous works reporting on microfluidic platforms for cell-to-cell interaction studies [17-29]. Most of them still require loading hundreds or thousands of cells in a device; thus, they still lack single cell resolution [17-23]. Droplet based technology can provide a high-throughput combinatorial pairing of cells, but it lacks capabilities for long-term cell culture, limiting its applications in practical co-culture assays [24]. Recently, several microfluidic devices reported cell pairing and cell-to-cell interaction at single-cell resolution [25-29], but those works were limited to adherent cell co-culture. For applications in cancer biology, 3D suspension culture is believed to maintain the stemness of CSCs, but suspension environments are too harsh for most adherent stromal cells (e.g. fibroblast cells, endothelial cells) [30, 31]. In this work, we developed the first co-culture platform combining both suspension and adhesion culture in close proximity inside the same chamber. Compared to previous single-cell platforms [32-35], the presented platform also specializes in high capture efficiency, up to 75% of the loaded cells, even for small samples (50 cells). This enables the study of rare cell populations such as samples taken from primary cells.

6.2 Design and Fabrication

The presented co-culture platform is composed of an inner suspension culture chamber, an outer adherent culture chamber, and narrow interaction channels connecting them (Fig. 6-1(A)). The whole device consists of 120 co-culture units (15 by 8) (Fig. 6-1(B)), and each unit is composed of the two culture chambers connected by 7 narrow (cross-section 3 μm by 20 μm and 100 μm long) channels. To facilitate suspension and adherent culture on the same device, two layers of PDMS are used in fabrication. The bottom layer was patterned with indented microwells that were selectively coated with Poly-hydroxyethylmethacrylate (polyHEMA, Sigma-Aldrich), which has been extensively used as an adhesion blocking coating material [34]. The top channels layer is patterned with microfluidic channels for flow control and chambers for co-culture.

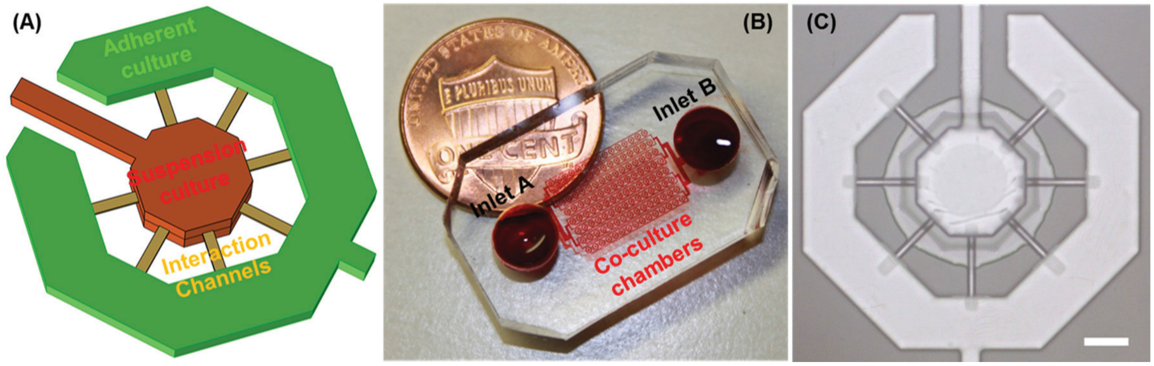

Fig. 6-1. microfluidic chip for adhesion suspension culture: (A) 3D schematics of a co-culture chamnber having inner suspension culture chamber, outer adherent chamber and interacting channel connecting them, (B) photograph of a fabricated device having 120 chambers within 8 mm by 10.5 mm core area, and (C) micrograph showing a fabricated co-culture chamber (scale bar: 100 μm).

These two PDMS layers (channel layer and substrate layer) were separately fabricated using standard soft lithography processes, and then aligned and bonded together, as shown in Fig. 6-2. For the channel layer, two masks were used to fabricate a SU8 (Microchem) master mold: the first mask for narrow interaction channels (3 µm height) and the second mask for main microfluidic channels and adherent cell culture chambers (40 µm height). One mask was used to fabricate the SU8 master mold for the substrate layer which has indented chambers (40um depth) for suspension cell culture. To make the chambers non-adherent, polyHEMA was filled in the suspension culture chambers by a stamping process developed in our lab. The polyHEMA is in ethanol solution (60 mg/mL in 95% ethanol) and was coated on the substrate PDMS. A piece of blank PDMS was pressed on top to squeeze out the excess solution leaving the polyHEMA only in the indented micro-wells. To improve the coating quality, the indented PDMS substrate was plasma treated to increase the hydrophilicity. This will increase the likelihood that the polyHEMA ethanol solution will deposit only to the patterned PDMS substrate while stamping. Then, the substrate and the blank PDMS stamp were put on a hot plate at 110 ℃ for 2 hours under pressure, in order to facilitate evaporation of ethanol through the PDMS layer. During the evaporation of ethanol, the polyHEMA layer will be deposited in the suspension cell culture chambers. To remove the undesired residual polyHEMA on the surface, 30 seconds of 800 Watt plasma polymer etching was performed using the YES polymer striper (the expected etching depth is 0.3 µm). This results in a clean PDMS surface with polyHEMA only left in the suspension culture chamber. The fabricated substrate is the then aligned and bonded to the other PDMS fluidic layer that contains the outer chambers and interaction channels. The fabricated device is shown in Fig. 6-1 (C).

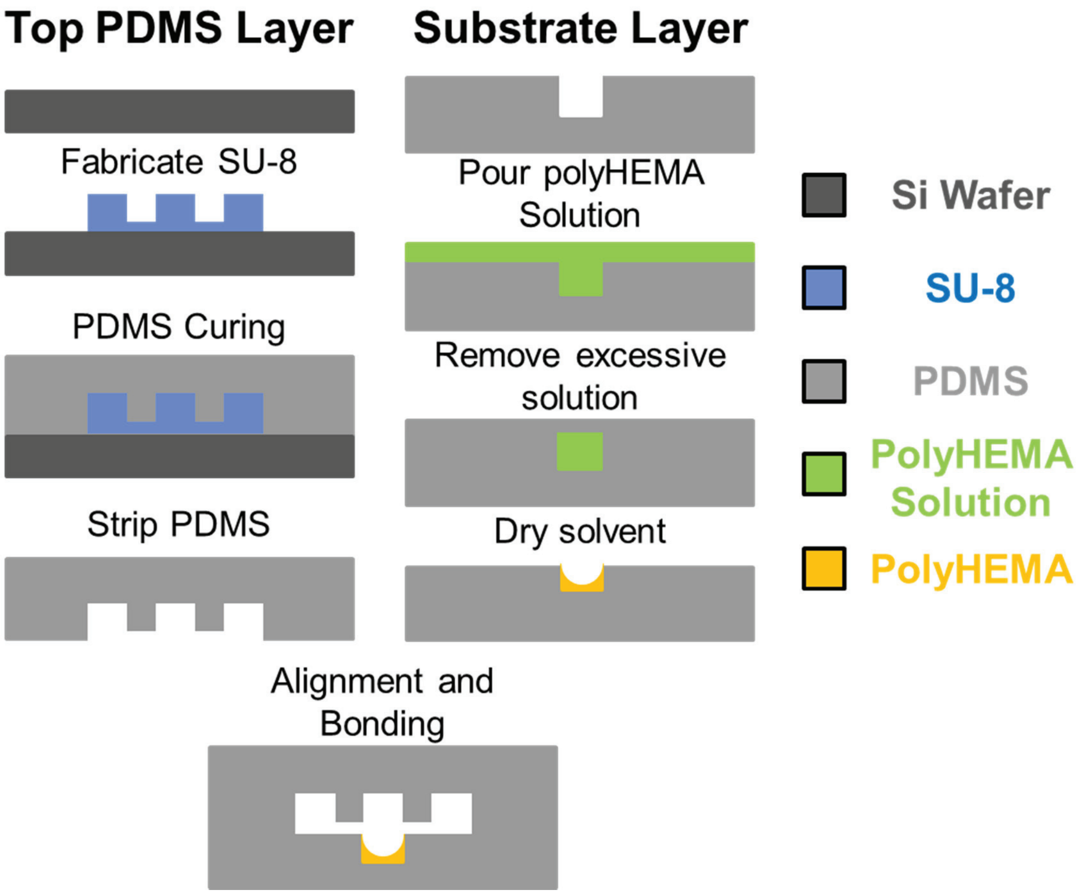

Fig. 6-2. Fabrication process of the adhesion/suspension culture chip.

6.3 Characterization of the fabricated surface

First, we examined the surface profile of the fabricated substrates by SEM. Fig. 6-3(A, B) shows the surface profile before the filling of polyHEMA. We can clearly visualize the vertical side wall of the indented micro-well. After polyHEMA filling, the side wall of the indented micro-well becomes smooth. This indicates that polyHEMA was deposited on the substrate. If we remove the polyHEMA by plasma etching, we can observe the exposed PDMS on the bottom of the micro-well clearly in a SEM picture (Fig. 6-4). This indicator was used to determine the proper etching time. In addition, we measured the surface profiles using a laser interference microscope (LEXT, Olympus), as shown in Fig. 6-3(C, D)). The deposited polyHEMA smoothens the cross-section of the micro-well. Based on the comparison of profiles, the polyHEMA coating depth at the center of the chamber is approximately 4 µm, which is sufficient to generate a non-adherent culture surface, based on our previous experiments.

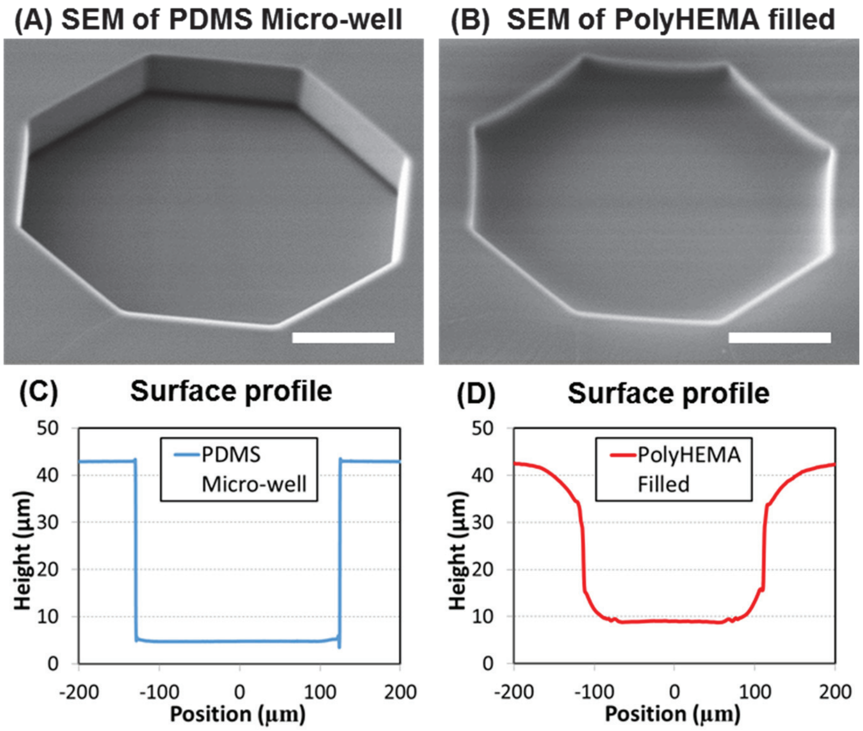

Fig. 6-3. Fabricated of non-adherent microwell: (A, B) SEM of microwell before and after filling polyHEMA and (C, D) surface profile of microwell before and after filling polyHEMA measured by LEXT. PolyHEMA was measured to be 4 µm thick in the center. (scale bar: 100 µm)

To verify the effect of polyHEMA coating, T47D breast cancer cells were cultured on the selectively coated substrate, compared with an uncoated PDMS substrate and a standard tissue culture plastic dish. (Fig. 6-5). Due to the difference of stiffness between PDMS (500kPa) and the polystyrene (PS) dish (1GPa), the observed cell morphologies were slightly different, but still, the cells were clearly attached on the PS dish and the uncoated PDMS substrate. The uncoated PDMS was patterned in the same way as the polyHEMA coated substrate (40um deep wells), and the cells are adherent both inside and outside of the wells (Fig. 6-5 (B)). Without the plasma etching process, a thin polyHEMA layer is formed on the top surface of the polyHEMA coated substrate. As such in Fig. 6-5(C), we observed that cells remain rounded and aggregated on both the top surface and within the microwells, demonstrating that the T47D could not adhere. To attain dual suspension and adhesion culture on the same substrate, the residual polyHEMA was removed by the oxygen plasma etch. As the residual poylHEMA is much thinner (< 0.5 μm) than the polyHEMA deposited in the wells (~ 4 μm), the polyHEMA coating inside micro-wells can be preserved, while removing all polyHEMA on the non-indented surface. Fig. 6-5(D) demonstrates the desired selective coating behavior. As the well is non-adherent, cells formed aggregation in the well, while an adherent monolayer has grown on its surrounding area. In addition to T47D cell lines, multiple cell lines including C2C12 (mouse myoblast), MDA-MB-231 (breast cancer), and HCC38 (breast cancer) cells were cultured on the substrate. The selectivity was observed in all these cell lines, indicating that the fabrication process is robust and reliable for suspension/adherent cell culture.

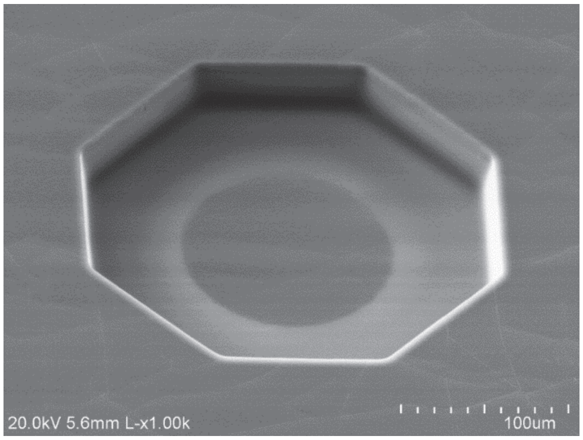

Fig. 6-4. PolyHEMA over-etched indented chamber. The PDMS substrate exposes at the center of the chamber.

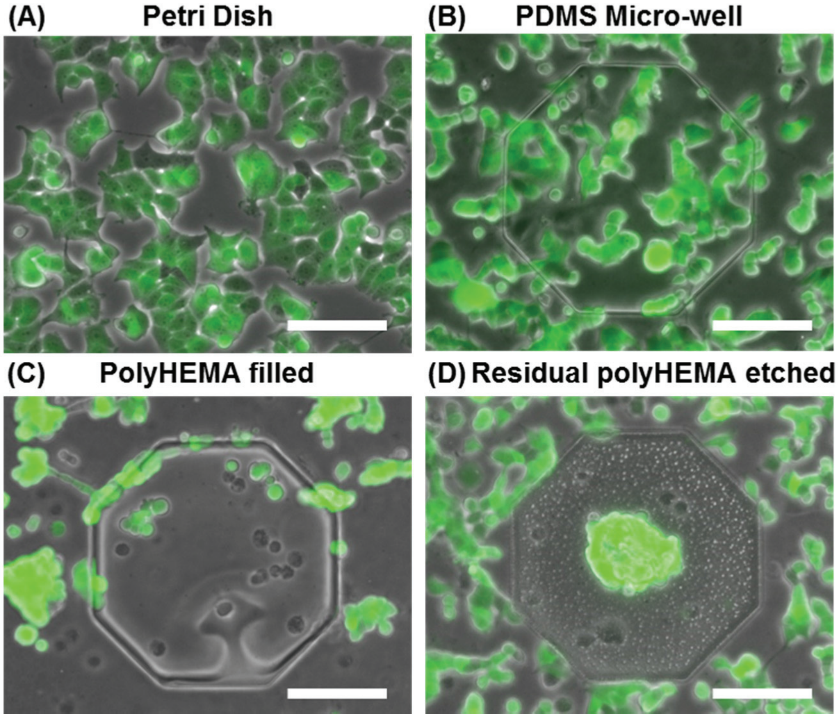

Fig. 6-5. T47D cells grow on the substrates of: (A) Petri dish (all adherent), (B) micro-well without coating (all adherent), (C) surface coated with polyHEMA (all suspension) and (D) selectively polyHEMA coated substrate (suspension in the microwell but adherent elsewhere). (scale bar: 100 µm)

6.4 Single cell isolation by Poisson's distribution

To guarantee that cells cannot migrate between the inner and outer chambers, the interaction channels are designed to be 3µm in height, preventing migration while allowing paracrine based interactions. During operation, the stromal cells in the outer ring will be loaded first, and then allowed time to adhere to the substrate. The single cancer cells will be then loaded and captured in the micro-well for suspension culture and single cell derived sphere formation. Once the single cell is loaded into the indented well, it will settle to the bottom of the well as demonstrated by the fluidic simulation shown in Fig. 6-6. As a proof of concept, we demonstrated co-culture of T47D (breast cancer) and C2C12 (mouse fibroblast) cells to model tumor proliferation enhancement via fibroblast cell signaling.

The C2C12 cells, which require an adherent environment, were first loaded in the outer chamber (Fig. 6-7(B)). The cells were cultured with serum media (DMEM with 10% FBS), which contains attachment factors that encourage cell adhesion. After one day, cells were attached and grew to monolayer (Fig. 6-7(C)). As the interaction is much narrower than the size of cell, all coming single cancer cells were captured in the inner chambers (Fig. 6-7(D)).

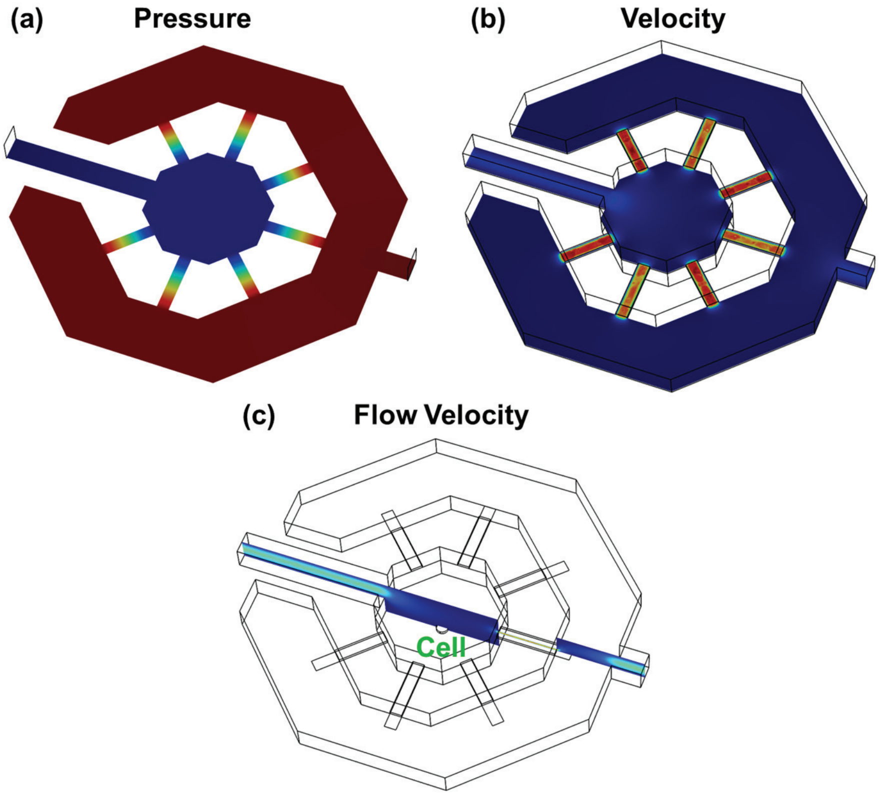

Fig. 6-6. The flow simukations of the cell capture design: (a) the pressure distribution, (b) the flow velocity of the xy-plane, and (c) the flow velocity of the xz-plane.

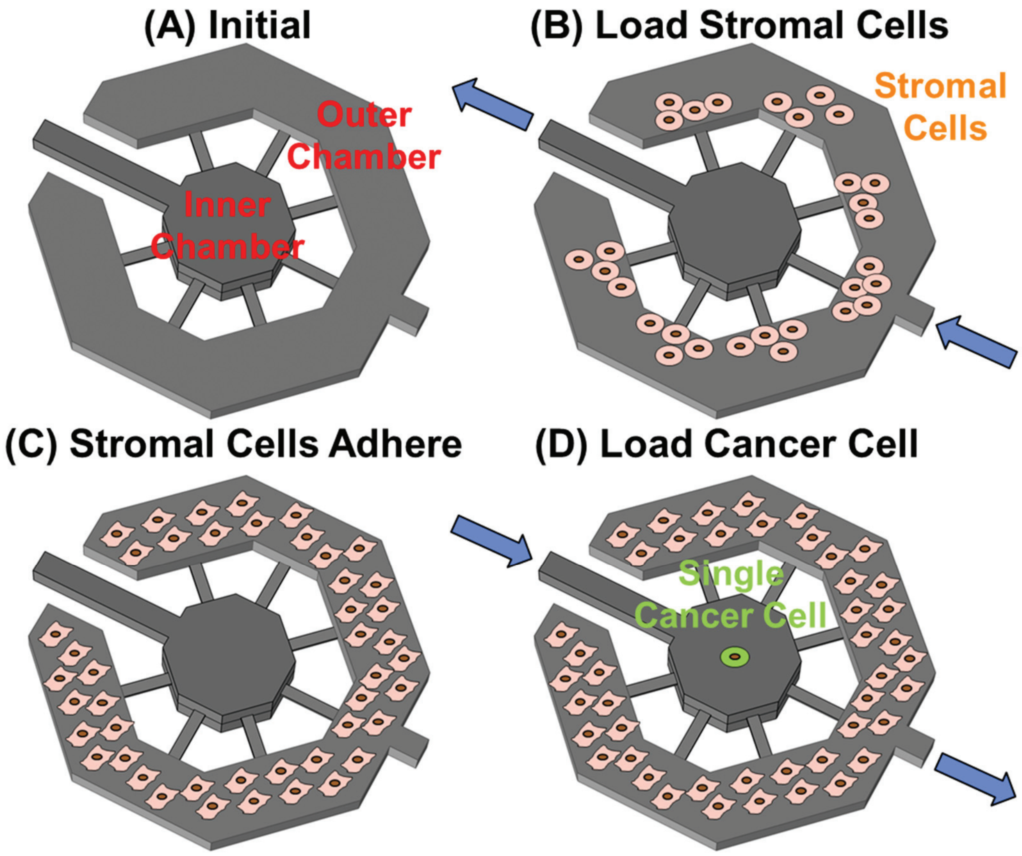

Fig. 6-7. Cell loading process of the adhesion/suspension chip: (A) the schematics of a chamber of adhesion/suspension chip, (B) C2C12 cells loaded in the outer culture chamber on day 0, (C) C2C12 cells adhered and grew to monolayer on day 1, (D) single T47D cell (green fluorescent labelled) loaded in the inner chamber on day 1.

Although conventionally hydrodynamic capture schemes can have higher capture rates (60-90%), they are not ideal for small samples such as primary cells or CTCs, due to lower cell capture efficiency (typically less than 10%). Additionally, it is difficult to implement a hydrodynamic capture scheme in our platform due to the high fluidic resistance of the narrow interaction channels. Compared to the hydrodynamic capture, that may lose cells through the serpentine (by-pass) paths, we can attain a high capture efficiency in the presented platform by collecting all incoming cells into chambers. Although the presented scheme cannot guarantee single cell in each chamber, the capture distribution of cells in the chambers should follow Poisson's distribution. When the number of coming cells is much smaller than the number of the chamber, it is likely to have single cell per chamber. As a proof of the concept, we loaded 50 cells in a device having 120 chambers, and 37 single cells were isolated in the chambers. The experimental results matched well with the Poisson distribution model (Fig. 6-8), showing that the capture scheme is suitable for the studies of small number (< 100) of cells.

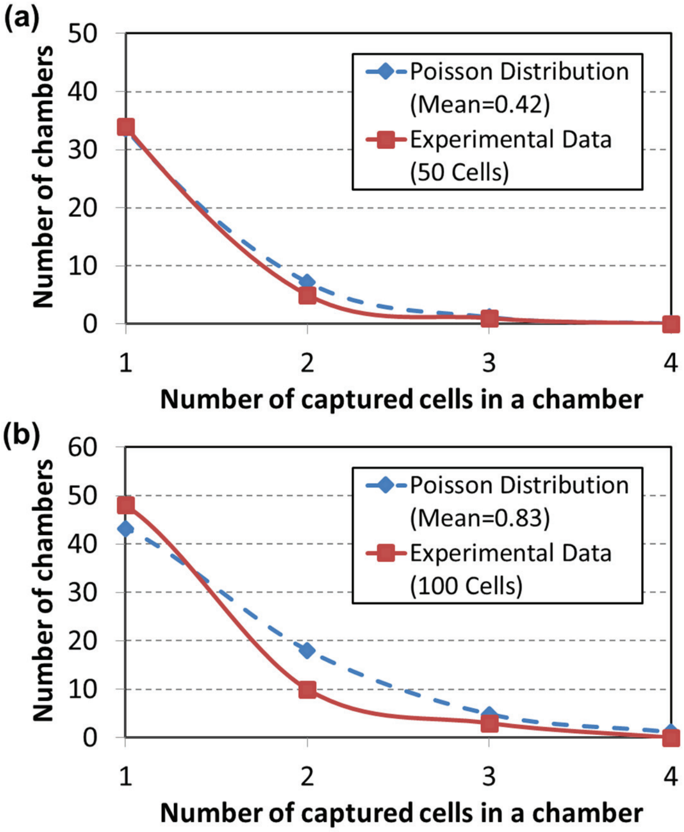

Fig. 6-8. The number of captured cell per chamber: (A) 50 cells loaded into a device with 120 chambers and (N=4) (B) 100 cells loaded into a device with 120 chambers (N=4). The experiment results match well with the Poisson distribution.

When having large number of cells, we can optimize the cell capture rate by controlling the number of loaded cells. As shown in the Fig. 6-9, if loading too less cells, we tend to have many empty chambers, while loading too many cells can cause a lot of multiple captured chambers. Give the number of chamber per device, we can calculate the ideal number of loaded cells for the optimization of capture rate (~ 35 %). Although controlling the number of 50-100 cells can be difficult, two times higher or lower number of cells can only cause the degradation of performance by merely 20%, meaning that we can have robust loading performance.

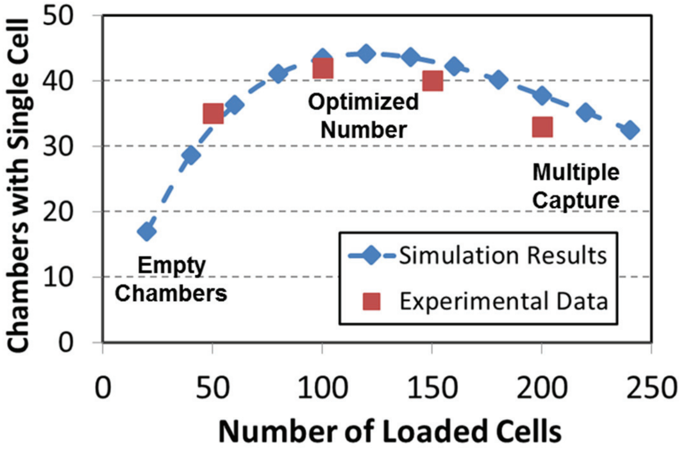

Fig. 6-9. The number of chamber capturing exact single cell per device (120-well device) with different number of loaded cells.

6.5 Single cell derived sphere formation under the influence of stromal cells

Though we designed the interaction channels to facilitate stromal interactions, it is important that we verify how secreted factors behave in the chamber. As shown in the simulations (Fig. 6-10) when media flows inward (from the outer ring to the inner suspension culture chamber), the media containing secretions from the fibroblasts can affect cancer cells located inside the inner chamber. Conversely, when media flows outward (from the inner suspension chamber to the outer ring culture chamber), the secretions from the cancer cell can affect the fibroblasts. When the flow is stopped, secreted factors from each population can diffuse throughout the chamber, allowing reciprocal interactions. As such, the platform has the potential to control the direction and type of interaction. In our first trials, we alternated the flow direction, flowing inward for 12 hours and outward for 12 hours during each 24-hour period.

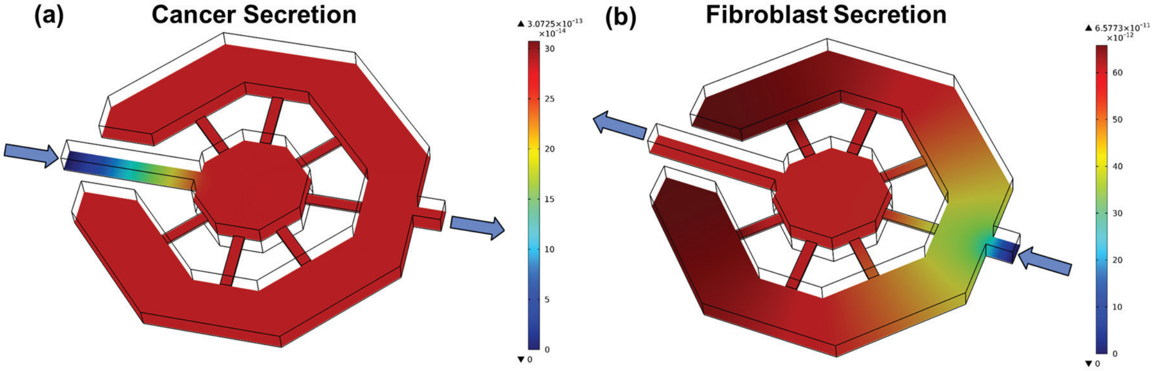

Fig. 6-10. The simulations of cell secretion concentration in the chamber: (A) the discribution of cancer cell secretion, while the media flows from inner chamber to outer ring and (B) the discribution of fibroblast cells secretion, while the media flows from outer ring to inner chamber. The simulation was performed by assuming that single cell secretes 1^{-20} *mole of proteins per second, its diffusion coefficient is* 1^{-10} m^2/s*, and single cancer and 50 fibroblast cells in the beginning.*

After co-culturing the two populations for 14 days, we quantified the interaction efficacy by counting the number of single-cell-derived spheres present throughout the 120-well array [35, 36]. Compared to single cancer cells cultured without stromal interaction (Fig. 6-11 (A)), the cancer cells co-cultured with fibroblasts (Fig. 6-11 (B)) have doubled the sphere formation rate, indicating that fibroblast cells can boost the stem/progenitor cell potential in the cancer population (Fig. 6-11 (C)). Co-cultured spheres were observed to be larger (Fig. 6-11 (D)), indicating a higher proliferation rate as well. In summary, we successfully demonstrated high capture efficiency in a close-proximity dual suspension and adherent co-culture environment, and also performed a co-culture assay for proof of concept.

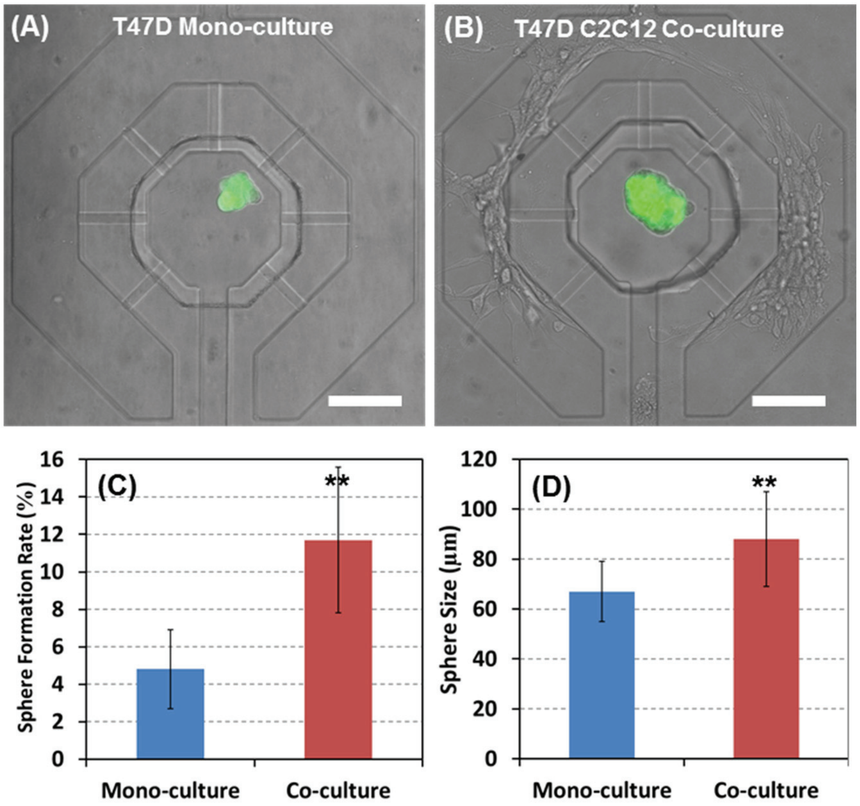

*Fig. 6-11. Differential cancer (T47D) sphere formation with and without co-culture with C2C12 cells: Representative cancer sphere on day 14 (A) without C2C12 or (B) co-cultured. (C) Sphere formation rate with and without co-culture after 14-day culture. (N = 4), ** P < 10-2. (d) Average sphere size with and without co-culture (N = 4), ** P < 10-2.*

6.6 Chapter Summary

We developed a single cell co-culture platform combining both suspension and adhesion culture in close proximity. Utilizing innovative substrate patterning, only the indented micro-chambers were non-adherent, while cells can adhere to other regions. The adhesion/suspension dual culture micro-environment has been proven reliable for 5 cell lines indicating its broad potential. The final device was fabricated by combining the substrate with a patterned channel layer, designed with a capture efficiency matching a Poisson distribution, specializing in small sample handling. For the 50 loaded cells, we can capture 37 single cells in individual microwells. As a proof of concept, we have performed a cell interaction assay, co-culturing C2C12 and T47D cells in the fabricated chip. Experimental results showed that both sphere formation rate and the size of the single cell derived spheres were enhanced when T47D cells were co-cultured with C2C12 cells. This demonstrates the capability of our microfluidic prototype device to perform cell-to-cell interaction assays with a dual adhesion/suspension culture environment.

Chapter 7
SINGLE CELL DETACHMENT AND RETRIEVAL IN THE MICROFLUIDICS USING PHOTO-ACOUSTIC EFFECT ON CNT/PDMS SUBSTRATE

This chapter presents a novel cell detachment technique which provides good spatial resolution to selectively retrieve single cells from microfluidic chips. Pulsed laser beams were used to generate deformation on a CNT-PDMS composite film on which cells were adhered and cultured. Due to rapid (in milliseconds) deformation, cells can be detached in a non-thermal manner. This enables high cell viability and produces a negligible effect on the mRNA expression of single cell.

7.1 Introduction

Due to the genomic instability and epigenetic dysregulation of cancer cells [1-2], intratumor heterogeneity, imposes challenges in cancer therapy, as individual cells within a tumor can respond differently to the same drug. However, cell heterogeneity cannot be easily studied by conventional dish-based assays, which measure the averages from tens of thousands of cells at a time. Although FACS and MACS sorting instruments can separate tumor cells into several sub-populations based on cell surface markers, the markers may not correlate well with the cell behaviors that matter in the treatment [3]. Recent developments in microfluidics has enabled single-cell resolution assays that isolate and culture cells in an array of microchambers [4]. Cellular development can be monitored in the chamber, and in-situ sensors can characterize the metabolism or secretions of the single cells [5-7]. Nevertheless, when single cells proliferate in a chamber, it is difficult to investigate the heterogeneity between two daughter cells from the same progenitor cell. As it is known that cancer stem cell (CSC) can undergo either self-renewal or differentiation, and this decision can determine the development of tumor, fully characterizing two sister cells can facilitate the fundamental understanding of the regulating pathways for cell renewal and differentiation in cancer development [8-9]. Since the off-chip analysis can provide higher multiplexing capability up to 96 mRNA (Fluidigm, C1, Biomark) and 32 proteins (Fluidigm, CyTOF) for single cell analysis, the capability to retrieve a target single cell for off-chip analysis is critical.

Conventional cell detachment schemes, such as trypsinization or PNIPAAm-based detachment [10], do not provide good spatial resolution; cells are detached from the entire substrate. The PALM CombiSystem developed by Zeiss can detach cells adhered on a laser-absorbing film. However, this system can only operate on an open substrate, so it is difficult to integrate it with microfluidics, which are ideal platforms for single cell manipulation and analysis. The methods using capillary vacuum or localized trypsin exposure can provide simple alternative methods for selective cell retrieval, but they are still limited to open substrates [11-12]. Cell release through photo degradation of a film substrate provides better spatial resolution and can be integrated with microfluidic devices, but this process generates acid and leads to toxicity that may affect cell behavior and expression. [13]. In 2012, an IR-triggered single cell detachment method using CNT substrates was reported [14]. However, cell viability was poor under direct laser irradiation because of heat-induced cell necrosis. Recently, we demonstrated cell detachment using ultrasound-induced cavitation [15], but unfortunately this approach only works on open substrate and is not compatible with microfluidic arrangement due to acoustic attenuation in PDMS.

Here, we present a new cell detachment technique which provides good spatial resolution to selectively retrieve single cells from microfluidic chips. Pulsed laser beams were used to generate deformation on a CNT-PDMS composite film on which cells are adhered and cultured. Due to rapid (in microseconds) deformation, cells can be detached in a non-thermal manner. This enables high cell viability and produces a negligible effect on the mRNA expression of single cell.

7.2 Cell Detachment Mechanism and Fabrication of Microfluidic Platform

We developed this novel cell detachment technology based on photo-acoustic mechanism. The cell detachment setup is illustrated in the Fig. 7-1. To convert the optical power from the laser to a mechanical force for cell detachment, we developed a two-layer composite substrate (shown in Fig. 7-2 (A)), which composes of a light absorbing material and a polymer layer. The light absorbing layer will transform the optical energy to heat, and the generated heat leads to the thermal expansion of polymer. The rapid (<1μs) deformation of the polymer layer can lead to high enough shear stresses to detach the cells on the surface. Due to the high optical absorption of CNTs, they were first investigated as a light absorbing layer and deposited via CVD (Chemical Vapor Deposition). Later testing showed that sputtered Au/Pd alloy (20nm) can be used as the alternative light absorbing material, which has better uniformity and higher potential for scalable fabrication. PDMS, a commonly used microfluidic material, was selected as the polymer layer for three merits: (1) the high thermal expansion coefficient of PDMS helps transformation of the heat to a mechanical force [15], (2) the low thermal conductance can isolate the cells above from the heat of the CNT surface, preserving cell viability, and (3) PDMS has good bio-compatibility. The SEM picture of the CNT film (~ 6 μm) grown on the substrate is shown in the Fig. 7-3. (A). To uniformly coat thin PDMS on CNT substrate, we diluted PDMS in Hexane with a 1:1 ratio. A 3μm PDMS layer can be achieved using a 6,000 rpm spin coating speed (Fig. 7-3. (B)). The relation between PDMS thickness and the dilution ratio and spinning rate is characterized in Fig. 7-4.

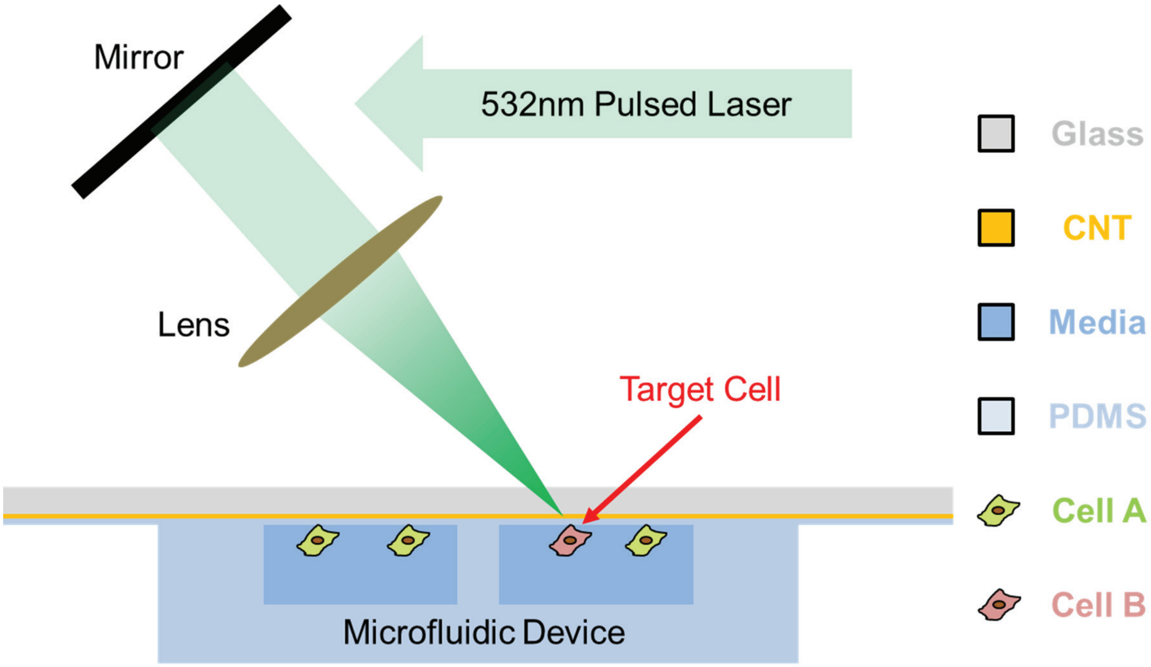

Fig. 7-1. Schematic diagram of single cell detachment setup. The target cell was cultured in the microfluidic chamber and observed under microscope. Once being selected, the pulsed laser can be used to detach the target cell.

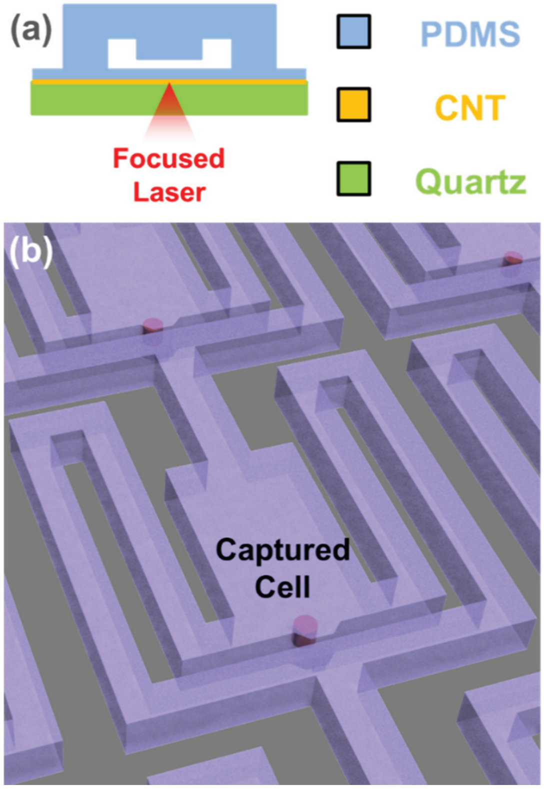

Fig. 7-2. Schematic diagram of a single cell assay platform: (A) cross- sectional view and (B) 3D micro-chamber schematics with a captured cell.

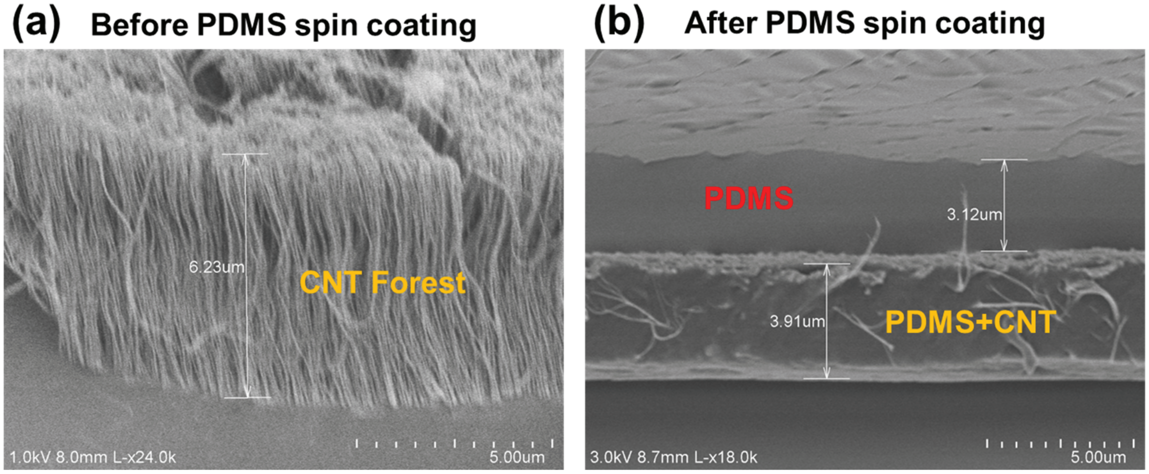

Fig. 7-3. SEM images of the substrates: (A) the CVD-grown CNT forest on quartz substrate (B) the embedded CNTs in the PDMS layer after spin coating of PDMS.

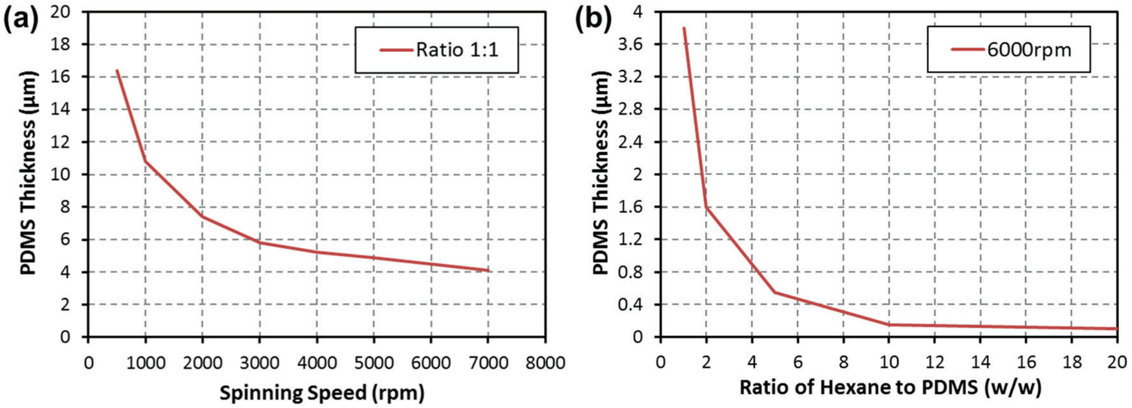

Fig. 7-4. The correlation between the PDMS thickness and the spinning rate and the Hexane dilution ratio: (A) PDMS thickness versus the spinning rate, when diluted 1:1 to Hexane, and (B) PDMS thickness versus dilution ratio, when fixing to 6000rpm.

7.3 Selective Cell Detachment and Retrieval at Single Cell Resolution

Using the hydrodynamic capture scheme, reported in chapter 3, we can capture single cells in each chamber of a microfluidic culture array with high efficiency (around ~ 80-90% [4]). The captured cells can grow in the microfluidic chamber for more than 14 days, so cell assays as diverse as drug screens, cell-to-cell interaction, cell migration, sphere formation, and cell differentiation can be performed in our platform. During such assays, it can be beneficial to retrieve cells of interest for further downstream analysis. A focused short-pulse of laser (3-5 ns) can be applied for cell detachment at single cell resolution. The laser energy (~0.1mJ per pulse) is absorbed by the CNT layer grown on the substrate (Fig. 7-3), transferring the energy to heat. The PDMS expands and deforms, inducing a high shear force to detach the cell. The low thermal conductivity of the PDMS layer insulates the cell culture area, so the generated heat does not affect cell viability. Fig. 7-5 illustrates the detachment process of a single skov3 (ovarian cancer) cell. In the beginning (Fig. 7-5 (A)), the cell was captured in the chamber and allowed to attached to the substrate over a few hours. When the laser is used on the substrate near the cell, a shear force is generated and the cell detached (Fig. 7-5 (B)). Driven by reversing the gravity flow, the cell travels upward to be retrieved in the outlet (Fig. 7-5 (C)). Fig. 7-6 demonstrates the precise spatial resolution of the presented detachment scheme. After focusing the irradiation to just one side of the cell, we can partially detach the cell, leaving one side anchored and the other free.

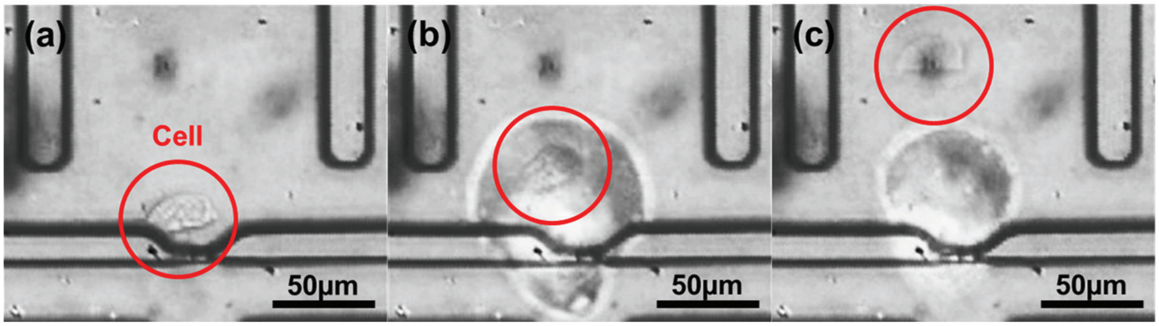

Fig. 7-5. Process of single cell detachment: (A) before detachment, (B) after detachment, (C) when the detached cell flowing away.

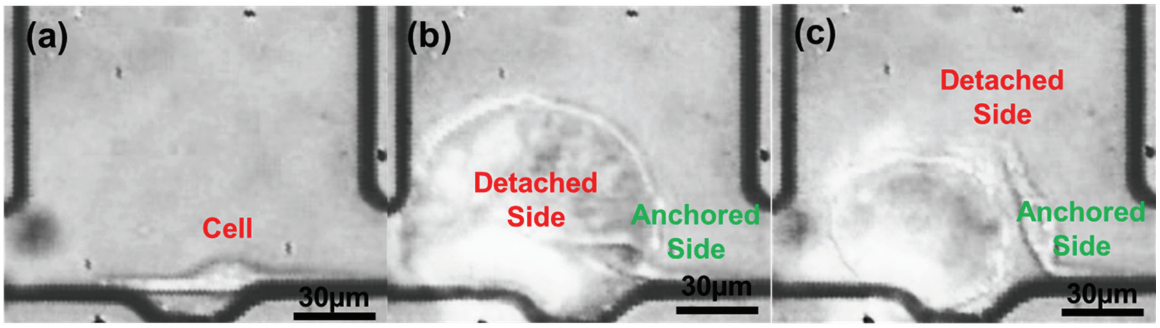

Fig. 7-6. Partial cell detachment: (A) before detachment, (B) after detachment, (C) a partially-detached cell anchored on one side and detached on the other.

To facilitate further analysis (e.g. mRNA RTq-PCR) on the target cell, we designed a novel cell retrieval scheme that can achieve high yield retrieval and avoid undesired contamination from residual cells left in the inlet. In the cell loading phase, media flows from inlet to outlet (in Fig. 7-7, flowing from top to bottom), so the cells can be captured at the capture sites (Fig. 7-7 (A)). In the detachment phase, we first detach the cells from the lower chambers (the even rows in the array) by applying pressure from the right (Fig. 7-7 (B)). The detached cells in the lower chambers will be guided upward and retrieved in the left outlet. Then, we can detach the upper chambers (the odd rows in the array) by applying the pressure from the left (Fig. 7-7 (C)). The detached cells in the upper chambers will be guided upward and retrieved in the right outlet. Using the alternating parallel channels in an array, we can retrieve all the cells from left and right outlets, so the residual cells in the inlet during cell loading will not contaminate the sample.

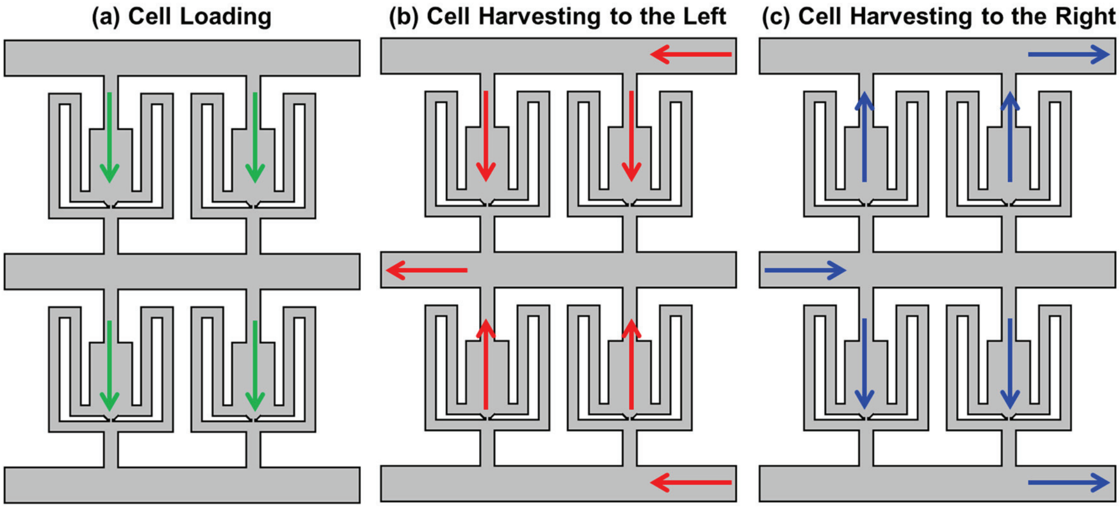

Fig. 7-7. Cell retrieval process by flow control: (A) Cell loading phase - The media flows downward in all chambers and cells are hydro-dynamically captured in each chamber, (B) Cell harvesting to the left. After cell detachment, we harvest the cells in the lower chambers (the even rows) first by applying pressure from right to left. The detached cells in the lower chambers will be guided upward and then collected in the left outlet (C) Cell harvesting to the right - We retrieve the cells in the upper chamber (the odd rows) by applying pressure from left to right. The detached cells in the upper chambers will be guided upward and then collected in the right outlet. Using the alternating parallel channels in an array, we can retrieve cells from all the chambers.

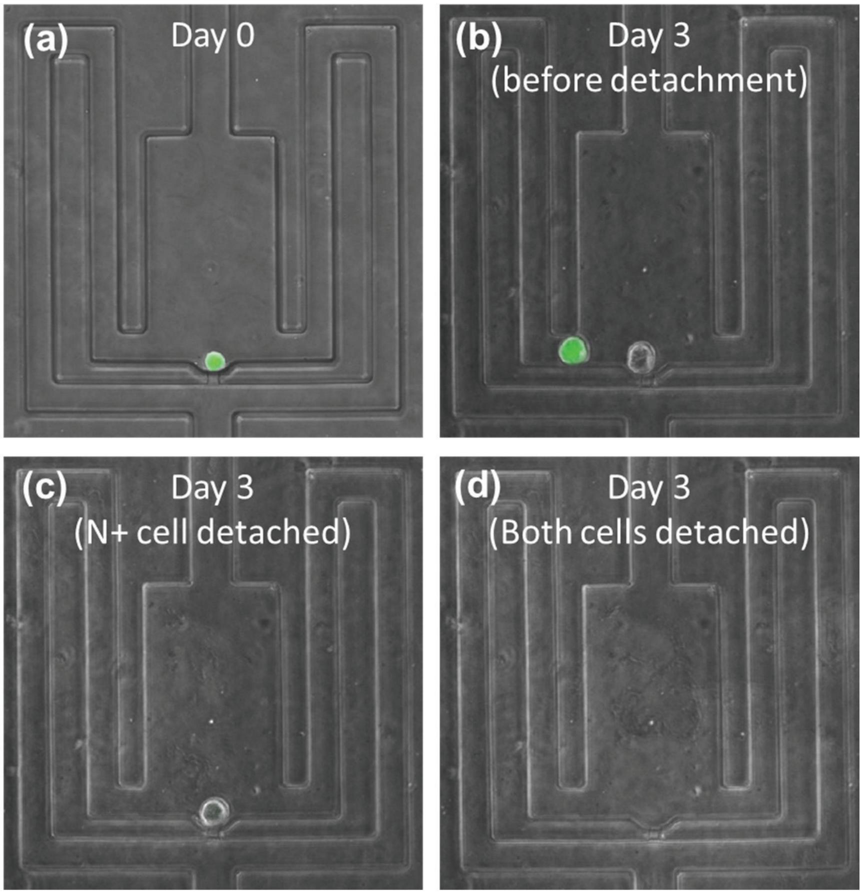

Fig. 7-8. Selective retrieval of asymmetrically divided cells. (A) single Notch+ T47D cells was captured in a chamber. (B) After 3 days, the Notch+ cell asymmetrically divided to one Notch+ (green) and Notch- (non-green) cell. (C) The Notch+ cell was selectively detached and retrieved first. (D) Notch- cell was successfully retrieved.

As a proof of concept, we demonstrated the selective retrieval of asymmetrically divided Notch+ T47D (breast cancer) cells. The Notch pathway is a signaling pathway that regulates cell self-renewal and differentiation, and high Notch expression is related to stem-like properties and higher tumor initiating potential [16-17]. To monitor Notch pathway activation, we transduced T47D cells with a lentiviral (pGreenFire1) Notch reporter containing multiple Notch response elements upstream from a minimal CMV promoter regulating destabilized GFP. Due to asymmetric division, some Notch+ cells generate Notch- daughter cells, and this regulation is essential in the tumor development. Notch+

cells were loaded in the chamber on day 0 (Fig. 7-8 (A)), and one was selected that asymmetrically divided to one Notch+ (green) and one Notch- (non-green) cell after 3 days (Fig. 7-8 (B)). First, we retrieved the Notch+ cell, and, due to the high spatial resolution, the Notch- cell stayed at its original place (Fig. 7-8 (C)). Then, the Notch- cell was retrieved (Fig. 7-8 (D)), so two daughter cells could be analyzed and compared.

7.4 Viability of Detached Cells

Fig. 7-9 shows the cell's viability after recovery from laser induced cell detachment. In this case, a single cell was detached and then retrieved in a 96-well plate (Fig. 7-9 (A - C)). 4 days after the detachment, it proliferated to around 30 cells. Using LIVE/DEAD staining (Life Technologies, USA), we found that all cells were viable. In Fig. 7-10, we compared the cell viability in our method with that of the conventional trypsinization-based method. Remarkably, cells that underwent the laser detachment scheme show slightly better cell viability than those that underwent the conventional trypsinization process, indicating that the presented method is suitable for the applications which need further culturing of the samples after retrieval. In addition to the viability test, we visualized the cells after detached by the laser or trypsinization process under SEM (Fig. 7-11). Trypsinization digest all the membrane proteins (giving the cells a smooth surface (Fig. 7-11 (B, D)), while the laser detachment preserves such surface proteins (leaving the cells rough under the SEM (Fig. 7-11 (A, C)). The preservation of these membrane proteins enhances the cell survival, helping to explain the observed higher cell viability. In addition as the surface markers will be preserved in the laser detachment process, marker staining will not be affected and can be performed soon after retrieval.

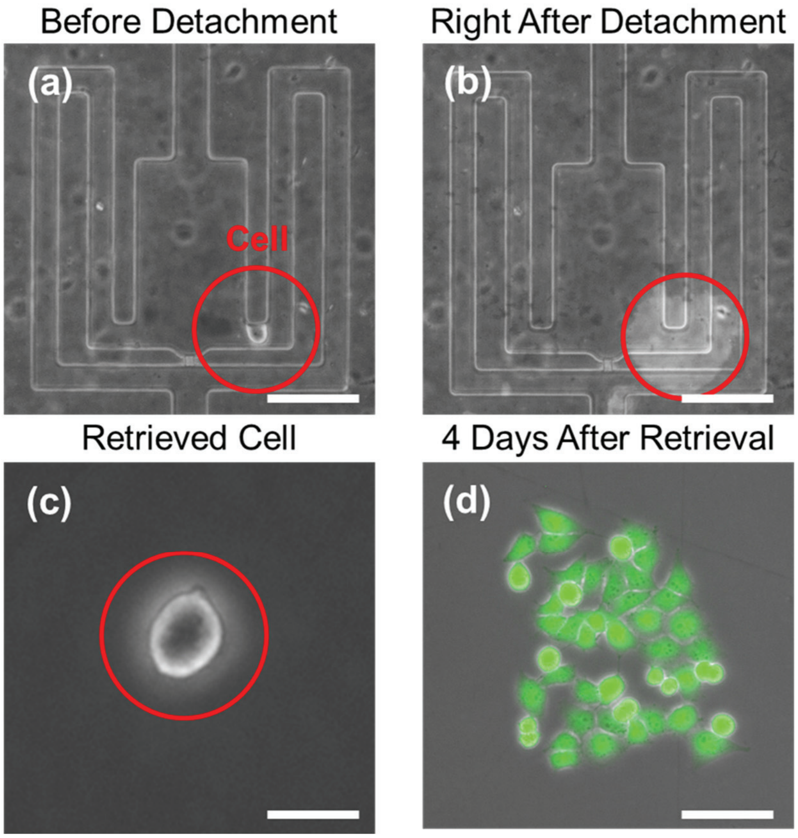

Fig. 7-9. The recovery of a MDA-MB-231 cell after laser detachment: (A) before detachment, (B) after detachment, (C) retrieved in the 96-well plate, and (D) 4 days recovery showing healthy proliferation.

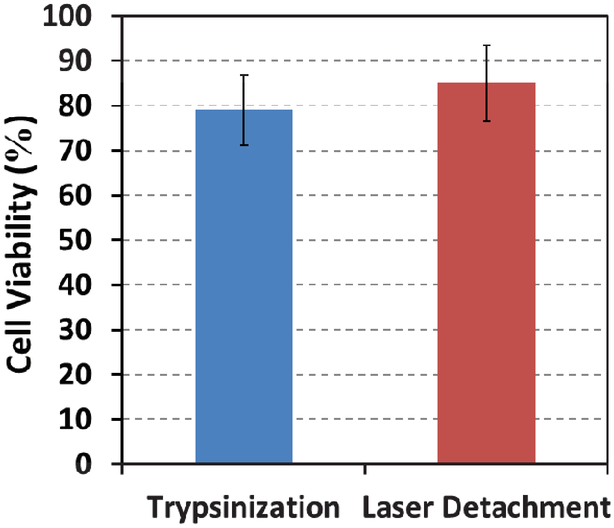

Fig. 7-10. Cell viability of MDA-MD-231 cells 4 days after the detachment by laser (the presented scheme) and by trypsin (the conventional scheme), respectively. Laser detachment shows better viability.

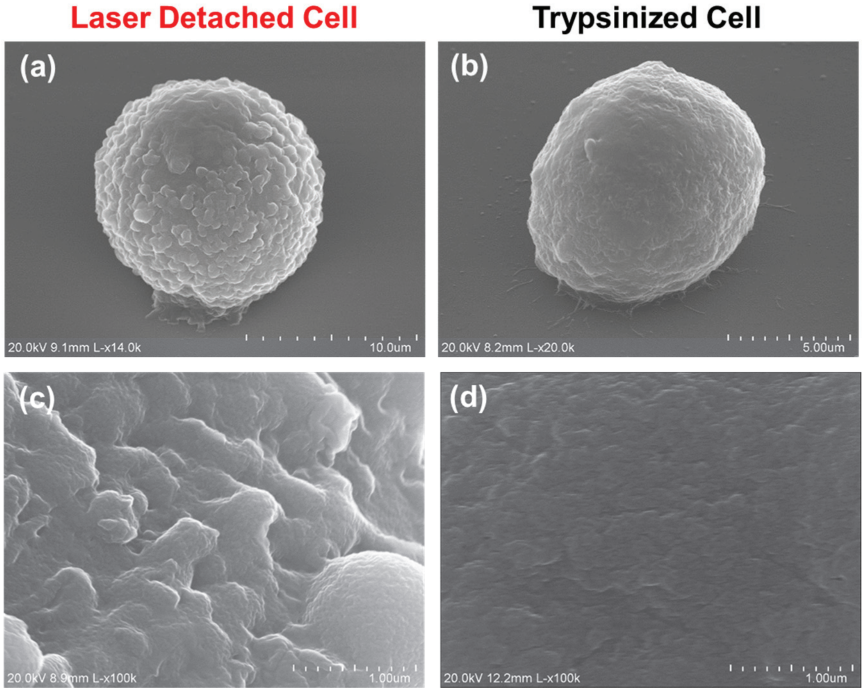

Fig. 7-11. The scanning electron microscope (SEM) of laser detached and trypsinized cell: (A) a laser detached MDA-MB-231 cell, (B) a trypsinized MDA-MB-231 cell, (C) Enlarged view of a laser detached MDA-MB-231 cell, and (D) Enlarged view of a trypsinized MDA-MB-231 cell.

7.5 Single Cell Gene Expression

Although we demonstrated good cell viability and surface protein preservation, laser detachment may induce a cellular stress response that alters gene expression [18]. We characterized the mRNA expression of 96 genes comparing 20 laser detached and 20 trypsinized cells. Fig. 7-12 is the principle component analysis (PCA) plot showing the characteristics of each single cell as a dot. The cells detached by different methods are marked by different colors (trypsizined cells are green, while laser detached ones are red). In the plot, the two populations mix together, meaning that no distinguishing feature can be found that separates the two populations. The Hierarchical Clustering (HC) plot (Fig. 7-13) groups cells with similar expression together like a family tree. Again, the two populations are mixed in the center, showing that the heterogeneity within group is larger than the difference between two detachment methods. Fig. 7-14 is the violin plot of the trypsinized cells and the laser detached cells. The cells detached by both methods maintain typical T47D cell expression such as high EPCAM and low Vimentin, and no significant difference was found.

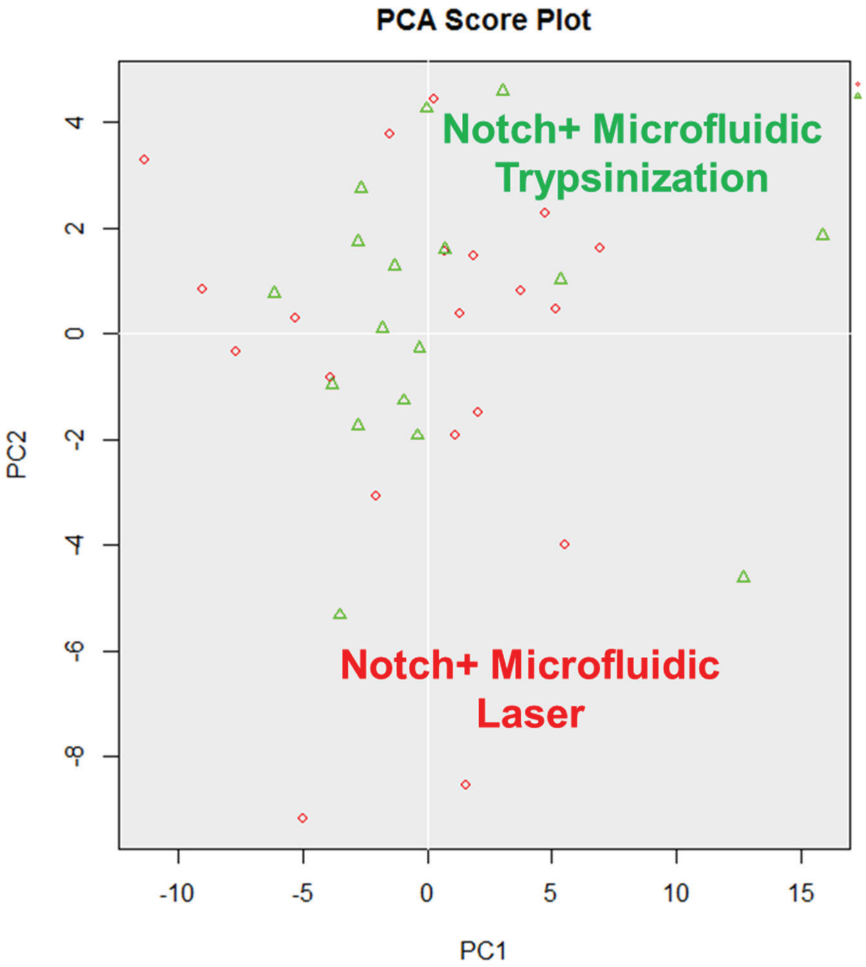

Fig. 7-12. The Principal component analysis (PCA) plot of trypsinized (green) cells and the laser detached (red) cells. The cells in both populations mix in the plot, meaning no significant difference in gene expression by two detachment methods.

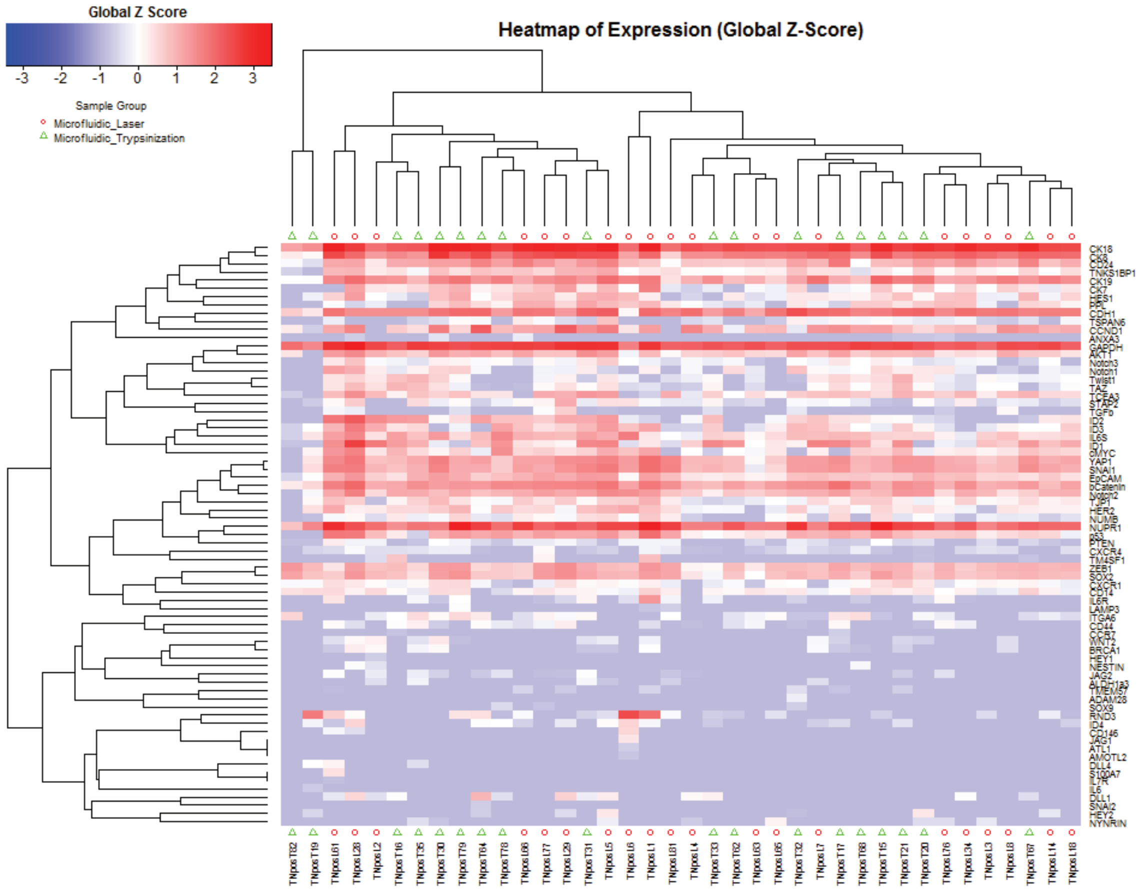

Fig. 7-13. The Hierarchical Clustering (HC) plot of trypsinized (green) cells and the laser detached (red) cells. The cells detached by both methods mix in the plot, meaning no significant difference was observed by two detachment methods.

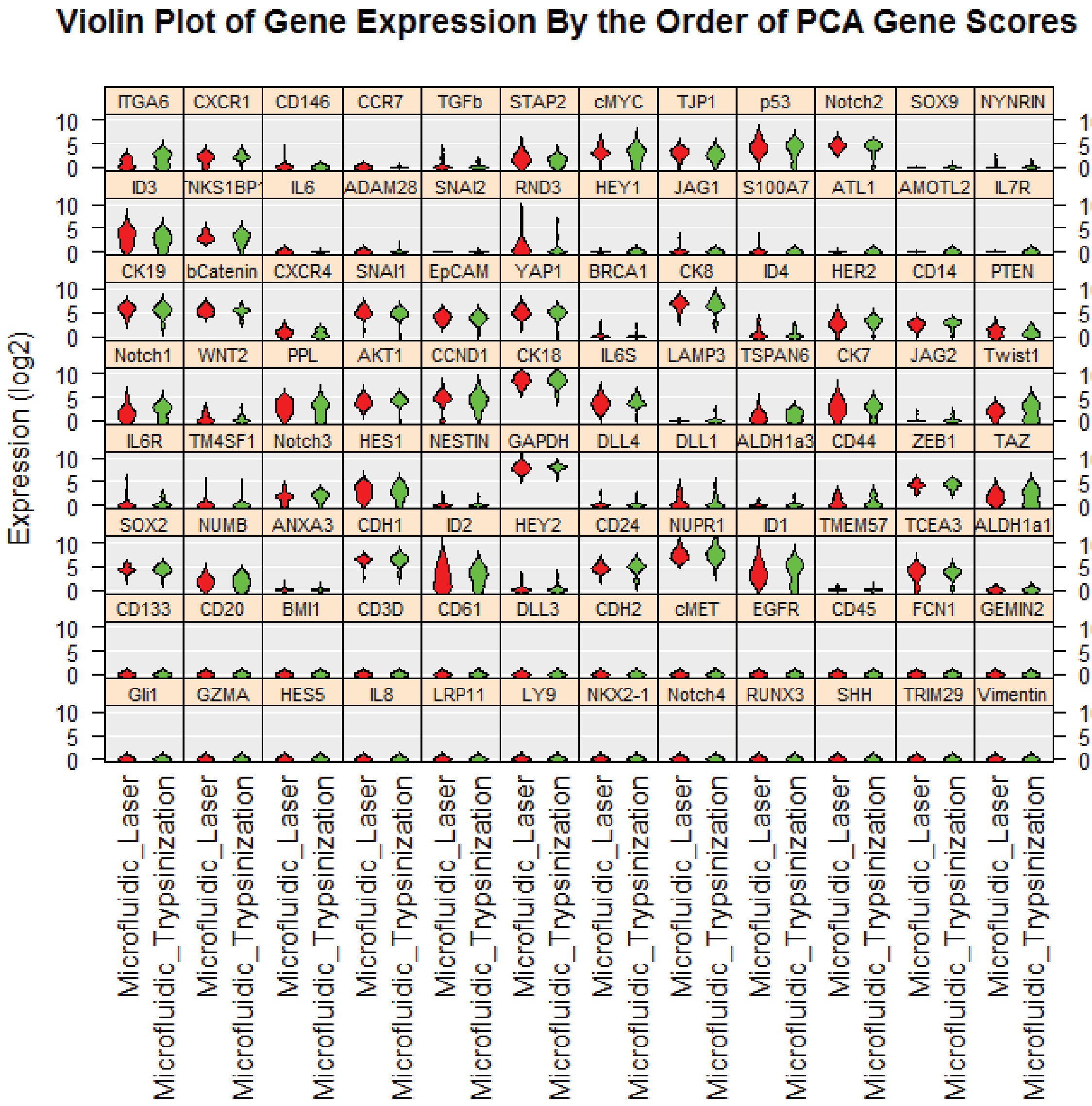

Fig. 7-14. The violin plot of trypsinized (green) cells and the laser detached (red) cells. 96 genes expression of each single cell was analyzed. The y-axis is the relative expression, and the x-axis is the distribution of the population. The cells detached by both methods maintain typical T47D cell expression, and no significance was found.

7.6 Chapter Summary

Combining our single cell capture scheme and cell detachment and retrieval capabilities, we can monitor the development of a colony formed by single cells and then retrieve specific cells with interesting morphologies within a colony for further analysis. This capability open new possibilities in the study of cancer cell heterogeneity during tumor development. As a proof of concept, we harvested two asymmetrically divided daughter cells from the same progenitor cell. The presented method can maintain good cell viability and preserve the membrane proteins after detachment. In addition, the gene expression will not be altered in this process as compared to trypsinization. These preliminary data prove that the presented cell retrieval method is suitable for the applications needing further off chip cell culture or mRNA expression analysis. Such techniques will be invaluable in studies of highly heterogeneous cancer cell populations.

Chapter 8
CONCLUSION AND FUTURE WORKS

This thesis presented several microfluidic platforms for the study of cancer metastasis on chip and a selective single cell retrieval tool for the genotypic and phenotypic analysis of cell heterogeneity. This chapter summarizes the works that has already been completed and discusses the possible improvements and applications in the future.

8.1 Conclusion

The accomplishments of this thesis focus on single cell microfluidic platforms for emulating three main stages of cancer metastasis and a selective single cell retrieval tool based on a photo-acoustic release mechanism. First, a single cell migration chip, which positions single cells at the long capillary channels and provides a stable chemical gradient to induce cell migration was developed. The chip is designed to study cancer metastasis by measuring the motility and chemo-attraction of cells at a single cell resolution. We can screen for drugs (or reagents) that inhibit metastasis, and identify biological signals that attract the cells. In addition to the migration assays, the platform also provides a method for motility based cell behavioral sorting. Highly motile and non-motile cells can be selectively retrieved from either side of the capillary channels after a migration assay. The retrieval process was show to have no effect on cell viability and was shown to enable downstream analysis. The preliminary results show that the demonstrated characteristics of sorted cells are maintained after retrieval and further culture, allowing for further downstream studies in the difference between highly motile and non-motile cells.

Second, I designed a single cell suspension culture chip, which can capture a total of 1,024 cells in a microwell array at single cell resolution and provide a suspension cell culture environment using a polyHEMA surface coating to prevent cell adhesion. Using the platform, the cells are individually separated into each chamber; this will not only prevent uncontrolled cell aggregation, but also, enable tracking of individual cell behavior within heterogeneous populations. Although polyHEMA has been used for suspension cell culture in petri dishes, the conventional polyHEMA coating technique provides poor uniformity due to using an uncontrolled evaporation process. Spin-coating is a well-defined process and is widely used in microfabrication. Here, it was used as a polyHEMA coating technique to provide greater control of spreading and evaporation. Even though pinholes and trapped bubbles are generated during spin-coating, these defects can be removed by double spin-coating and including a high temperature reflow of the deposited polyHEMA as the final step. With the optimized coating protocol, the surface roughness can be reduced to 0.2 μm, which is only 6% of the roughness introduced in the conventional coating process. This greater uniformity facilitates successful integration with our microfluidics. Integrating the single cell device with the polyHEMA substrate, we demonstrated different anoikic behaviors between stem-like and non-stem-like SKOV3 ovarian cancer cells. In addition, the integrated platform allowed for single-cell-derived sphere formation assays. The platform provides a continuous perfusion of media from gravity flow to improve the reliability and throughput for long-term culture. We successfully performed single-cell-derived sphere assays of patient derived xenograft (PDX) cells and breast cancer cell lines including SUM159, MDA-MB-231, and MCF-7 and T47D cells.

To facilitate investigation of cell-cell interactions at a single cell level, I developed a ratio controlled cell-cell interaction chip, specializing in controlling the number of interacting cells and microenvironment using a novel actuation method. Electrolytic bubbles are generated to block flow and isolate the microwells without using any valves or external pneumatic pumps. In addition, another platform was designed in which actuation-free isolation was implemented using two-phase immiscible flows while providing continuous renewal of media through a semi-permeable membrane for long-term co-culture. Furthermore, I implemented a dual adherent-suspension co-culture device, which can provide both a suspension environment for cancer cells and adherent culture for stromal cells in close proximity by selectively patterning polyHEMA in indented micro-wells. Using this platform, up to 70% of the loaded cell can be captured for small sample sizes (50 cells), enabling the analysis of rare cell populations such as primary cells or CTC.

In addition to the microfluidic platforms, I developed a selective single cell retrieval tool, which can retrieve interesting single cells from the microfluidics for further analysis. Cells are cultured on a CNT-PDMS composite film, which can be deformed using pulsed laser exposure. Due to the rapid (in milliseconds) deformation, cells can be detached in a non-thermal manner and then retrieved by precise flow control. Combining our single cell capture scheme, cell detachment, and retrieval capabilities, we can monitor the development of a colony formed by single cells and then retrieve specific cells with interesting morphologies or other characteristics within a colony for further analysis. These capabilities can enable new studies of cancer cell heterogeneity that were not previously possible with conventional FACS sorting techniques. We demonstrated that the presented method has a negligible effect on cell viability and preserves the membrane proteins after detachment. In addition, gene expression of laser detached cells is similar to the cells detached by trypsinization, indicating little expression alteration caused by laser detachment. These preliminary data prove that the presented cell retrieval method is suitable for applications where further off chip cell culture or mRNA expression analysis is desirable.

8.2 Future Works

8.2.1 Study the self-renewal and differentiation of cancer stem cell

To expand on the use of our single cell retrieval tool, we would like to study the regulation of the differentiation and self-renewal of cancer stem-like cells (CSCs), which are known to be tumorigenic. The regulation of differentiation and self-renewal is an interesting fundamental science question, and skewing CSC towards differentiation could be a promising therapeutic opportunity. Conventional FACS sorting machines can only separate CSC and non-CSC, without visualizing the cell division process, and thus, FACS lacks the capability to distinguish the CSC that gives rise to non-CSC (differentiation) and the CSC that gives rise to only CSC (self-renewal). Combining the microfluidic single cell capture scheme and the cell retrieval capability, we can decipher CSC differentiation or self-renewal regulation pathways. The single CSC can be loaded and monitored in the micro-chamber, and after proliferation, the two daughter cells (of either symmetric or asymmetric division) can be retrieved for off-chip analysis. Then, the difference between the differentiating CSC and self-renewing CSC can be compared via genomic analysis.

8.2.2 Use primary cancer cells in the microfluidics

Although I have successfully developed microfluidics tools for the on-chip emulation of cancer metastasis, the use of primary cells from patient has not yet been fully explored. We have preliminary success in growing spheres from single patient derived xenograft (PDX) cells in the single cell suspension culture chip, and similar approaches can be applied to the newly developed dual adhesion-suspension cell-cell interaction platform, targeting the cell-cell interactions between primary cancer cells and fibroblast cells. It is believed that cancer cells can influence the surrounding fibroblast cells, creating tumor associated fibroblast that provide a favorable environments for cancer development, drug resistance, and metastasis. After co-culture, we can exam the sphere formation results and then study the molecular signature of single cells, as we did in the Chapter 3, to understand the effect of the fibroblasts on the cancer cells. In addition, we can also retrieve the fibroblast cells to compare their expression to bulk primary fibroblasts. Although more challenging, the use of primary samples can greatly increase the impact of in-vitro microfluidic work and better recapitulate in-vivo biology on-chip.

8.2.3 Small sample preparation by microfluidics

Although we can manipulate single cells in microfluidics, the sample preparation and interfacing of these microfluidic approaches and conventional bulk analysis machines is challenging. As the bulk tools typically use large volumes (mL), while microfluidic tools prefer to handle small volumes (µL – nL), the dead volume lost during interfacing and centrifugation can be significant. As an example, when using circulating tumor cells (CTCs), which have great potential for diagnostics and personalized medicine, it is typical to have less than 10 cells per mL of patient blood. Using conventional dish based approaches such as western blot and qRT-PCR, tens of cell cannot be used to generate meaningful data in the assays, because the large volume dilutes the concentration of proteins and mRNA of the cells. Even though microfluidics can analyze smaller number or even single cells, the volume (mL) of the CTC samples is too large to be loaded in most microfluidic platforms. For example, the C1™ Single-Cell Auto Prep System (Fluidigm can only load 3μL into its microfluidic chip. Given a cell concentration of 10 cells per mL, almost no cell can be loaded for analysis of CTC. Centrifuge can help increasing the cell density, but the majority of cells will be lost in centrifuging process for three reasons: (1) reducing the volume from mL to μL is fundamentally challenging, (2) when the number of cells is really small (10-50 cells), cells cannot aggregate well into a pellet, and (3) fragile primary samples cannot endure high centrifuging force (typically should be lower than 100 – 300 relative centrifugal force (RCF)). Thus, we are working on implementing a microfluidic cell condenser interface stage, which can enrich low density cell solutions to minimize the interface loss. Such advances in small sample preparation are promising both for research and commercialization applications.

8.2.4 Cell sorter based on behavior

Cell heterogeneity is known to be a critical issue in cancer research, but conventionally, cell heterogeneity studies have been performed mostly using cell markers to distinguish cells. Cell surface markers cannot fully represent the properties and behaviors of a cell, but FACS and MACS sorting are the only reliable methods to provide high throughput (~million cells per hour) cell characterization for cell heterogeneity studies.

In this thesis, we demonstrated the capability to separate cells based on different motility, and the laser-based cell retrieval tool is a more general approach for retrieving single cells based on their morphologies. The sorted cells were proved to have different mRNA expressions and behaviors, verifying the feasibility of sorting cells by behavior rather than markers. However, low throughput (less than 100 cells can be retrieved per hour) hinders the use of these approaches on a large scale or as a replacement for FACS and MACS. Moving toward the behavior-based cell sorter, we should improve the throughput by implementing high-throughput imaging capabilities, fully automatic software analysis, and robotic automation of liquid handling. Though throughput of behavior based sorted will be still significantly lower than that of the conventional FACS sorter, the ability of our platforms to handle small samples with high efficiency will alleviate the need for high-throughput. Combining behavior based cell sorter and the capability of analyzing small samples can change the paradigm of cell heterogeneity studies.

BIBLIOGRAPY

Chapter 1

1. Hanahan D, Weinberg RA, *Cell,* 2011, 144, 646-674.
2. Steeg SP, *Nature Rev. Cancer*, 2006, 12, 895-904.
3. Bissell JM and Hines CW, *Nature Medicine*, 2011, 17, 320-329.
4. Siegel, Rebecca, Naishadham, Deepa, Jemal, Ahmedin, *CA: A Cancer Journal for Clinicians*, 2012, 62, 1, 10-29.
5. Sethi N and Kang Y, *Nat Rev Cancer*., 2011, 11, 735-748.
6. Steeg PS. *Nat Rev Cancer*., 2003, 3, 55-63.
7. Corbin E. Meacham and Sean J. Morrison, 2013, *Nature*, 501, 328–337.
8. Rodriguez LG, Wu X, Guan JL. *Methods Mol Biol*., 2005, 294, 23-9.
9. Chen HC, *Methods Mol Biol*., 2005, 294, 15-22.
10. A.Y. Hsiao, Y. Torisawaa, Y. Tung, S. Sud, R. S. Taichman, K. J. Pienta, , S. Takayama, *Biomaterials*, 2009, 30, 3020-7.
11. M. Bauer, G. Su, D. J. Beebe, A. Friedl, *Integr Biol.* , 2010, 2, 371-8.
12. Y. Gao, D. Majumdar, B. Jovanovic, C. Shaifer, P. C. Lin. A. Zijlstra, D. J. Webb and D. Li, *Biomed Microdevices*, 13, 539-48, 2011.
13. D. Majumdar, Y. Gao, D. Li, and D. J. Webb, *J Neurosci Methods*, 196, 38-44, 2011.
14. M. Heneweer, M. Muusse, M. Dingemans, P. C. de Jong, M. van den Berg, J. T. Sanderson, *Toxicol Sci*., 2005, 83, 257-63.
15. J. Park, H. Koito, J. Li, A. Han, *Biomed Microdevices*, 2009, 11, 1145-53.
16. H. Ma, T. Liu, J. Qin, B. Lin, *Electrophoresis*, 2010, 31, 1599-605.
17. Elliot E. Hui, *Proc. Natl. Acad. Sci. U. S. A*, 2007, 104, 5722–5726.
18. I. K. Zervantonakis, S. K. Hughes-Alford, J. L. Charest, J. S. Condeelis, F. B. Gertler and R. D. Kamm, *Proc. Natl. Acad. Sci. U. S. A*., 2012, 109, 13515–20.
19. J. Pan, A. L. Stephenson, E. Kazamia, W. T. S. Huck, J. S. Dennis, A. G. Smith and C. Abell, *Integr. Biol*., 2011, 3, 1043–1051.
20. T. P. Lagus and J. F. Edd, *RSC Adv*, 2013, 3, 20512.
21. A. Huebner, D. Bratton, G. Whyte, M. Yang, A. J. deMello, C. Abell and F. Hollfelder, *Lab Chip*, 2009, 9, 692–698.
22. S.M. Frisch, R.A. Screaton, *Curr Opin Cell Biol*, 2001 13, 555-562.
23. W.-H. Tan and S. Takeuchi, *Proc Natl Acad Sci U S A*, 2007, 104(4), 1146–1151.
24. J. Chung, Y. J. Kim and E. Yoon, *Appl. Phys. Lett*, 2011, 12, 3701-3703.
25. Alison M Skelley, Oktay Kirak, Heikyung Suh, Rudolf Jaenisch and Joel Voldman., *Nature Methods*, 2009, 6, 147 – 152.
26. John A. Baron, *Nature Review Cancer*, 12, 368-371, 2012.
27. Virginie Clement, Valerie Dutoit, Denis Marino, Pierre-Yves Dietrich and Ivan Radovanovic, *Int. J. Cancer*: 125, 244–248, 2009.

28. Cristina Richichi, Paola Brescia, Valeria Alberizzi, Lorenzo Fornasari, and Giuliana Pelicci, *Neoplasia*. Jul 2013; 15(7): 840–847.
29. Yamada H, Maruo R, Watanabe M, Hidaka Y, Iwatani Y, Takano T. *Cytometry A*. 2010, 77(11):1032-7.
30. Lili C. Kudo, Nancy Vi, Zhongcai Ma, Tony Fields, Nuraly K. Avliyakulov, Michael J. Haykinson, Anatol Bragin, Stanislav L. Karsten, *PlosOne*, 7, 7, e41564, 2012.
31. Orane Guillaume-Gentil, Tomaso Zambelli and Julia A. Vorholt, *Lab Chip*, 14, 402-414, 2014.
32. Kimio S, Kyoko K, Toshiyuki T, et al., *Proceedings of MicroTAS*, 2013 100-102.
33. Sada T, Fujigaya T, Niidome Y, Nakazawa K, Nakashima N, *ACS Nano*., 2011, 5(6):4414-21.
34. Baac H-W, Ok J-G, Maxwell A, Lee K-T, Chen Y-C et al., *Sci. Rep*., 2012, 2, 989.

Chapter 2

1. Hanahan D, Weinberg RA, *Cell,* 2011, 144, 646-674.
2. Steeg SP, *Nature Rev. Cancer,* 2006, 12, 895-904.
3. Bissell JM and Hines CW, *Nature Medicine*, 2011, 17, 320-329.
4. Yoshida AB. Sokoloff MM, Welch RD and Rinker-Schaeffer WC, *J Natl Cancer Inst.,* 2000, 92, 1717-1730.
5. Gobeil S, Zhu X, Doillon CJ, Green MR,*Genes Dev.,* 2008*,* 22, 2932-2940.
6. Shoushtari NA, Szmulewitz ZR and Rinker-Schaeffer WC, *Nat Rev Clin Oncol.,* 2011*,* 8, 333-342.
7. Sethi N and Kang Y, *Nat Rev Cancer.,* 2011*,* 11, 735-748.
8. Steeg PS. *Nat Rev Cancer.,* 2003*,* 3, 55-63.
9. Nathanson SD,*Cancer*, 2003, 98, 413–423.
10. Rodriguez LG, Wu X, Guan JL. *Methods Mol Biol*., 2005, 294, 23-9.
11. Chen HC, *Methods Mol Biol*., 2005, 294, 15-22.
12. Xie Y, Zhang W, Wang L, Sun K, Sun Y, Jiang X, *Lab Chip*., 2011, 11, 2819-2822.
13. Irimia D, Charras G, Agrawal N, Mitchison T, Toner M, *Lab Chip*., 2007, 7, 1783-1790.
14. Shin MK, Kim SK, Jung H, *Lab Chip*., 2011, 11, 3880-3887
15. Irimia D, Toner M, *Integr Biol (Camb)*. 2009, 1, 506-512.
16. Mak M, Reinhart-King CA, Erickson D, *PLoS One*., 2011, 6, 20825.
17. Gallego-Perez D, Higuita-Castro N, Denning L, DeJesus J, Dahl K, Sarkar A, Hansford DJ, *Lab Chip*, 2012, 12, 4424-32.
18. Ko Y-G, Carlos C-C and Ho C-C, *Soft Matter*., 2013, 9, 2467-2474
19. Chung S, Sudo R, Mack PJ, Wan CR, Vickerman V, Kamm RD, *Lab Chip*. 2009, 9, 269-275.
20. De Cock LJ, De Wever O, Hammad H, Lambrecht BN, Vanderleyden E, Dubruel P, De Vos F, Vervaet C, Remon JP, De Geest BG, *Chem Commun (Camb)*., 2012, 48, 3512-3514.
21. Chaw KC, Manimaran M, Tay EH, Swaminathan S, *Lab Chip*. 2007, 7, 1041-1047.
22. Kaji H, Yokoi T, Kawashima T, Nishizawa M, *Lab Chip*., 2009, 9, 427-432.
23. Altschuler SJ, Wu LF, *Cell*, 2010, 141, 559-563.
24. Negrini S, Gorgoulis VG, Halazonetis TD, *Nat Rev Mol Cell Biol.,* 2010, 11, 220-228.

25. Magee JA, Piskounova E, Morrison SJ,Cancer, *Cell*, 2012, 21, 283-296.
26. Charafe-Jauffret E, Ginestier C, Iovino F, Tarpin C, Diebel M, Esterni B, Houvenaeghel G, Extra JM, Bertucci F, Jacquemier J, Xerri L, Dontu G, Stassi G, Xiao Y, Barsky SH, Birnbaum D, Viens P, Wicha MS, *Clin Cancer Res*., 2012, 16, 45-55.
27. Visvader JE, Lindeman GJ, *Nat Rev Cancer*., 2008, 8, 755-768.
28. Yang J, Weinberg RA, *Dev Cell*., 2008, 14, 818-29.
29. Kalluri R, Weinberg RA, *J Clin Invest.,* 2009. 119, 1420-1428.
30. Nieto MA, *Annu Rev Cell Dev Biol*., 2011, 27, 347-376.
31. Voulgari A, Pintzas A, *Biochim Biophys Acta*., 2009, 1796, 75-90.
32. Cieply B, Riley P, Pifer PM, Widmeyer J, Addison JB, Ivanov AV, Denvir J, Frisch SM, *Cancer Res*., 2012, 72, 2440-53.
33. Frimat JP, Becker M, Chiang YY, Marggraf U, Janasek D, Hengstler JG, Franzke J, West J, *Lab Chip*., 2011, 11, 231-237.
34. Y.-C. Chen, X. Lou, P. Ingram, and E. Yoon, *Proceeding of MicroTAS*, 2011, 1409-1411.
35. Joyce JA, Pollard JW, *Nat Rev Cancer*., 2009, 9, 239-52.
36. Walker GM, Sai J, Richmond A, Stremler M, Chung CY, Wikswo JP, *Lab Chip.* 2005, 5, 611-618.
37. Shi CL, Yu CH, Zhang Y, Zhao D, Chang XH, Wang WH,*Asian Pac J Cancer Prev*. 2011, 12, 555-9.
38. Green CE, Liu T, Montel V, Hsiao G, Lester RD, Subramaniam S, Gonias SL, Klemke RL, *PLoS One*., 2009, 4, 21.
39. Craig MJ, Loberg RD, *Cancer Metastasis Rev*., 2006, 25, 611-9.
40. Kakinuma T, Hwang ST, *J Leukoc Biol*., 2006, 79, 639-51.
41. Koizumi K, Hojo S, Akashi T, Ysumoto K, Saiki I, *Cancer Sci.,* 2007, 98, 1652-8.
42. Scarpino S, Stoppacciaro A, Colarossi C, Cancellario F, Marzullo A, Marchesi M, Biffoni M, Comoglio PM, Prat M, Rucor LP, *J Pathol., 1999,* 189, 570-5.
43. Wei W, Kong B, Yang Q, Qu X, *Cancer Biol Ther., 2010,* 9, 79-87.
44. Zhong SQ, Xu YD, Zhang YF, Hai LS and Tang FC, *World J Gastroenterol*, 1998, 4, 550-552.
45. Rosenthal DT, Iyer H, Escudero S, Bao L, Wu Z, Ventura AC, Kleer CG, Arruda EM, Garikipati K, Merajver SD,*Cancer Res.*, 2011, 71, 6338-6349.
46. Jane L, Tracey AM and Wen GJ, *Current Signal Transduction Therapy*, 2011, 6,173-179.

Chapter 3

1. Patricia S.S. *Nature Rev. Cancer*, 2006, 12, 895-904.
2. Bissell J.M. and Hines C.W. *Nature Medicine*, 2011, 17, 320-329.
3. Sethi N. and Kang Y. *Lab Chip*, 2011, 11(22), 3880-3887.
4. Irimia D., Charras G., Agrawal N., Mitchison T., Toner M. *Lab Chip*., 2007, 7(12), 1783-1790.
5. Mehlen P., Puisieux A. *Nat Rev Cancer*., 2006, 6(6), 449-458.
6. Kim Y.N., Koo K.H., Sung J.Y., Yun U.J., Kim H. *Int J Cell Biol*. 2012, 306879.
7. Yoon H.J., Kim T.H., Zhang Z., Azizi E., Pham T.M., Paoletti C., Lin J., Ramnath N., Wicha M.S., Hayes D.F., Simeone D.M., Nagrath S. *Nat Nanotechnol*. 2013, 8(10),

735-41.
8. Wei L., Yang Y., Yu Q. *Cancer Res*. 2001, 61(6), 2439-2444.
9. Singh A.B., Sugimoto K. and Harris C.R. *The Journal of Biological Chemistry*, 2007, 282, 32890-32901.
10. Negrini S., Gorgoulis V.G., Halazonetis T.D. *Nat Rev Mol Cell Biol*. 2010, 11(3), 220-228.
11. Magee J.A., Piskounova E., Morrison S.J. *Cancer Cell*, 2012, 21(3), 283-296.
12. Al-Hajj M., Wicha M.S., Benito-Hernandez A., Morrison S.J., Clarke M.F., *Proc. Natl. Acad. Sci. USA*, 2003, 100, 3983-3988.
13. O'Brien C.A., Pollett A., Gallinger S., Dick J.E. *Nature*, 2007, 445, 106-110.
14. Prince M.E., Sivanandan R. Kaczorowski A., Wolf G.T., Kaplan M.J., Dalerba P., Weissman I.L., Clarke M.F., Ailles L.E., *Proc. Natl. Acad. Sci. USA*., 2007, 104, 973-978.
15. McDermott S.P., Wicha M.S. *Mol Oncol*. 2010, 4(5), 404-19.
16. Zhou B.B., Zhang H., Damelin M., Geles K.G., Grindley J.C., Dirks P.B. *Nat Rev Drug Discov*., 2009, 8(10), 806-823.
17. Visvader J.E., Lindeman G.J. *Nat Rev Cancer*. 2008, 8(10), 755-768.
18. Dontu G., Abdallah W.M., Foley J.M., Jackson K.W., Clarke M.F., Kawamura M.J., Wicha M.S. *Genes Dev*., 2003, 17(10), 1253-1270.
19. Hsiao A.Y., Tung Y.C., Kuo C.H., Mosadegh B., Bedenis R., Pienta K.J., Takayama S. *Biomed Microdevices*, 2012, 14(2), 313-323.
20. Friedrich J., Seidel C., Ebner R., Kunz-Schughart L.A. *Nat Protoc*. 2009, 4(3), 309-324.
21. Lee W.G., Ortmann D., Hancock M.J., Bae H., Khademhosseini A. *Tissue Eng Part C Methods*, 2010, 16(2), 249-259.
22. Ota H., Kodama T., Miki N. *Biomicrofluidics*., 2011, 3, 34105-34115.
23. Huebner A., Bratton D., Whyte G., Yang M., Demello A.J., Abell C., Hollfelder F. *Lab Chip*. 2009, 9(5), 692-8.
24. Ingram P., Im M., McDermott S., Wicha M.S., Yoon E. *Proceeding of MicroTAS,* 2011, 1539-1541.
25. Chung J., Kim Y.J., Yoon E. *Appl Phys Lett*., 2011, 98(12), 123701.
26. Markovitz-Bishitz Y., Tauber Y., Afrimzon E., Zurgil N., Sobolev M., Shafran Y., Deutsch A., Howitz S., Deutsch M. *Biomaterials*, 2011, 31(32), 8436-8444.
27. Rago A.P., Napolitano A.P., Dean D.M., Chai P.R., Morgan J.R. *Cytotechnology*, 2008, 56(2), 81-90.
28. Re F., Zanetti A., Sironi M., Polentarutti N., Lanfrancone L., Dejana E., Colotta F. *J Cell Biol*. 1994, 127(2), 537-46.
29. Minett T.W., Tighe B.J., Lydon M.J., Rees D.A. *Cell Biol Int Rep*., 1984, 8(2), 151-159.
30. Yamada K.M., Geiger B. *Curr Opin Cell Biol*., 1997, 9(1), 76-85.
31. Gupta P.B., Chaffer C.L., Weinberg R.A. *Nat Med*., 2009, 15(9), 1010-1012.
32. Ginestier C., Hur M.H., Charafe-Jauffret E., Monville F., Dutcher J., Brown M., Jacquemier J., Viens P., Kleer C.G., Liu S., Schott A., Hayes D., Birnbaum D., Wicha M.S., Dontu G. *Cell Stem Cell*. 2007, 1(5), 555-567.
33. Silva I.A., Bai S., McLean K., Yang K., Griffith K., Thomas D., Ginestier C., Johnston C., Kueck A., Reynolds R.K., Wicha M.S., Buckanovich R.J. *Cancer Res*., 2011,

71(11), 3991-4001.
34. Nieto M.A. *Annu Rev Cell Dev Biol*. 27, 347-376 (2011).
35. Watanabe S., Kishimoto T., Yokosuka O. *Pancreas*, 2011, 40(4), 608-614.
36. Zeng Q., Chen S., You Z., Yang F., Carey T.E., Saims D., Wang C.Y. B. *J Biol Chem.* 2002, 277(28), 25203-8.
37. Dontu G., Jackson K.W., McNicholas E., Kawamura M.J., Abdallah W.M., Wicha M.S. *Breast Cancer Res*., 2004, 6, 605-615.
38. Creighton C.J., Li X., Landis M., Dixon J.M., Neumeister V.M., Sjolund A., Rimm D.L., Wong H., Rodriguez A., Herschkowitz J.I., Fan C., Zhang X., He X., Pavlick A., Gutierrez M.C., Renshaw L., Larionov A.A., Faratian D., Hilsenbeck S.G., Perou C.M., Lewis M.T., Rosen J.M., Chang J.C. *Proc. Natl. Acad. Sci. USA*, 2009, 106, 13820-13825.
39. Grudzien P., Lo S., Albain K.S., Robinson P., Rajan P., Strack P.R., Golde T.E., Miele L. and Foreman K.E. *Anticancer Research*, 2010, 30, 3853-3868.
40. Cao L., Zhou Y., Zhai B., Liao J., Xu W., Zhang R., Li J., Zhang Y., Chen L., Qian H., Wu M. and Yin Z. BMC *Gastroenterology*, 2011, 11,71.

Chapter 4

1. K. Polyak, I. Haviv, I.G. Campbell, *Trends Genet*, 2009 25(1), 30-8
2. R. Peerani and P. W. Zandstra, *J. Clin. Invest*, 2010, 120, 60–70.
3. D. Hanahan, R. A. Weinberg. *Cell*, 2011, 144(5), 646-74
4. R. R. Langley, I. J. Fidler, *J Cancer*, 2011, 128(11), 2527-35.
5. I. J. Fidler, *Nat Rev Cancer*, 2003, 3(6), 453-8.
6. S. Liu, C. Ginestier, S. J. Ou, S. G. Clouthier, S. H. Patel, F. Monville, H. Korkaya, A. Heath, J. Dutcher, C. G. Kleer, Y. Jung, G. Dontu, R. Taichman, M. S. Wicha., *Cancer Res*. 2011, 71(2), 614-24.
7. G. Solinas, G. Germano, A. Mantovani, P. Allavena., *J Leukoc Biol*., 2009, 86(5), 1065-73.
8. J. G. Quatromoni, E. Eruslanov, *Am J Transl Res*., 2012, 4(4), 376-89.
9. J. Lu, X. Ye, F. Fan, L. Xia, R. Bhattacharya, S. Bellister, F. Tozzi, E. Sceusi, Y. Zhou, I. Tachibana, D. M. Maru, D. H. Hawke, J. Rak, S. A. Mani, P. Zweidler-McKay, L. M. Ellis, *Cancer Cell*, 2013, 23(2), 171-85.
10. J. W. Franses, A. B. Baker, V. C. Chitalia, E. R. Edelman, *Sci Transl Med*., 2011, 3(66), 66.
11. Y, Luo, H, Zhou, J, Krueger, C, Kaplan, S, H, Lee, C, Dolman, D, Markowitz, W, Wu, C, Liu, R, A, Reisfeld, R, Xiang. *J Clin Invest*., 2006, 116(8), 2132-2141.
12. Y. Miki, K. Ono, S. Hata, T. Suzuki, H. Kumamoto, H. Sasano, *J Steroid Biochem Mol Biol*., 2012, 131(3-5), 68-75.
13. M. Cristofanilli, G. T. Budd, M. J. Ellis, A. Stopeck, J. Matera, M. C. Miller, J. M. Reuben, G. V. Doyle, W. J. Allard, L. W. Terstappen, D. F. Hayes, *N Engl J Med*., 2004, 351(8), 781-91.
14. S.S. Patricia, *Nature Rev. Cancer*, 2006, 12, 895-904.
15. J.B. Mina and C.H. William, *Nature Medicine*, 2011, 17, 320-329.
16. P. Mignatti, T. Morimoto, D.B. Rifkin, *Proc Natl Acad Sci U S A*, 1991, 15, 88(24), 11007-11.
17. M. Heneweer, M. Muusse, M. Dingemans, P. C. de Jong, M. van den Berg, J. T.

Sanderson, *Toxicol Sci*., 2005, 83(2), 257-63.
18. A.Y. Hsiao, Y.S. Torisawa, Y.C. Tung, S. Sud, R.S. Taichman, K. J. Pienta, S. Takayama, *Biomaterials*, 2009, 30(16), 3020-7.
19. J. Park, H. Koito, J. Li, A. Han, *Biomed Microdevices*, 2009, 11(6), 1145-53.
20. M. Bauer, G. Su, D. J. Beebe, A. Friedl, *Integr Biol*., 2010, 2(7-8):371-8.
21. H. Ma, T. Liu, J. Qin, B. Lin, *Electrophoresis*, 2010, 31(10), 1599-605.
22. Y. Gao, D. Majumdar, B. Jovanovic, C. Shaifer, P. C. Lin, A. Zijlstra, D. J. Webb, D. Li, *Biomed Microdevices*, 2011;13(3):539-48.
23. D. Majumdar, Y. Gao, D. Li, D. J. Webb, *J Neurosci Methods*, 2011, 196(1), 38-44.
24. E. Tumarkin, L. Tzadu, and E. Kumacheva, *Integr. Biol*., 2011, 3, 653-662.
25. Y.-C. Chen, Y.-H. Cheng, H.S. Kim, P.N. Ingram, J.E. Nor and E. Yoon, *Lab Chip*, 2014, 14 (16), 2941 - 2947.
26. P. Ingram, Y. J. Kim, T. Bersano-Begey, X. Lou, A. Asakura, and E. Yoon, *Proceedings of MicroTAS*, Groningen, 2010, 277-279.
27. J. Frimat, M. Becker, Y. Chiang, and J. West, *Lab Chip*, 2011, 11, 231-237.
28. S. Hong, Q. Pan and L. P. Lee, *Integr. Biol*., 2012, 4, 374–80.
29. R. R. Stine, E. L. Matunis, *Trends in Cell Biology*, 2013, 23(8), 357-364.
30. P. M. Fordyce, Diaz-Botia CA, DeRisi JL, Gomez-Sjoberg R, *Lab Chip*, 2012, 12(21), 4287-95.
31. S. H. Chiu and C. H. Liu, Lab Chip, 2009, 9, 1524-1533.
32. D. R. Hofer, E. R. Sherwood, W. D. Bromberg, J. Mendelsohn, C. Lee, J. M. Kozlowski, *Cancer Res*., 1991, 51(11),2780-5.
33. C. Christov, F. Chrétien, R. Abou-Khalil, G. Bassez, G. Vallet, F. J. Authier, *Mol. Biol. Cell*, 2007, 18, 1397-1409.
34. W.-H. Tan and S. Takeuchi *Proc Natl Acad Sci U S A*, 2007, 104(4), 1146–1151.
35. J. Chung, Y. J. Kim and E. Yoon, *Appl. Phys. Lett*, 2011, 12, 3701-3703.
36. Y. C. Chen, X. Lou, P. Ingram, and E. Yoon, *Proceedings of MicroTAS*, Seattle, 2011,. 1409-1411.
37. Y.-C. Chen, Pa. Ingram, X. Lou, and E. Yoon, *Proceedings of MicroTAS*, Okinawa, 2012, 1241-1244.
38. M. A. Eddings and B. K. Gale, *J. Micromech. Microeng*. 2006, 16, 2396.
39. C. Lochovsky, S. Yasotharan and A. Günther, *Lab Chip*, 2012, 12, 595-601.
40. G. J. VanBerkel, F. Zhou, J. T. Aronson, *International journal of mass spectrometry and ion processes*, 1997, 162(1), 55-67.

Chapter 5

1. R. Peerani and Peter W. Zandstra, *J. Clin. Invest*, 2010, 120, 60–70.
2. D. Hanahan, R. A. Weinberg. *Cell*, 2011, 144, 646-74.
3. M. Cristofanilli, G. T. Budd, M. J. Ellis, A. Stopeck, J. Matera, M. C. Miller, J. M. Reuben, G. V. Doyle, W. J. Allard, L. W.M.M. Terstappen, and D. F. Hayes, *N Engl J Med*, 2004, 351, 781-91.
4. M. J. Bissell and W. C Hines, et al, *Nature Medicine*, 2011, 17, 320-329.
5. P. Mignatti, T. Morimoto, D.B. Rifkin, *Proc Natl Acad Sci U S A*, 1991, 15, 11007-11.
6. A.Y. Hsiao, Y. Torisawaa, Y. Tung, S. Sud, R. S. Taichman, K. J. Pienta, , S. Takayama, *Biomaterials*, 2009, 30, 3020-7.

7. M. Bauer, G. Su, D. J. Beebe, A. Friedl, *Integr Biol.*, 2010, 2, 371-8.
8. Y. Gao, D. Majumdar, B. Jovanovic, C. Shaifer, P. C. Lin. A. Zijlstra, D. J. Webb and D. Li, *Biomed Microdevices*, 13, 539-48, 2011.
9. D. Majumdar, Y. Gao, D. Li, and D. J. Webb, *J Neurosci Methods*, 196, 38-44, 2011.
10. M. Heneweer, M. Muusse, M. Dingemans, P. C. de Jong, M. van den Berg, J. T. Sanderson, *Toxicol Sci*., 2005, 83, 257-63.
11. J. Park, H. Koito, J. Li, A. Han, *Biomed Microdevices*, 2009, 11, 1145-53.
12. H. Ma, T. Liu, J. Qin, B. Lin, *Electrophoresis*, 2010, 31, 1599-605.
13. Elliot E. Hui, Proc. *Natl. Acad. Sci. U. S. A*, 2007, 104, 5722–5726.
14. I. K. Zervantonakis, S. K. Hughes-Alford, J. L. Charest, J. S. Condeelis, F. B. Gertler and R. D. Kamm, roc. *Natl. Acad. Sci. U. S. A*., 2012, 109, 13515–20.
15. E. Tumarkin, L. Tzadu, E. Csaszar, M. Seo, H. Zhang, A. Lee, R. Peerani, K. Purpura, P. W. Zandstra and E. Kumacheva, *Integr. Biol*, 2011, 3, 653-662.
16. S. Hong, Q. Pan and L. P. Lee, *Integr. Biol*., 2012, 4, 374–80.
17. J. Pan, A. L. Stephenson, E. Kazamia, W. T. S. Huck, J. S. Dennis, A. G. Smith and C. Abell, *Integr. Biol*., 2011, 3, 1043–1051.
18. T. P. Lagus and J. F. Edd, *RSC Adv*, 2013, 3, 20512.
19. A. Huebner, D. Bratton, G. Whyte, M. Yang, A. J. deMello, C. Abell and F. Hollfelder, *Lab Chip*, 2009, 9, 692–698.
20. S.M. Frisch, R.A. Screaton, *Curr Opin Cell Biol*, 2001 13, 555-562.
21. P. Ingram, Y. J. Kim, T. Bersano-Begey, X. Lou, A. Asakura, and E. Yoon, *Proceeding of MicroTAS*, 2010, 277-279.
22. Y.-C. Chen, X. Lou, P. Ingram, and E. Yoon, *Proceeding of MEMS*, 2012, 792-795.
23. W.-H. Tan and S. Takeuchi, *Proc Natl Acad Sci U S A*, 2007, 104(4), 1146–1151.
24. J. Chung, Y. J. Kim and E. Yoon, *Appl. Phys. Lett*, 2011, 12, 3701-3703.
25. Y.-C. Chen, P. Ingram, X. Lou, and E. Yoon, *Proceeding of MicroTAS*, 2012, 1241-1244.
26. S.-Y. The, R. Lin, L.H. Hung and A.P. Lee., *Lab Chip*, 2008, 8, 198–220.
27. W.-A. C. Bauer, M. Fischlechner, C. Abell and W. T. S. Huck, *Lab Chip*, 2010, 10, 1814–1819.
28. W.-H. Tan and S. Takeuchi, *Lab Chip*, 2006, 6, 757–763.
29. M.T. Guo, A. Rotem, J. A. Heyman, D. A Weitz, *Lab Chip*, 2012, 12, 2146–2155.
30. Z. Cao, B. VanDerElzen, K. J. Owen, J. Yan, G. He, R. L. Peterson, D. Grimard, and K. Najafi, *Proceeding of MEMS*, 2013, 361-364
31. M. Zhang, J. Wu, L. Wang, K. Xiao and W. Wen, *Lab Chip*, 2010, 10, 1199-1203
32. J M. Karlsson1, T. Haraldsson, C. F. Carlborg, J. Hansson, A. Russom and W. VanDerWijngaart, *J. Micromech. Microeng*. 2012, 22, 085009.
33. K. G. Neiva, K. A. Warner, M. S. Campos, Z. Zhang, J. Moren, T. E. Danciu and J. E. Nör, *BMC Cancer*, 2014, 14, 99.

Chapter 6

1. McClellan J, King MC. *Cell*, 2010. 141, 2, 210-217
2. Shackleton M, Quintana E, Fearon ER, Morrison SJ. *Cell*, 2009. 138(5), 822-829.
3. Bonnet D, Dick JE. *Nature Medicine*, 1997, 3, 730-737.
4. Mei Zhang M, Behbod F, Atkinson RL, Landis MD, Kittrell F, Edwards D, Medina D,

Tsimelzon A, Hilsenbeck S, Green JE, Michalowska AM, Rosen JM. *Cancer Res*, 2008. 68, 4674.

5. Maitland NJ, Collins AT. *JCO*, 2008. 26(17), 2862-2870.
6. Reya T, Morrison SJ, Clarke MF, Weissman IL. *Nature*, 2001, 414, 105-111.
7. Visvader JE. *i*, 2009, 23, 2563-2577.
8. Zhou J, Zhang Y. *Cell Cycle*, 2008, 7(10), 1360-1370.
9. Chen R, Nishimura MC, Bumbaca SM, Kharbanda S, Forrest WF, Kasman IM, Greve JM, Soriano RH, Gilmour LL, Rivers CS, Modrusan Z, Nacu S, Guerrero S, Edgar, Wallin JJ, Lamszus K, Westphal M, Heim S, James CD, VandenBerg SR, Costello JF, Moorefield S, Cowdrey CJ, Prados M, Phillips HS. *Cancer Cell,* 2010, 17(4), 362-375.
10. Croker AK, Goodale D, Chu J, Postenka C, Hedley BD, Hess DA, Allan AL. *J Cell Mol Med*, 2009, 13(8), 2236-2252.
11. Dexter DL, Leith JT. *JCO*, 1986, 4(2), 244-257.
12. Geisler JP, Rose SL, Geisler HE, Miller GA, Wiemann MC, 2002, 7, 25-28.
13. R. Peerani and Peter W. Zandstra, *J. Clin. Invest*, 2010, 120, 60–70.
14. Raghu Kalluri and Michael Zeisberg, *Nature Reviews Cancer*, 2006, 6, 392-401.
15. Dan Liu, and Peter J. Hornsby, *Cancer Res,* 2007, 67(7), 3117–26.
16. P. B. Gupta, C. L. Chaffer and R. A. Weinberg, *Nat. Med*., 2009, 15(9), 1010–1012.
17. M. Heneweer, M. Muusse, M. Dingemans, P. C. de Jong, M. van den Berg, J. T. Sanderson, *Toxicol Sci*., 2005, 83(2), 257-63.
18. A.Y. Hsiao, Y.S. Torisawa, Y.C. Tung, S. Sud, R.S. Taichman, K. J. Pienta, S. Takayama, *Biomaterials*, 2009, 30(16), 3020-7.
19. J. Park, H. Koito, J. Li, A. Han, *Biomed Microdevices*, 2009, 11(6), 1145-53.
20. M. Bauer, G. Su, D. J. Beebe, A. Friedl, *Integr Biol*., 2010, 2(7-8):371-8.
21. H. Ma, T. Liu, J. Qin, B. Lin, *Electrophoresis*, 2010, 31(10), 1599-605.
22. Y. Gao, D. Majumdar, B. Jovanovic, C. Shaifer, P. C. Lin, A. Zijlstra, D. J. Webb, D. Li, *Biomed Microdevices*, 2011, 13(3), 539-48.
23. D. Majumdar, Y. Gao, D. Li, D. J. Webb, J Neurosci Methods, 2011, 196(1), 38-44.
24. E. Tumarkin, L. Tzadu, and E. Kumacheva, *Integr. Biol*., 2011, 3, 653-662.
25. P. Ingram, Y. J. Kim, T. Bersano-Begey, X. Lou, A. Asakura, and E. Yoon, *Proceedings of MicroTAS*, Groningen, 2010, 277-279.
26. J. Frimat, M. Becker, Y. Chiang, and J. West, *Lab Chip*, 2011, 11, 231-237.
27. S. Hong, Q. Pan and L. P. Lee, *Integr. Biol*., 2012, 4, 374–80.
28. Y.-C. Chen, Y.-H. Cheng, H.S. Kim, P.N. Ingram, J.E. Nor and E. Yoon, *Lab Chip*, 2014, 14 (16), 2941 - 2947.
29. Yu-Chih Chen, Patrick Ingram and Euisik Yoon, *Analyst*, 2014, Advance Article, DOI: 10.1039/C4AN01282H
30. Gabriela Dontu, Wissam M. Abdallah, Jessica M. Foley, et al. *Genes Dev*., 2003, 17, 1253-1270.
31. Yi-Chung Tung, Amy Y. Hsiao, Steven G. Allen, Yu-suke Torisawa, Mitchell Ho and Shuichi Takayama, *Analyst*, 2011, 136, 473-478.
32. W.-H. Tan and S. Takeuchi, *Proc Natl Acad Sci U S A*, 2007, 104(4), 1146–1151.
33. Alison M Skelley, Oktay Kirak, Heikyung Suh, Rudolf Jaenisch and Joel Voldman., *Nature Methods*, 2009, 6, 147 – 152.
34. J. Chung, Y.-J. Kim and E. Yoon, *Appl. Phys. Lett*, 2011, 98(12), 3701.
35. Y.-C. Chen, P. Ingram, X. Lou, and E. Yoon, *Proceeding of MicroTAS*, 2012, 1241-

1244.

36. J. Visvader & G. Lindeman, *Nature Reviews Cancer*, 2008, 8, 755–768.

Chapter 7

1. Negrini S, Gorgoulis VG, Halazonetis TD, *Nat Rev Mol Cell Biol.*, 2010, 11(3):220-228.
2. Visvader JE, Lindeman GJ, *Nat Rev Cancer*, 2008, 8(10):755-768.
3. John A. Baron., *Nat Rev Cancer*, 2012, 12, 368-371.
4. Chung J, Kim Y.-J., and Yoon E, *Appl. Phys. Lett*, 2011, 98(12), 370.
5. Chao Ma, Rong Fan, Habib Ahmad, Qihui Shi, Begonya Comin-Anduix, Thinle Chodon, Richard C Koya, Chao-Chao Liu, Gabriel A Kwong, Caius G Radu1,, Antoni Ribas and James R Heath, *Nature Medicine,* 2011, 17, 6, 738-744.
6. Yvonne J. Yamanaka, Gregory L. Szeto, Todd M. Gierahn, Talitha L. Forcier, Kelly F. Benedict, Mavis S.N. Brefo, Douglas A. Lauffenburger, Darrell J. Irvine, and J. Christopher Love, *Anal. Chem.*, 2012, 84, 10531−10536.
7. Yao Lu, Jonathan J. Chen, Luye Mu, Qiong Xue, Yu Wu, Pei-Hsun Wu, Jie Li, Alexander O. Vortmeyer, Kathryn Miller-Jensen, Denis Wirtz, and Rong Fan, *Anal. Chem.*, 2013, 85, 2548−2556.
8. Reya T, Morrison SJ, Clarke MF, Weissman IL, *Nature*, 2001, 414, 105-111.
9. Shackleton M, Quintana E, Fearon ER, Morrison SJ, *Cell*, 2009,138(5), 822-829.
10. Canavan HE, Cheng X, Graham DJ et al., *J Biomed Mater Res A.,* 2005, 75(1):1-13.
11. Lili C. Kudo, Nancy Vi, Zhongcai Ma, Tony Fields, Nuraly K. Avliyakulov, Michael J. Haykinson, Anatol Bragin, Stanislav L. Karsten, *PlosOne*, 2012, 7, 7, e41564.
12. Orane Guillaume-Gentil, Tomaso Zambelli and Julia A. Vorholt, *Lab Chip*, 2014, 14, 402-414.
13. Kimio S, Kyoko K, Toshiyuki T, et al., *Proceedings of MicroTAS* 2013, 100-102.
14. Sada T, Fujigaya T, Niidome Y, Nakazawa K, Nakashima N, 2011, *ACS Nano.* 5(6):4414-21.
15. Baac H-W, Ok J-G, Maxwell A, Lee K-T, Chen Y-C et al., 2012, *Sci. Rep*. 2, 989.
16. Grudzien P., Lo S., Albain K.S., Robinson P., Rajan P., Strack P.R., Golde T.E., Miele L. and Foreman K.E., *Anticancer Research*, 2010, 30, 3853-3868.
17. Cao L., Zhou Y., Zhai B., Liao J., Xu W., Zhang R., Li J., Zhang Y., Chen L., Qian H., Wu M. and Yin Z., BMC *Gastroenterology*, 2011, 11,71.